RAPID MAGNETIC PRINTING OF 3D CELLULAR STRUCTURES USING MAGNETIC CELL BIOINKS

RAPID MAGNETIC PRINTING OF 3D CELLULAR STRUCTURES USING MAGNETIC CELL BIOINKS

By SARAH MISHRIKI, B.TECH.

A Thesis Submitted to the School of Graduate Studies in Partial Fulfillment of the Requirements for the Degree Doctor of Philosophy

McMaster University DOCTOR OF PHILOSOPHY (2021) Hamilton, Ontario (School of Biomedical Engineering)

TITLE: Rapid Magnetic Printing of 3D Cellular Structures Using Magnetic Cell Bioinks

AUTHOR: Sarah Mishriki, B. Tech (McMaster University) SUPERVISOR: Professor Ishwar K. Puri NUMBER OF PAGES: xxii, 200

Lay Abstract

The unmet medical need for accurate and personalized therapeutic treatment inspires the fabrication of miniaturized disease models. These models can be made outside of the body using human cells and used to represent physiological phenomenon to predict the clinical outcomes of disease. We describe a rapid method of fabricating such models using magnetic forces. By the addition of a magnetic salt, we can magnetize a liquid containing a suspension of human cells so that they are displaced towards areas where the magnetic field strength is low. The use of these magnetized cell suspensions can be used as biological inks for the rapid printing of three-dimensional cellular structures. The potential of this method to rapidly print living biological constructs emphasizes the realization of personalized medicine and a pathway towards an accelerated drug discovery process.

Abstract

In this thesis, a rapid magnetic printing technique has been developed for contactless, label-free, and scaffold-free printing of three dimensional (3D) cellular structures *in vitro*. The biological inks (bioinks) used to form these structures were composed of cells suspended in a liquid medium. Development of this technique was based on exploiting the inherent magnetic susceptibility of cells. Since cells and their liquid medium are diamagnetic (negative magnetic susceptibility), a paramagnetic salt hydrate, gadopentatic acid (Gd-DTPA), was added to the liquid medium to increase its magnetic susceptibility. When a magnetic field was applied, the host fluid containing the paramagnetic salt was towards regions of high magnetic field strength, displacing the cells towards regions towards regions of low magnetic field strength.

This rapid printing technique using magnetic cell bioinks was first described using whole blood to form various structures including spherical clusters (spheroids), strips, and three-pointed stars. This demonstration verified the printing technique as a safe and non-toxic method. Subsequent studies were performed using a frequently studied human breast cancer cell line, Michigan Cancer Foundation-7 (MCF-7), to develop a thorough protocol using mammalian cells. Here, the printing method was used to form 3D cellular structures on ultra-low attachment (ULA) and 2.5D cellular structures on tissue-culture-treated (TCT) surfaces. These geometries were produced within 6 hours with high reproducibility.

The use of a co-culture on TCT surfaces using MCF-7 and human umbilical vein endothelial cells (HUVECs) and on ULA surfaces using MD Anderson metastatic breast-

231 (MDA-MB-231) and embryonic mouse fibroblast (3T3) cells demonstrated the observance of unique cellular interactions and improved printing abilities (accelerated time and improved reproducibly) of the structures printed with magnetic inks, respectively.

The use of magnetic cell inks in research and clinical settings can accelerate the development of medical innovations such as drug discovery, personalized medicine, and treatment of disease.

Acknowledgements

"It takes a village to raise a child." The same can and should be said about completing a PhD. To my village: from the bottom of my heart, I thank you. This dissertation is the product of the many privileges I have been so fortunate to receive, and the accumulation of the efforts and sacrifices of my family, colleagues, friends, and mentors. I have been blessed beyond comprehension, and I am fully and eternally thankful to you.

My foremost thanks are to my supervisor, Professor Ishwar K. Puri. His guidance and genuine confidence in my abilities has been my source of academic growth. The opportunities to expand my skills and deepen my love for research is due to the collaborative and high-caliber educational environment that he has shaped in his Multiphysics Research Group and within McMaster Faculty of Engineering. There are no words to fully express my sincere thanks and appreciation for his guidance and constant support. My progress and the quality of my thesis would not have been the same without the continued advice and expertise of my supervisor and valued committee members, Professor Todd Hoare and Professor Ravi Selvaganapathy.

I have found great mentors and colleagues in MuRG. I have learned far beyond my expectations and gained new perspectives in research through collaborations with Dr. Fei Geng, Dr. Abdel Rahman Abdel Fattah, Dr. Rakesh P. Sahu, Dr. Srivatsa Aithal, Dr. Suvojit Ghosh, Dr. Ahmed Abdalla, Dr. Tamaghna Gupta, Dr. Rohit Gupta, Elvira Meleca, Tobias Kammann, and Carolina Chávez Madero. The achievements accomplished together were

not possible had they been attempted individually. I thank them for putting new meaning to the phrase, *"The whole is greater than the sum of its parts."* The moral support from my MuRG group members can not be underestimated or unacknowledged. It has been pure joy to be in the midst of such incredible company among Dr. Tahereh Majdi, Dr. Huifang Pang, Dr. Peiying Jennifer Tsai, Dr. Ri Chen, Dr. Sahar Asgari, Dr. Krishna Jangid, Dr. Mohamed Nawwar Arash Fattahi, and Aiswarya Susan Mathai.

Finally, I would like to thank my sweet and wonderful family. The number of selfless acts of kindness and support is infinite. There is not enough time (or space in this thesis) to describe each one of them, big or small. Everything from bringing snacks to my room when I have forgotten to eat to letting me put thousands of kilometers on their car for my daily commute from Scarborough to McMaster, my parents and brother have unofficially but whole-heartedly made the same commitment to completing this dissertation as I since January 2016. I truly could not have done it without them. To my extended family, future family, friends who became family, your prayers were never ceasing and constantly at work. I have truly been so lucky and fortunate to be on the receiving end of such support. Thank you, thank you, thank you.

Table of Contents

List of all Figures and Tables

Table of Figures

List of Tables

List of all Abbreviations and Symbols

List of Abbreviations

$2^{(-\Delta\Delta CT)}$	Delta-delta cycle threshold
2D	Two-dimensional
2.5D	Two-and-a-half-dimensional
3D	Three-dimensional
ANOVA	Analysis of variance
ATCC	American type culture collection
ATP	Adenosine triphosphate
bFGF	Basic fibroblast growth factor
bioMEMS	Biological micro-electro-mechanical systems
BSA	Bovine serum albumin
CA	Contrast agent
CAGR	Compounded annual growth rate
CAF	Cancer-associated fibroblast
cDNA	Complementary deoxyribonucleic acid
CTC	Circulating tumor cell
CYP450	Cytochrome P450
DAPI	4′,6-diamidino-2-phenylindole
DMEM	Dulbecco's modified eagle medium
DMSO	Dimethyl sulfoxide
ECM	Extracellular matrix
EDTA	Ethylenediaminetetraacetic acid
EGF	Epidermal growth factor
EGFP	Enhanced green fluorescent protein
ELISA	Enzyme-linked immunosorbent assay
EMT	Epithelial-mesenchymal transition

ER	Estrogen receptor
FBS	Fetal bovine serum
FeHA	Fe-doped hydroxyapatite
FEMM	Finite Element Magnetic Method
FITC	Fluorescein isothiocyanate
GAPDH	Glyceraldehyde 3-phosphate dehydrogenase (gene)
Gd-BT-DO3A	Gadobutrol (Gadavist)
Gd-DTPA	Gadopentatic acid, diethylenetriaminepentaacetic acid gadolinium (III) dihydrogen salt hydrate
gelMa	Gelatin methacrylate
GFP	Green fluorescent protein
GFP+	Green fluorescent protein-transfected
HEPES	4-(2-hydroxyethyl)-1-piperazineethanesulfonic acid
HER2	Human epidermal growth factor 2
HGMF	High-gradient magnetic field
HIF1α	*Hypoxia-inducible factor-1-alpha* (gene)
ICP-MS	Inductively coupled plasma mass spectrometry
IMS	Immunomagnetic separation
IQR	Interquartile range
μ-TAS	Micro-total analysis systems
MeHA	Methacrylated hyaluronic acid
MEMS	Micro-electro-mechanical systems
MFH	Magnetic fluid hyperthermia
MNP	Magnetic nanoparticle
MRI	Magnetic resonance imaging
MTT	3-(4,5-dimethylthiazol-2-yl)-2,5-diphenyltetrazolium bromide
N-S-N-S	North-South-North-South
N52	NdFeB 52

NK	Natural killer
NSF	Nephrogenic systemic fibrosis
PBS	Phosphate buffered saline
PCL	Poly(ε-caprolactone)
PCR	Polymerase chain reaction
PDMS	Polydimethylsiloxane
PDT	Photodynamic therapy
PEG	Polyethylene glycol
PEGDA	Polyethylene glycol dimethacrylate
PLGA	Poly(d, L-lactide-co-glycolide)
PS	Polystyrene
Q1	First quartile, 25^{th} percentile
Q3	Third quartile, 75^{th} percentile
qPCR	Quantitative polymerase chain reaction
rBM	Recombinant basement membrane
RLU	Relative luminescence unit
RFP	Red fluorescent protein
RPF+	Red fluorescent protein-transfected
RNA	Ribonucleic acid
RPMI	Rosewell Park Memorial Institute
Rs	Separation resolution
RT-qPCR	Quantitative reverse-transcription polymerase chain reaction
SARS-CoV-2	Severe acute respiratory syndrome coronavirus 2
SD	Standard deviation
SEM	Standard error of the mean
SEM-EDS	Scanning electron microscopy energy-dispersive X-ray spectroscopy
SPION	Super paramagnetic iron oxide nanoparticle

SQUID	Superconducting quantum interference device
SR-STXM	Synchrotron radiation scanning transmission X-ray microscopy
TCT	Tissue culture-treated
TME	Tumor microenvironment
ULA	Ultra-low attachment
USD	United States (American) dollar
UV	Ultraviolent
VEGF	*Vascular endothelial growth factor* (gene)

List of Cells and Cell Lines

293T	Human embryonic kidney, expressing SV40 large T antigen
3T3	Mouse embryonic fibroblast
3T3-L1	Mouse preadipocyte
7F2	Mouse adipogenic-differentiated osteoblasts
ASMC	Aortic smooth muscle cells
AVCC	Aortic valve co-culture
BALB/3T3	Mouse embryonic fibroblast
bND.3	Endothelial cells
C. reinhardtii	*Chlamydomonas reinhardtii*
CAF	Cancer-associated fibroblast
D1 ORL UVA	Mouse bone marrow stem cell
E. coli	*Escherischia coli*
ECV304	Human urinary bladder carcinoma
hbSMC	Human bladder smooth muscle cells
HEK293	Human embryonic kidney, also referred to as HEK
HFP	Human foreskin fibroblast
hiPSC-CM	Human induced pluripotent stem-cell-derived cardiomyocytes

HLF-1	Human lung fibroblast
Hs578bst	Human breast fibroblast
Hs578t	Triple-negative human breast carcinoma
HUVEC	Human umbilical vein endothelial cells
LN-229	Normal astrocyte
MCF-7	Michigan Cancer Foundation-7
MCF-10A/myr-Akt1	Human breast tumor model of MCF-10A
MCTS	Multicellular tumor spheroid
MDA-MB-231	MD Anderson metastatic breast-231
MSC	Mesenchymal stem cell
NHDF	Normal human dermal fibroblasts
NIH/3T3	Mouse Swiss NIH embryonic fibroblasts
PC-3	Human prostate cancer epithelial
RBC	Red blood cell
S. aureus	*Staphylococcus aureus*
S. cerevisiae	*Saccharomyces cerevisiae*
S. epidermidis	*Staphylococcus epidermidis*
SMC	Smooth muscle cells
SUM159	Human breast cancer
T98G	Human glioblastoma
TC	Tumor cell
U251/U251-MG	Human glioblastoma
U937	Human histolytic lymphoma monocytes
VIC	Valvular interstitial cells
VEC	Valvular endothelial cells
WAT	White adipose tissue
WBC	White blood cell

List of Symbols

a	Radius of a particle (m)
$\mathbf{B}$	Magnetic flux density (T)
$\mathbf{B}_{low}$	Region of low magnetic field strength (T)
C_T	Cycle threshold (dimensionless)
$d\mathbf{s}$	Differential area in the control surface ($\Delta\mathbf{s}$)
$d\vartheta$	Differential fluid element ($\Delta\vartheta$)
$\Delta\chi$	Magnetic susceptibility difference between an entity and the fluid medium that contains it (dimensionless), $\Delta\chi = \chi_p - \chi_m$
$\mathbf{F}$	Total magnetic body force acting on a fine-sized magnetizable body (N)
$\mathbf{F}_b$	Buoyancy force (N)
$\mathbf{f}_c$	Magnetic body force on a cell (N)
$\mathbf{F}_d$	Drag force on a spherical cell according to Stokes flow (N)
$\mathbf{F}_m$	Magnetic force (N)
$\mathbf{F}_{mag}$	Magnetic force on a cell (N)
g	Gravity (m/s^2, N/kg)
$\mathbf{H}$	Magnetic field strength (A/m)
$\mathbf{M}$	Magnetization (A/m)
μ_0	Magnetic permeability of a vacuum (constant, $4\pi\times10^{-7}$ N/A^2)
N	Demagnetization factor (dimensionless)
η	Medium viscosity (Pa s)
R	Radius (m)
$\mathbf{U}$	Velocity (m/s)
V_c	Cell volume (m^3)
χ_c	Magnetic susceptibility of a cell (dimensionless)
χ_{eff}	Effective magnetic susceptibility of a material (dimensionless)
χ_i	Intrinsic magnetic susceptibility of a material (dimensionless)

χ_m	Magnetic susceptibility of a fluid medium (dimensionless)
χ_p	Magnetic susceptibility of a particle (dimensionless)

Declaration of Academic Achievements

This dissertation was used to fulfill the requirements of Ph.D. degree. All the research projects were conducted from January 2016 to May 2021. During the period of thesis study, a thorough protocol describing rapid magnetic printing of 3D cellular structures was developed. This technique was initially demonstrated using whole blood, and later with various mammalian cell lines including Michigan Cancer Foundation-7, MD Anderson metastatic breast-231, and NIH/3T3. The major contribution of this thesis work was from myself.

This thesis has resulted in eight peer-reviewed journal articles, one manuscript to be submitted but not yet published (first author), and one US patent. Of the eight published articles, I am the first author on two of these papers and an equal contribution co-author of four. Co-author names were listed in alphabetical order for equal contribution manuscripts. The prepared and accomplished works are listed below:

1. **Sarah Mishriki**, Tamaghna Gupta, Rakesh P. Sahu, and Ishwar K. Puri. "3D cell printing and manipulation with magnetic bioinks." *To be submitted to **MDPI Biomolecules**.*
2. Srivatsa Aithal, **Sarah Mishriki**, Rohit Gupta, Rakesh P. Sahu, George Botos, Shazia Tanver, Russel W. Hanson, and Ishwar K. Puri. "SARS-CoV-2 detection with aptamer-functionalized gold nanoparticles." *Published on September 1, 2021 in **Talanta**.*

3. **Sarah Mishriki**, Srivatsa Aithal, Tamaghna Gupta, Rakesh P. Sahu, Fei Geng, and Ishwar K. Puri, "Fibroblasts accelerate formation and improve reproducibility of 3D cellular structures printed with magnetic assistance." *Published on July 23, 2020 in **AAAS Research**.*
4. Tamaghna Gupta, Srivatsa Aithal, **Sarah Mishriki**, Rakesh P. Sahu, Fei Geng, and Ishwar K. Puri, "Label-free magnetic-field-assisted assembly of layer-on-layer cellular structures." *Published on May 22, 2020 in **ACS Biomaterials Science and Engineering**.*
5. Abdel Rahman Abdel Fattah, Rakesh P. Sahu, Fei Geng, **Sarah Mishriki**, Elvira Meleca, Ishwar K Puri, Suvojit Ghosh "3d label-free contactless formation of cellular structures and co-cultures through diamagnetophoresis." *Published on May 2, 2019 in the **US Patent office**, application number 16178172.*
6. **Sarah Mishriki**, Abdel Rahman Abdel Fattah, Tobias Kammann, Rakesh P. Sahu, Fei Geng, and Ishwar K. Puri. "Rapid magnetic 3D printing of cellular structures with MCF-7 cell inks." *Published on February 4, 2019 in **AAAS Research**.*
7. Abdel Rahman Abdel Fattah, **Sarah Mishriki*****, Tobias Kammann, Rakesh P. Sahu, Fei Geng, and Ishwar K. Puri. "Gadopentatic acid affects in vitro proliferation and doxorubicin response in human breast adenocarcinoma cells." *Published on August 1, 2018 in **Springer Netherlands BioMetals**.*
8. Abdel Rahman Abdel Fattah, **Sarah Mishriki***, Tobias Kammann, Rakesh P. Sahu, Fei Geng, and Ishwar K. Puri. "3D cellular structures and co-cultures formed

through the contactless magnetic manipulation of cells on adherent surfaces." *Published on February 1, 2018 in* ***RSC Biomaterials Science****.*

9. Abdel Rahman Abdel Fattah, Ahmed M. Abdallah, **Sarah Mishriki*****, Elvira Meleca, Fei Geng, Suvojit Ghosh, and Ishwar K. Puri. "Magnetic printing of a biosensor: inexpensive rapid sensing to detect picomolar amounts of antigen with antibody-functionalized carbon nanotubes." *Published on March 17, 2017 in* ***ACS Applied Materials and Interfaces****.*
10. Abdel Rahman Abdel Fattah, Elvira Meleca, **Sarah Mishriki*****, Alina Lelic, Fei Geng, Rakesh P. Sahu, Suvojit Ghosh, and Ishwar K. Puri. "In situ 3D label-free contactless bioprinting of cells through diamagntophoresis." *Published on November 8, 2016 in* ***ACS Biomaterials Science and Engineering****.*

****Co-first authorship contribution.*

1 Introduction

The unmet medical need for tissues and organs inspires novel fabrication techniques to produce *in vitro* models for drug development, personalized medicine, and functional transplantable organs. In this investigation, a detailed protocol for rapid magnetic cell printing of 3D cellular structures was established. The process of establishing such protocol was performed using various cell lines to emphasize different printing capabilities. For all investigations, a paramagnetic MRI contrast agent (gadopentatic acid, Gd-DTPA) was used. Since most cells are diamagnetic, the addition of Gd-DTPA exploited the inherent magnetic susceptibility of the cells. This magnetic susceptibility difference then allowed the cells to be manipulated within the host fluid according to the arrangement of an external magnetic field.

A review of magnetic printing techniques and applications is provided in **Chapter 2**. Here, a *magnetic bioink* is defined as a solution containing both magnetic materials (such as nanoparticles or salts) and a biological entity (cells, proteins, biological system). Therefore, this definition includes *positive magnetophoresis*, where the intentional printing of an entity is dependent on a positive magnetic susceptibility in applications including cell printing using magnetic labels, IMS, MDT, and MFH; and *negative magnetophoresis*, where the intentional printing of an entity is dependent on displacement due to a negative magnetic susceptibility in applications including cell printing, cell isolation, and levitation of hydrogels. This review serves as a background to the field of magnetic printing, with emphasis on magnetic cell printing. The remaining chapters are based on experimental results of magnetic cell printing through negative magnetophoresis. In each, the printing

method is described, with emphasis on which objective the use of magnetic printing is intended to overcome.

Initial observations were described in a proof-of-concept demonstration using whole blood in a suspension of 200 mM Gd-DTPA in PBS (**Chapter 3**). Three geometries were explored and verified using different magnet arrangements, sizes and vessels. Two rod magnets (magnetized through thickness) were arranged parallel to one another, on either side of a cylindrical vial. This resulted in the formation of a line geometry. Second, three rod magnets (magnetized through length) were surrounding a cylindrical vial 120º apart, resulting in the formation of a three-pointed star geometry. Lastly, cube magnets were arranged in alternating North-South-North-South orientation. A rectangular vial was placed on top of the array, and spherical clusters were formed at each intersection of a magnet quartet. This spherical cluster formation was used for further investigations using mammalian cells.

Tumor cells are often studied to explore response to drugs and environmental stimulants to predict clinical outcome. However, their attachment to a non-biological, 2D substrate influence their ability to recapitulate physiological phenomenon, such as the production of ECM, cell-cell interaction, proteomic and genomic expressions, metabolic activity, and response to a drug. The formation of miniaturized 3D structures is able to overcome such challenges, bridging the gap between traditional cellular study platforms and animal models.

The formation of monotypic 3D and 2.5D spherical cell clusters (referred to as *spheroids*) is described in **Chapter 4**. Here, a magnet quartet was aligned with 384-well

ultra-low attachment (ULA) and 96-well tissue culture-treated (TCT) multi-well plates to form 3D and 2.5D cellular structures, respectively. Various parameters were explored to determine the optimal conditions for cellular printing using MCF-7 cells, a human metastatic breast cancer cell line. The parameters studied include: the effect of Gd-DTPA on: cell proliferation, cell morphology, and on the ability to concentrate cells, the effect of incubation time to form a robust structure, growth and reproducibility (measured by projected area and circularity), and gene expressions of *VEGF* and *HIF1α*. It was determined that 25 mM Gd-DTPA was sufficient for magnetic printing of 5000 cells to form a circular cluster in an ULA surface, and 3000 cells in a TCT surface within 6 hours. In comparison to non-magnetic printing i.e. spheroids formed on flat and round ULA surfaces, magnetic printing was shown to be highly reproducible.

The method of forming 3D spherical structures in on ULA surfaces was expanded to form spherical co-culture assemblies on an ULA surface, as described in **Chapter 5**. Here, the main objective was to accelerate the formation and improve the reproducibility of 3D cellular structures composed of a human metastatic breast cancer cell line, MDA-MB-231, and fibroblasts (embryonic mouse fibroblasts, NIH/3T3). The high clinical significance of MDA-MB-231 has been underrepresented *in vitro*, due to difficulties in forming 3D cellular structures. The fibroblasts, through their active role in producing and reforming ECM, were hypothesized to behave as a 'glue' to hold an MDA-MB-231-containing 3D cellular structure together. Magnetic printing was shown to improve both time and reproducibility (measured by projected area and circularities) of monotypic MDA-MB-231 cellular structures in comparison to formation through gravitational settling alone,

which was demonstrate through the use of a round-bottom ULA surface. For the first time without additional reagents, the formation of MDA-MB-231 3D cell cluster was observed within 24 hours is magnetic printing, whereas formation via gravitational settling alone required 48 hours. The introduction of fibroblasts further improved the time of formation and reproducibility of the 3D cellular structures. However, projected circularity and area measurements during two weeks revealed that even short exposure times to Gd-DTPA had negative impacts on the growth of monotypic and co-culture clusters.

In a separate study, the formation of 2.5D co-culture assemblies on a TCT surface was investigated, as described in **Chapter 6**. Here, the TCT surface promoted the attachment of HUVECs to form a 2D cell layer. Following their attachment, a 3D circular structure composed of MCF-7 cells was magnetically patterned using the same magnet quartet as previously described. The resulting heterogeneous cell landscape was an expanding monolayer originating from the cells on the periphery of the 3D cellular structure. The interaction of the two cell lines revealed unique morphologies not observed in typical cell study platforms.

Concluding remarks and future directions are provided in **Chapter 7**.

2 3D Cell Printing and Manipulation with Magnetic Bioinks

This chapter is reproduced from *3D cell printing and manipulation with magnetic bioinks*, submitted for publication in *MDPI Biomolecules, **Sarah Mishriki**, Tamaghna Gupta, Rakesh P. Sahu and Ishwar K. Puri.* The author of this thesis is the first author and the main contributor of this publication.

2.1 Abstract

Three-dimensional (3D) printing is typically performed by adding materials in the form of quasi-two-dimensional layers to fabricate 3D structures. When magnetic inks are used for this purpose, their components are printed and organized by applying an external magnetic field. The magnetic field induces magnetophoresis, allowing manipulation of the printed material by action-from-a-distance that produces a 3D construct. This review describes how magnetic bioinks composed of magnetic salts or particles and biological molecules, such as cells and proteins, are used for 3D printing. Emphasis is placed on the emerging use of magnetic bioinks to print living 3D biological materials and cellular structures. Other applications, including cell separation, biosensing, magnetic fluid hyperthermia, and magnetic drug targeting, are also discussed. Magnetic bioinks offer solutions for diagnosis, *in vitro* research, and treatment of disease.

2.2 Introduction

Human diseases are often first studied in a population of mammalian cells attached to an artificial two-dimensional (2D) substrate, but an *in vitro* environment can lead to inaccurate conclusions. After 2D cell culture investigations, animal studies are used to evaluate

therapeutic candidates in living systems, *in vivo*.[1] 2D cell models are often not appropriate indicators of preclinical success due to the presence of different cell receptors[2] and non-human pathophysiology.[3] Hence, approximately only 5-8% of therapeutic candidates studied in animal models translate into clinical human trials.[3-5] Ethical concerns, standardization issues, and high cost also limit the use of animal models. While mathematical models can predict clinical outcomes of tumorigenesis[6] and chemotherapeutic drug efficacy,[7] they do not consider the dynamics of a biological system with feedback.

Due to shortcomings associated with 2D cell models, animal studies, and analytical solutions, 3D cell models can offer more accurate recapitulation of physiological phenomena. 3D cultures demonstrate superior *in vivo* phenomena, such as gene expression,[8] drug potency,[1] cell morphology,[9-10] formation of organized extracellular matrix (ECM),[10] and regions of proliferative, senescent, and necrotic cell layers.[11] These cultures better reproduce the mechanical properties mediated by neighboring cells and the ECM.[9] Since the goal of 3D cell modeling is to more faithfully represent native tissue environments *in vitro*, it follows that the development of 3D cellular structures will eventually replace 2D cell models to refine and reduce the number of animal studies for high-throughput screening.[12] Other applications of 3D cellular structures include drug discovery and screening;[4, 10, 13-14] disease modeling with organoids,[15-17] organ-on-chip[18-19] and tumor-on-chip[20-21] devices; tumor modeling;[22] and cell-containing transplantable tissues.[23-26]

Biological materials, molecules, and cells can be incorporated into printable inks for three-dimensional (3D) printing, e.g., for tissue engineering and regenerative medicine applications.[27-28] Autologous constructs have been formed for patients in end-stage diseases, such as biologically active bladder surrogates,[29] and engineered airways for adult[30] and pediatric[31] candidates using human adult donor trachea and patient-derived mesenchymal stem cells (MSCs). The static definition of 3D printing can be broadened to include emerging printing techniques that also exhibit dynamic, time-dependent changes in the biological constructs. When a stimulus-responsive material is used,[32-33] the construct can be controlled over time.[27]

Various printing methods have been employed to manipulate cells and biological materials in a 3D space, including acoustophoresis;[34-35] temperature;[36-37] light;[38] biochemical gradients;[39] and electric stimuli,[40] where magnetophoresis is a recent addition.[41-48] Using action-from-a-distance with a magnetic field, high-resolution patterns are printed with magnetic inks, often without introducing scaffolds or solid structures. This is of particular importance for biomedical applications, where biological materials require an environment that adapts to their dynamic interactions and native microenvironments during 3D self-assembly,[49] while also maintaining viability and functionality.

In general, an ink is a solution that contains a dispersed entity within a host fluid. The host fluid and dispersed entity differ in a particular aspect, allowing the entity to be displaced within its liquid counterpart. A bioink is a dispersion containing biological entities, such as cells, proteins, or biologically derived materials that are to be printed in a liquid counterpart that is both biocompatible and has a property distinct from the dispersed

biological entity. Thus, magnetic bioinks are suspensions containing magnetic materials that control the placement of biological entities under the influence of an applied magnetic field. This definition is consistent with traditional concepts of 3D printing since the intentional positioning of suspended entities is shared.

A summary of the broad applications and considerations of magnetic bioinks is provided in **Figure 2.1** and **Table 2.1**. Simply put, magnetic manipulation and magnetic printing require a magnetic field and entities that will respond to it. These fields do not require complex instrumentation and can be generated with common rare-earth magnets.[50] Thus, magnetic manipulation is easily integrated with existing systems for contactless control of target specimens.[46]

This review focuses on the recent advances in magnetic bioinks composed of magnetic salts, magnetic nanoparticles (MNPs), and cells for applications in cell manipulation and 3D cell printing. The ability to form 3D cellular constructs with physiological relevance is based on the rich science of recent innovations in manipulation techniques using magnetic materials. Special attention is placed on the emerging use of magnetic bioinks to print 3D cellular structures and tissues that offer solutions for diagnosis, *in vitro* research, and disease treatment.

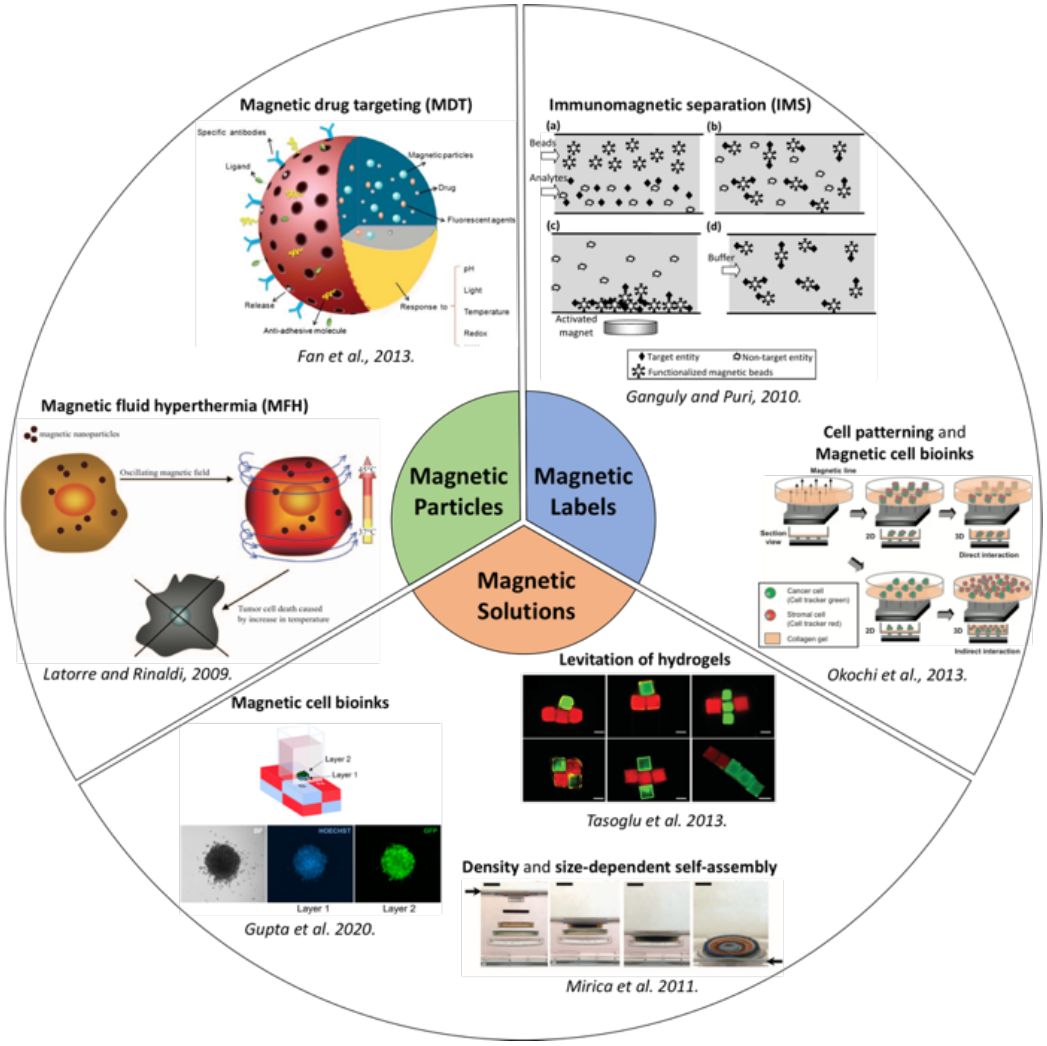

Figure 2.1: Applications of magnetic bioinks. Magnetic bioinks are categorized under magnetic particles, magnetic labels, or magnetic solutions. Magnetic particles are used *in vivo* for therapeutic applications, such as magnetic fluid hyperthermia (MFH; reprinted from Ref. 51) and magnetic drug targeting (MDT; reprinted from Ref. 52). Magnetic labels are used for specific or non-specific labeling of molecules or cells such as in immunomagnetic separation (IMS; reprinted from Ref. 53) or cell patterning and magnetic cell bioinks (reprinted from Ref. 54), to render them

magnetic for *in vitro* applications. Magnetic solutions are utilized for label-free *in vitro* applications of diamagnetic materials such as 3D printing using magnetic cell bioinks (reprinted from Ref. 55), levitation of hydrogels for living material fabrication (reprinted from Ref. 56), and density and size-dependent self-assembly (reprinted from Ref. 57). Each satisfies the definition of a magnetic bioink by incorporating magnetic materials and a biological entity.

Table 2.1. Advantages and disadvantages of 3D printing using magnetic bioinks.

Methods	**Advantages**	**Disadvantages**
Label-based cell printing using MNPs	Surface-modified and smaller MNPs have little effect on cell proliferation[58, 59] High-throughput production of 3D cellular structures[60] The scale of constructs is in the mm range[61] Rapid formation[58, 60] Readily compatible with microfluidic devices[50]	Retention of MNPs within cell constructs after release from membrane[58] Nanoparticles discolor the medium, which interferes with colorimetric assays[58]
Label-free printing of cells using paramagnetic salt	Control over the geometry of the printed 3D cell structure[62] Rapid formation of cellular structures[55, 63, 64] High-throughput production[55, 63, 64] Readily compatible with microfluidic devices[50] Able to form unique cell landscapes e.g. 2.5D morphologies[64, 65] 3D geometries constructed in the mm range[66]	Toxicity associated with paramagnetic salt[63, 64, 71] Osmotic pressure imbalance[43]

	Exploitation of density differences for heterogeneous mixture of cells[67-70]	
Label-free printing of particles and objects	Exploitation of density differences for heterogeneous mixture of particles[49, 72] Particles can be levitated in axial and circular regions when using ring magnets[49] Can be combined with other action-from-a-distance methods, e.g. acoustophoresis[2]	Biological materials are typically diamagnetic, which require very strong magnetic fields, creating significant safety issues if ferromagnetic materials are nearby[73]
Label-based cell or particle separation	Continuous separation[74] Ability to process large volume ratios[66, 74] Ability to recirculate sorted cell fractions[74] More stable than fluorescent labels[50] Do not require light excitation[50]	Lengthy incubation[75] Removal of magnetic agents from target molecules for downstream applications[75] Exact control is required over the forces involved in the separation of labeled and unlabeled cells[74]
Label-free particle manipulation using a microfluidic device	Continuous separation[75] High throughput separation[50] High sensitivity[50]	Small sample volumes[76]
Magnetic fluid hyperthermia using MNPs	Less invasive than traditional therapies[77] Can be used to enhance chemotherapy and radiation therapy[51, 78]	Potential damage to healthy tissue by over-heating[79] Slow adoption into clinical settings[51]
Biosensing	Small sample volumes[80, 81] Simple design[80, 81] High sensitivity[80] and selectivity[81] Low energy requirement[80]	Requires the determination of specific biological targets[82] Low detection thresholds[80, 81, 83]

	Simple design[80] Rapid detection[80]	

2.3 Magnetophoresis fundamentals

Magnetic fields arise due to the motion of electric charges in the form of free and bound currents. The magnetic field within a magnetizable material,

$$\mathbf{B} = \mu_0 (\mathbf{M} + \mathbf{H}), \quad (2.1)$$

where $\mu_0 = (4\pi \times 10^{-7}\ \mathrm{N/A^2})$ denotes the permeability of vacuum. A free current, i.e., a flow of free charges through a conductor, produces **H**. The magnetization **M**, a material property, is produced by the collection of bound circulating currents generated by the orbital motion of electrons and electron spin[84]. The bound current loops behave as magnetic dipoles and, in most materials, their orientation is random in the absence of an external magnetic field. When a magnetic field is imposed, the materials can acquire a net magnetization parallel (paramagnets) or opposite (diamagnets) to the imposed field. In weak magnetic fields ($\mathbf{B} \leq$ 6 mT), the magnetization of most materials is proportional to the imposed **H,**[85] i.e.,

$$\mathbf{M} = \chi_i \mathbf{H}, \quad (2.2)$$

Where χ_i denotes the intrinsic magnetic susceptibility, a dimensionless quantity that is positive for paramagnetic and negative for diamagnetic materials. Materials are characterized by their response to a magnetic field as *diamagnetic*, *paramagnetic*, or *ferromagnetic*, as shown in **Figure 2.2**.

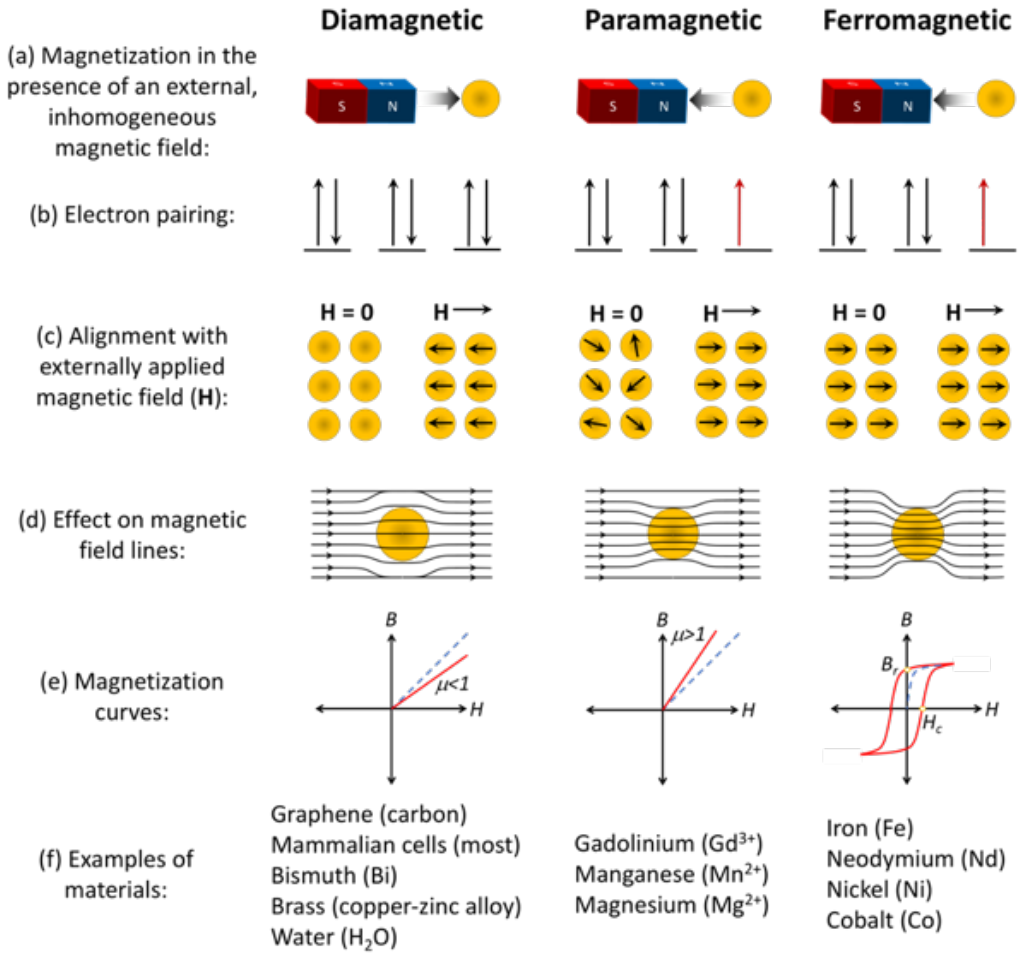

Figure 2.2: Characterization of diamagnetic, paramagnetic, and ferromagnetic materials. (**a**) Magnetization in the presence of an external, inhomogeneous magnetic field; (**b**) electron pairing; (**c**) alignment with an externally applied magnetic field; (**d**) magnetic field lines; and (**e**) magnetization curves. (**f**) Examples of materials in each category.

Diamagnetic materials are weakly repelled by a magnetic field and have a negative magnetic susceptibility, χ (~ 10^{-6}-10^{-3}). [86] They do not contain any unpaired electrons and have a net magnetic moment equal to zero in the absence of an external field **H**. In the

presence of an external magnetic field, their magnetization is in the direction opposite to that of **H**, thus repelling the magnetic lines of force.[87] An example of a diamagnetic material is graphene,[88, 89] which is a lattice structure produced by sp^2-hybridized carbon atoms. In a perfectly crystalline structure, this bonding pattern has electrons completing the s and 2p orbitals with no unpaired electrons. Other diamagnetic materials include bismuth,[86] brass,[86] and most mammalian cells.[90-92]

Paramagnetic materials are weakly attracted towards a magnetic field and have a small positive magnetic susceptibility ($\chi \sim 10^{-6}$-10^{-1}).[86] They contain at least one unpaired electron at the atomic level and have randomly aligned magnetic moments in the absence of a magnetic field. In the presence of a magnetic field, their magnetic moments align in the direction of **H** and are weakly attracted along the magnetic lines of force.[87] Like diamagnetic materials, their magnetic behavior is also diminished in the absence of a magnetic field. Examples include transition metal complexes such as chelates of gadolinium ions (Gd^{3+}), manganese (Mn^{3+}), and magnesium (Mg^{2+}) that are used to magnetize biological inks for label-free manipulation.

Ferromagnetic materials retain their magnetic field even after the external magnetic field has been removed. Only three elements – iron (Fe), nickel (Ni), and cobalt (Co) - have been found to be ferromagnetic at room temperature. Like paramagnetic materials, ferromagnetic materials have unpaired electrons and attract magnetic field lines. In the absence of a magnetic field, their magnetic moments are aligned and lie parallel to one another, which enhances their magnetization and attracts the material strongly along the magnetic lines of force. When an external magnetic field is applied, the magnetic moments

align with the direction of **H**. [86] These materials and their alloys are often used as permanent magnets, e.g., neodymium (Nd),[55, 62-65, 80, 81] Ni,[93] and Co.[94] When the size of the ferromagnetic materials is in the range of nanometers (nm), the magnetization of the magnetic domain of each particle flips randomly resulting in a zero-residual magnetization. However, in the presence of an external magnetic field the magnetic domains align with the direction of the applied field. This state of ferromagnetic materials is called superparamagnetism.[53, 95]

When a magnetizable material is exposed to a non-uniform magnetic field, it experiences a magnetic body force, also known as Kelvin body force, resulting from the interaction between the imposed **H** and induced **M**. The total magnetic body force acting on a finite-sized magnetizable body,[96]

$$\mathbf{F} = \iiint [\mu_0 (\mathbf{M}\cdot\nabla)\,\mathbf{H} + \nabla (\tfrac{1}{2}\,\mu_0\,\mathbf{M}\cdot\mathbf{M})]\,d\vartheta \qquad (2.3)$$

where $d\vartheta$ is the differential volume element. Using the corollary of the Gauss divergence theorem, $\iiint \nabla (\tfrac{1}{2}\,\mu_0\,\mathbf{M}\cdot\mathbf{M})]\,d\vartheta = \tfrac{1}{2}\mu_0 \oiint \mathbf{M}\cdot\mathbf{M}\,d\mathbf{s}$ differential area vector on the control surface. For a magnetizable body surrounded by a nonmagnetic medium, the control surface that completely encloses the magnetizable body lies in a region outside the body where $\mathbf{M} = 0$. Thus, the term $\tfrac{1}{2}\mu_0 \oiint \mathbf{M}\cdot\mathbf{M}\,d\mathbf{s}$ vanishes and Equation 2.3 reduces to:

$$\mathbf{F} = \mu_0 \iiint (\mathbf{M}\cdot\nabla)\,\mathbf{H}d\vartheta \qquad (2.4)$$

Physically, this force expression implies that the magnetizable body is attracted towards regions of higher **H**. Substituting Equation 2.2 in Equation 2.4, the magnetic force on an isolated spherical magnetic particle of radius *a* is obtained as:

$$\mathbf{F} = \mu_0 \left(^4/_3\ \pi a^3\right) \chi_{\text{eff}} (\mathbf{H}_0 \cdot \nabla)\mathbf{H}_0. \tag{2.5}$$

Here, χ_{eff} is the effective magnetic susceptibility of the particle, which is related to the intrinsic susceptibility χ_i by[96]

$$\chi_{\text{eff}} = \chi_i / 1 + N\chi_i \tag{2.6}$$

where N is the demagnetization factor. For a sphere, $N = {}^1/_3$. The effective magnetic susceptibility χ_{eff} considers the demagnetization effect when the induced particle dipole moment distorts the imposed field. The field $\mathbf{H}_0$ is located at the particle center. It is assumed that the particle is small enough so that the magnetic field and its gradient do not vary significantly within the particle volume.

Equation 2.5, which neglects the magnetic susceptibility of the surrounding medium, evaluates the Kelvin body force acting on ferromagnetic or superparamagnetic particles suspended in a nonmagnetic fluid. When the surrounding medium's magnetic susceptibility is at least four orders of magnitude smaller than the magnetic particles, it is neglected.[85] For cases where the susceptibility of the medium and the suspended particles are comparable (e.g., for diamagnetic particles suspended in a paramagnetic medium), Equation 2.5 assumes the form,

$$\mathbf{F} = \mu_0 \left(^4/_3\ \pi a^3\right) \Delta\chi\, (\mathbf{H}_0 \cdot \nabla)\mathbf{H}_0 \tag{2.7}$$

where $\Delta\chi = \chi_p - \chi_m$ denotes the difference between the magnetic susceptibilities of the particle (χ_p) and the surrounding medium (χ_m). For diamagnetic particles ($\chi_p < 0$) suspended in a paramagnetic medium ($\chi_m > 0$), $\Delta\chi$ is negative. Hence, the Kelvin body force reverses so that diamagnetic particles are transported to the magnetic field minima, also referred to as negative magnetophoresis.

2.4 Magnetic bioinks for single-cell manipulation and 3D cellular printing

The development of *in vitro* 3D cellular models is often inspired by an unmet medical need. For example, burn and tissue removal inspired the formation of adipogenic-differentiated 3D cellular structures for clinical applications and as models for obesity-related pathology.[98] Pre-fabricated 3D cellular structures composed of monotypic or co-culture assemblies are used as building blocks for larger tissue or organ printing.[50, 99, 100]

Common methods to engineer tissues *in vitro* typically require 3D bioprinting, which prints cell-laden hydrogels and permanent or sacrificial biological scaffolds for subsequent cell seeding. An ideal scaffold must be non-toxic to the cells, non-immunogenic in case it is implanted, have satisfactory mechanical properties, and facilitate appropriate tissue growth and differentiation. [101] However, the scaffold-based approach is expensive due to required additives to promote cell growth, and requires experienced personnel for operation and rigorous troubleshooting to optimize bioink printability and cell viability. Scaffold-based techniques can compromise the mechanical properties of the tissue construct and lead to poor cell compatibility during gelation.[102] Having a construct fully

composed by living cells may be advantageous in terms of preparation time for cell-cell interaction modeling in 3D tissues.

Alternatively, gravity-based approaches collect cells at an air-liquid interface, e.g., with the hanging-drop method, or on a rounded non-adherent surface.[103] These methods produce 3D cell clusters without using a scaffold and rely on intercellular interactions to produce ECM. Control over the size of the constructs is limited to cell number and viscosity of the medium to facilitate sedimentation. However, these passive techniques exercise little control over the final construct since they lack additional external forces to influence formation of the 3D cell clusters.

Magnetic printing is an emerging solution for engineering tissue constructs *in situ*.[104, 105] Cell-based magnetic bioinks have been used to form sophisticated cell patterns and unique geometries such as thick 3D cell clusters,[9] stacked co-cultures,[10, 106] rings,[9, 60] spheroids,[107] and linear structures.[90] The formation of 3D cell clusters with *positive magnetophoresis* requires cells to internalize or be labeled with MNPs, as described in **Figure 2.3**(**a**). To improve biocompatibility and limit cytotoxic effects, the MNPs are pre-coated with a biocompatible agent such as bovine serum albumin (BSA).[9] This provides the cells with positive magnetic susceptibility, moving them along the magnetic gradient from an inhomogenous magnetic field, towards a region of high magnetic field strength, thus allowing their manipulation via action-from-a-distance with a static or dynamic external magnetic field. As the cells coalesce and the 3D cellular structure matures, cell-cell interactions produce ECM so that the structure does not require an artificial scaffold.[9]

Alternatively, magnetic cell-laden bioinks can exist as label-free cell suspensions in a magnetically labeled cell medium (**Figure 2.3**(**b**)). With diamagnetic manipulation, the cells form 3D cellular structures rapidly. For label-free magnetic printing, a magnetic bioink is prepared by suspending diamagnetic cells in a paramagnetic medium. Here, cells that are intrinsically diamagnetic are suspended in a cell medium that is supplemented with a paramagnetic salt. This natural repulsion from a high magnetic field gradient forms the basis for *negative magnetophoresis*. In the presence of a magnetic field, the cells are displaced towards regions of lower field strength. Once the cells reach their equilibrium positions and synthesize sufficient ECM to hold their aggregated shape, the magnetic field is removed and the paramagnetic medium replaced with a regular, non-paramagnetic culture medium. Thereafter, the 3D cellular structure contracts due to intercellular interactions and then grows through cell proliferation.

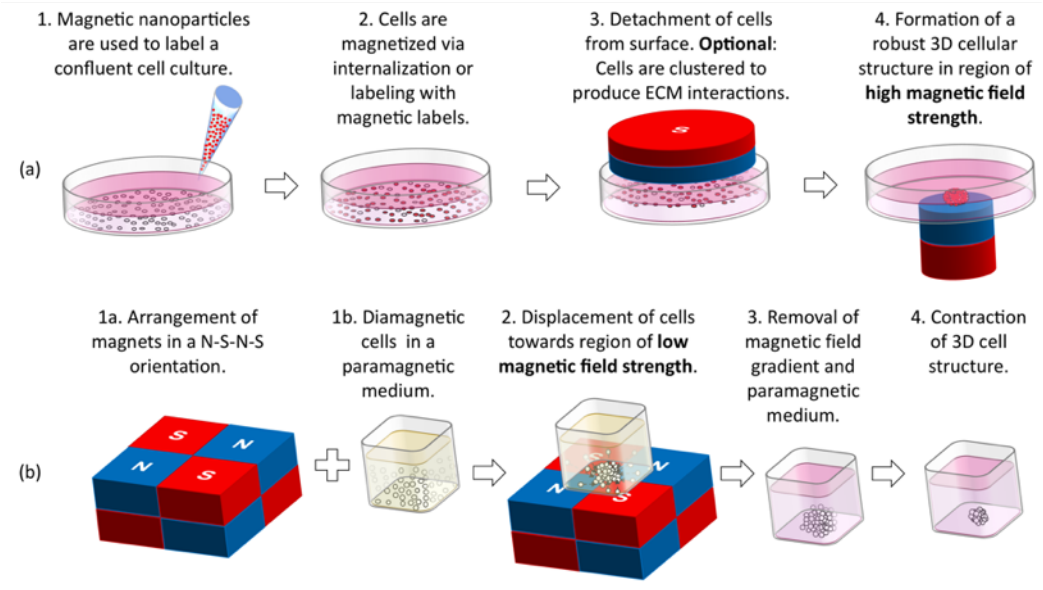

Figure 2.3: Printing of 3D spherical cellular structures using magnetic cell bioinks. (**a**) Magnetic printing of cells with positive magnetophoresis requires the diamagnetic cells to be labeled with MNPs to obtain a positive magnetic susceptibility. The magnetized cells are then detached from their tissue culture-treated surface. An optional step is sometimes implemented to levitate magnetized cells to the air-liquid interface to induce ECM formation. The resulting cell-cell interactions are broken by mechanical disruption. Finally, the presence of an inhomogeneous magnetic field concentrates the magnetized cells into the desired geometry at regions of high magnetic field strength, resulting in the formation of a 3D cellular structure. (**b**) Magnetic printing of cells via negative magnetophoresis, which displaces diamagnetic cells to regions of low magnetic field strength, is facilitated by the presence of paramagnetic salts. When sufficient cell-cell interactions have occurred, the inhomogeneous magnetic field and paramagnetic salt solution can be removed. The cell cluster continues to contract and form cell-cell interactions to form a stable 3D cellular structure.

2.5 Label-based manipulation of cells

During *label-based* magnetic manipulation, a magnetic particle is conjugated with a target molecule or cell, increasing the magnetic susceptibility of the target. A common label-based printing method tethers MNPs, such as magnetite (Fe_3O_4), to non-magnetic or diamagnetic materials, such as cells or microbeads. In the presence of an external inhomogeneous magnetic field, the magnetic particles and the particle-target conjugates are attracted towards areas of higher magnetic field strength. This attraction is experienced by

both ferromagnetic and superparamagnetic materials due to their positive magnetic susceptibility.

Commercially available MNPs consisting of iron oxides or nickel[108] are typically 1-100 nm in size and have high magnetic susceptibility that is conducive for manipulation.[109, 110] MNPs can be synthesized bottom-up through Massart co-precipitation,[109] oxidation of magnetic compounds,[111] biosynthesis,[112] or top-down by grinding a bulk material.[113] The magnetization of these nanoparticles is characterized by observing their magnetic hysteresis with a superconducting quantum interference device (SQUID) magnetometer.[9] MNPs can also be embedded into polymers to create magnetic aggregates (50-500 nm) or microspheres, also referred to as magnetic microbeads.[53, 95]

In vitro, MNPs are used to induce *in vivo*-like mechanical cues for self-organization and differentiation of tissues and [114] MNPs for clinical use must be biocompatible, have a strong magnetic polarization, and maintain colloidal stability during application. To maintain colloidal stability, MNPs are coated with biocompatible surfactants to prevent their agglomeration and, subsequently, ligands can be bound to their coated surfaces for labeling or use in separation.[50, 53] Computational models, such as COMSOL simulations, can be used to predict the final position and trajectory of label-based magnetic bioinks by determining areas of high magnetic flux density.[115-117]

MNPs are used in biosensor setups to quantify the presence and concentrations of a pathogen or a target molecule.[82] Microfluidic devices are used with MNPs to enhance the sensing capability of the system for low-volume samples.[118] While polymerase chain

reaction (PCR) and enzyme-linked immunosorbent assay (ELISA) are more accurate than other methods, they require long detection times, and expensive equipment and reagents. Some applications require rapid detection where sensing accuracy is less important. Here, functionalized MNPs are used to perform immunoassays that isolate cells and biological molecules from a suspension or solution,[119] such as influenza virus type A via antibody-[83] and aptamer-[120] based detection, the p24 capsid antigen for HIV-1 detection,[121] severe acute respiratory syndrome coronavirus 2 (SARS-CoV-2) spike and nucleocapsid proteins in buffer and untreated saliva,[122] *Salmonella* serogroup C_1 (O:6,7) antigens in blood- and stool-containing samples,[123] H5N1 virus in a continuous flow separation,[115] and *Escherischia coli* (*E. coli*) O157:H7 in food samples.[124] Alternatively, MNPs are used as chaperones to magnetize carbon nanotubes and align them into a conductive strip to detect antigens, such as c-Myc, in μL-sized sample volumes.[81] These techniques can be extended to offer the same benefits for single cell manipulation.

2.5.1 Single-cell manipulation

Magnetic cell separation captures target cells *in situ* using immunolabeled MNPs.[53, 125] For clinical applications, cell separation isolates and identifies diseased cells in a suspension containing both healthy and diseased cells, such as circulating tumor cells (CTCs) during cancer diagnosis and prognosis. Since the number of CTCs can be small, e.g., 10 cells/mL of whole blood, sensitive and selective detection is required.[94] Alternatively, a quadrupole magnetic field can be employed for effective cell separation. For clinical applications, sorted cell fractions may be recirculated back into the body.[74]

In a microfluidic device, the magnetophoretic capture and particle trajectories of microspheres are dependent on the dipole strength of the field-inducing electromagnet, magnetic susceptibility of the particles, particle diameter, fluid viscosity, flow velocity, microchannel dimensions, and distance of the dipole to the microchannel (**Figure 2.4**(**a**)).[126] These parameters can be used to design microfluidic devices for the magnetic separation of cells and biological molecules using microelectromechanical systems (MEMS) and bioMEMS for micro-total analysis systems (μ-TAS).[53] For instance, micropatterned Ni-Co alloy permanent magnets were arranged underneath a glass microchannel to separate Michigan cancer foundation-7 (MCF-7) cells from whole blood (**Figure 2.4**(**b**)).[94]

Single cells can also be manipulated in a hybrid co-culture/scaffold environment. Co-culture models often include non-diseased cells from the same tissue origin or stromal cells.[63] 3D cell culture models that incorporate a scaffold or co-culture can be used to evaluate cell-cell and cell-ECM interactions. In an investigation, normal human dermal fibroblasts (NHDF) were either magnetically patterned with the magnetite-labeled MCF-10A/*myr*-Akt1 and MD Anderson, metastatic breast sample 231 (MDA-MB-231) cancer cells using a pin-holder device to observe *direct* interactions, or introduced (non-patterned) within the collagen scaffold to observe *indirect* interactions (**Figure 2.4**(**c**)).[54] This established a platform to observe complex tumor microenvironment (TME) interactions during *in vitro* screening.

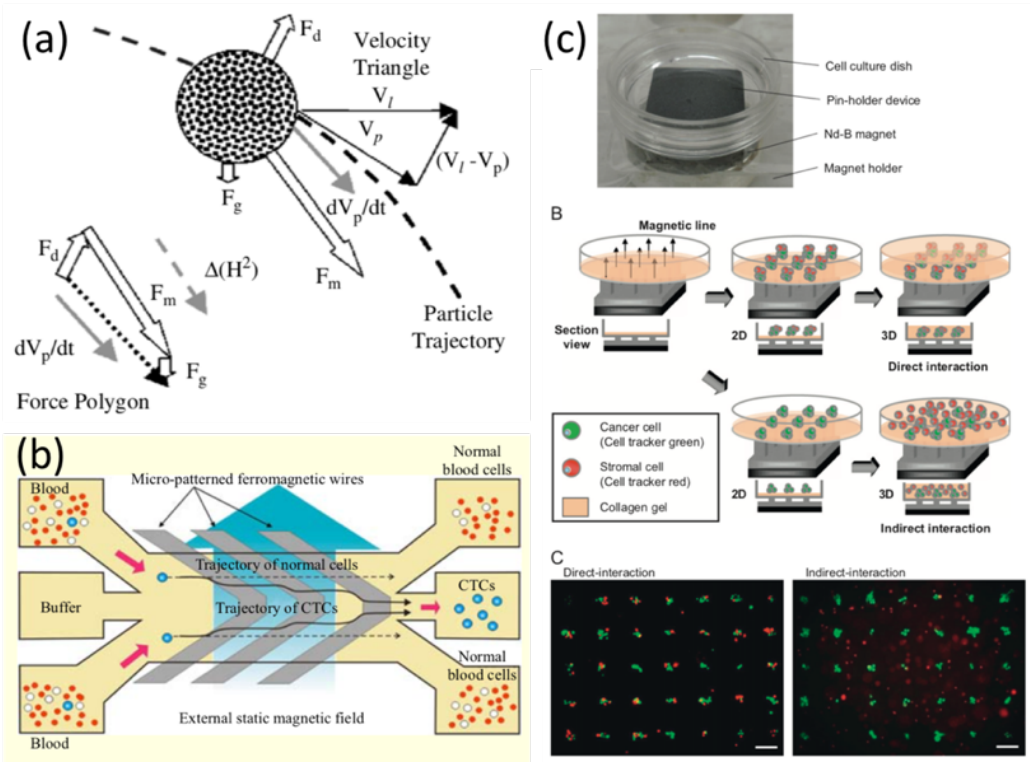

Figure 2.4: Label-based single-cell manipulation. (**a**) The force vectors acting on a magnetic microsphere inside a microfluidic channel. Reprinted from Ref. 126. (**b**) Schematic diagram showing the working principles of a microdevice for separation of circulating cancer cells (CTCs) using lateral magnetophoresis and immunomagnetic nanobeads. Reprinted from Ref. 94. (**c**) Magnetic force-based cell patterning using the pin-holder device for observation of cancer cells behavior with associated fibroblasts in their 3D microenvironment, direct- and indirect-interaction models (scale bar: 200 μm). Reprinted from Ref. 54.

2.5.2 Formation of 3D cellular structures

A commercially available magnetic label composed of gold nanoparticles, iron oxide and poly-L-lysine was used with various cell lines to form 3D *in vitro* cellular models by non-specific labeling of the cell membrane. Other examples include co-cultures of human breast cancer (SUM159 and MDA-MB-231) with human fibroblast (293T and Hs578bst) cell lines for the study of tumor-stroma interactions,[1] 3T3 murine embryonic fibroblasts to demonstrate spheroid size as a metric for cytotoxicity,[107] a bronchiole co-culture model,[10] a model to study white adipose tissue (WAT) development and growth using 3D cultures consisting of (1) monotypic adipospheres composed of mouse preadipocytes (3T3-L1) to observe adipogenic differentiation, (2) co-cultures with endothelial bND.3 cells to observe the formation of vessel-like structures and (3) mouse primary WAT cells to observe the expression of phenotypic markers,[127] smooth muscle cells (SMC-A and SMC-B) formed into rings to study uterine contractility,[128] tumors of the liver and breast to study the effectiveness of photodynamic therapy (PTD),[129] and human aortic smooth muscle cells (ASMC) formed in a ring structure to demonstrate functional vasoactivity.[60]

Magnetic cell printing can be used in combination with artificial scaffolds or in a co-culture to replicate physiological phenomena such as a heterogeneous TME.[13, 130] Here, the use of a scaffold provides the opportunity to observe the effects of paracrine signaling[13, 131] and simulate tissue rigidity which orchestrates mechanosensing.[132, 133] While a scaffold is necessary to model non-cellular components[130] and mimic the TME, it also provides control over the conditions of the ECM[13] factors that influence tumor progression. Magnetic labels in the form of bioinorganic hydrogel composed of bacteriophage,

magnetite, and gold have also been used to form 3D structures composed of highly-invasive human glioblastoma (U251-MG) and normal astrocyte (LN-229) cells.[134] At 48 hours, the monotypic glioblastoma 3D culture showed similar expressions of N-cadherin to a mouse xenograft. In a confrontation assay, the co-culture demonstrated invasiveness of the glioblastoma spheroid into the astrocyte structure.[134]

The formation of 3D cellular structures is not limited to mammalian cells. The 3D magnetic printing of *E. coli* and *Staphylococcus aureus* (*S. aureus*) was facilitated by the internalization of sugar-coated MNPs to form spheroid, ring and flat disc-like structures using NdFeB 52 (N52) magnets.[135] Here, glucose, galactose, maltose, and sucrose coated MNPs were shown to have no toxic effects on the bacteria cultures. The use of glucose-coated MNPs was shown to effectively modulate the swarming process of an *E. coli* liquid culture to promote biofilm formation and allow for subsequent studies.

2.5.3 Fabrication of engineered tissues

3D cell clusters are evaluated by their genetic and proteomic profile expressions. Although reliable, the complexity of unique expressions for different cell lines limits their use as metrics to provide an exhaustive list of markers that evaluate whether a cluster of cells has successfully formed a tissue. In addition, patient samples and immunological profiles may differ based on their differentiating characteristics[128, 136] that cannot be therefore compared with an engineered sample. Conventional slicing methods, such as staining and confocal microscopy,[60] are limited in their ability to distinguish microarchitecture, intercellular interactions, and tissue morphology.[9]

Label-based magnetic printing has revealed the resemblance of 3D cell clusters formed with internalized BSA-coated Fe_3O_4 particles to *in vivo* tissues.[9] Independent cultures of human lung fibroblast (HLF-1) and human prostate cancer epithelial (PC-3) cells were arranged in various geometries to verify that the 3D cell clusters faithfully represent *in vivo* tissue using universal indicators of tissue formation: intercellular interactions and tissue morphology.[9] Morphologically, 3D cell clusters are more spheroidal than their 2D controls and the results verified that 3D magnetic printing enhanced intercellular interactions mediated by extracellular fibers, which is typical of tissues *in vivo*. The evolving morphology of a ring-like 3D cell cluster was also investigated. PC-3 and HLF-1 cells organized into a multi-layer sheet morphology while HLF-1 cells depicted spheroidal morphology. These arrangements are typical of epithelial and fibroblast morphologies *in vivo*, respectively.

Co-cultures have been used to form an aortic valve composed of valvular interstitial cells (VICs) and endothelial cells (VECs) extracted and isolated from a porcine heart.[106] Magnetic labels were used to levitate labeled cells at the air-liquid interface of the cell culture suspension, forming disk-like structures of each cell line within 4 hours. These individual cell disks were then stacked on each other, with the VECs atop VICs. The interactions between the two disks took an additional 4 hours, totaling 8 hours of formation for the aortic valve co-culture (AVCC). Following 3 days of levitation, the AVCCs were harvested for phenotypic and functional biomarkers by immunohistochemistry staining and gene expression profiles, respectively. These miniaturized tissue constructs demonstrated the potential of magnetic levitational assays to form representative 3D tissue models. The

AVCCs maintained the phenotype and functions of each cell line after co-culture formation and expressed relevant ECM markers. The rapid formation and relevant expressions observed in these AVCCs are encouraging the potential formation of other tissue constructs for *in vitro* modeling of diseases.

A similar co-culture assembly process was used to form an airway-to-circulation facing bronchial wall using a magnetized Teflon pen that assembled monotypic 3D cultures into a stacked structure.[10] A stacked layer of epithelial cells, smooth muscle cells (SMCs), pulmonary fibroblasts, and pulmonary endothelial cells was used to create a bronchial co-culture model. Although the use of these cell lines in a co-culture is not unique, this study demonstrated asymmetrical ECM formation (with emphasis on collagen type I), physiological phenotypic markers, and cell morphologies for the first time.

MNP chaperones can also be utilized to form tissue-like structures using spheroids as building blocks, as demonstrated by first forming spheroids composed of primary rat aortic smooth muscle cells (SMCs) and magnetoferritin, a less-toxic alternative to iron-based MNPs. These spheroids were then used to form a ring structure on the order of 10 mm within 4 days.[61]

Simulations of two common geometries and experimental setups used for magnetic cell printing using label-based methods are shown in **Figure 2.5** for spherical (**a** and **c**) and ring structures (**b** and **d**). For each geometry, the 3D cellular structures are realized by various cell lines (**e-i**), emphasizing the versatility of magnetic cell bioinks to form desirable geometries using various cell lines.

The formation of 3D cellular constructs within a scaffold is possible with label-based methods. Red- and green-fluorescent MNPs were used to label human umbilical vein endothelial cells (HUVEC) and MSCs, respectively, to intentionally position them on opposing sides of a pre-printed scaffold composed of bioresorbable Fe-doped hydroxyapatite (FeHA) poly(ε-caprolactone) (PCL) to create a heterogeneous multicellular construct. These magnetic scaffolds produce highly ordered cell seeding and, with the combination of cells used, is expected to promote the reconstruction of bone microarcitecture.[116] Magnetically-labeled cells can also be suspended in a liquid biomaterial, positioned according to the external magnetic field, and fixed into their final geometry as the biomaterial solidifies. This was demonstrated using human induced pluripotent-stem-cell-derived cardiomyocytes (hiPSC-CMs) in a low-density collagen suspension, formed into ring, parallel gradient and circular geometries. The ring and circular structures were then grafted to a rat heart following solidification of the collagen (by temperature), which did not alter the native cardiac function after 2 and 8 days. These integrated label-based magnetic printing methods with a scaffold provide alternative solutions to the fabrication of complex tissue morphologies.[117]

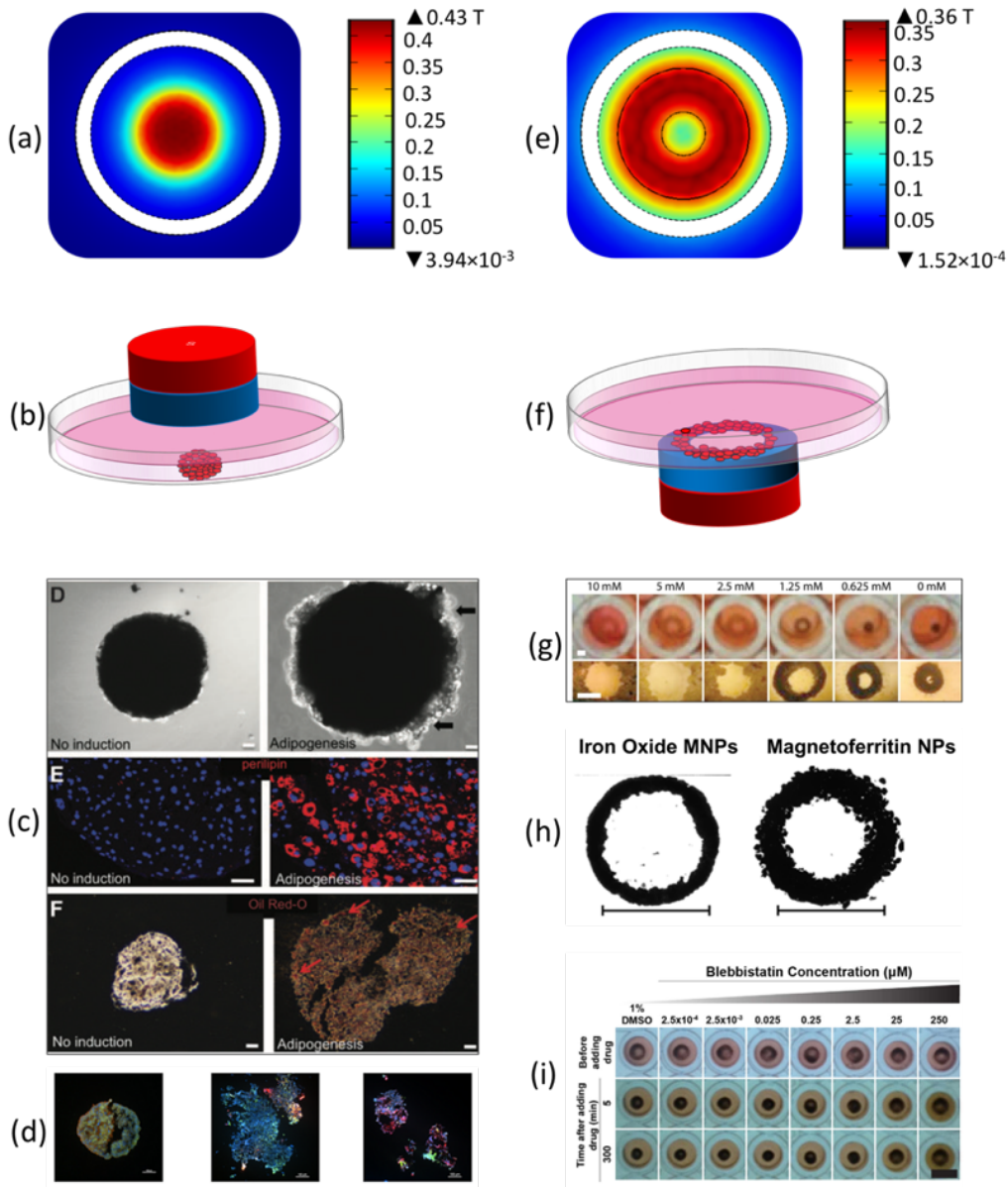

Figure 2.5: Label-based contactless formation of 3D cellular structures formed with magnetic cell bioinks. (**a**) Magnetic flux density distribution at the surface of the magnet arrangement using an N52 cylindrical/rod magnet on top of a 24-well plate, where the field shown is caused by a separation distance of 1 mm between the surface of the liquid and the magnet resulting in a region of the maximum magnetic

flux density at the center and (**b**) a schematic of its corresponding experimental setup. Single, spherical 3D cellular structures formed using a cylindrical magnet above the cell culture composed of (**c**) 3T3-L1 cells after 8 days of levitation with and without induction for adipogenic differentiation (scale bar: 100 mm; reprinted from Ref. 127); and (**d**) a mixed co-culture composed of 70% MDA-MB-231 (green) and 30% fibroblast (red) cells (Hs578bst, HFP or CAF) that are self-distributed after 3 days of culture (scale bar: 100 mm; reprinted from Ref. 1). (**e**) Magnetic flux density distribution in the *x*-*y* plane using an N52 ring magnet beneath a 96-well plate resulting in a region of maximum magnetic flux density on at the surface of the ring, and (**f**) schematic of its corresponding experimental setup. 3D cellular ring structures formed using a ring magnet underneath the cell culture composed of (**g**) HEK293 cells treated with ibuprofen (scale bar: 1 mm; reprinted from Ref. 137); (**h**) a fused ring-shaped tissue formed by primary rat aortic smooth muscle spheroids chaperoned by iron oxide MNPs or magnetoferritin nanoparticles (scale bar: 10 mm; reprinted from Ref. 61); and (**i**) A10 rat vascular smooth muscle cells in response to various concentrations of blebbistatin (scale bar: 5 mm; reprinted from Ref. 60). For (**a**) and (**e**) the magnet is denoted by solid black lines while the well plate boundaries are denoted by a white void outlined by dashed black lines.

2.6 Label-free cell manipulation

Label-free magnetic manipulation utilizes the intrinsic magnetic susceptibility of the material, where both *positive* and *negative magnetophoresis* are possible while respectively manipulating magnetic and diamagnetic particles. For example, when whole blood is

subjected to an external magnetic field, oxygenated red blood cells (RBCs) experience positive magnetophoresis while white blood cells (WBCs) experience negative magnetophoresis.[138]

Since the magnetic susceptibility of diamagnetic materials is typically much weaker than paramagnetic materials, a diamagnetic material can be suspended in a paramagnetic solution, where the two can be separated by an applied magnetic field. The label-free manipulation of objects is also possible in non-magnetic mediums such as air, which can even lift small animals such as frogs and mice, although the magnetic strength required is not safe without protective equipment.[73] It is also possible to manipulate the orientation of diamagnetic objects by simply rotating an imposed dynamically changing magnetic field gradient.[139]

The geometry of the final printed construct or position in 3D space can be designed using simulation software,[2, 49, 140] and analytical models[72] to devise intentional arrangements of the external magnetic field. These models can also predict the time particles take to reach their equilibrium positions by simulating the influence of the different magnetic susceptibilities of the paramagnetic and diamagnetic entities in suspension, and the distribution and strength of the inhomogeneous magnetic field gradient that determines the geometry of the printed construct.[88] However, the models do not typically account for fluid recirculation and, in the case of cell printing, neither do they include biological activities during printing, such as cell-cell and cell-substrate interactions.[62] Modification of these models to account for biological activity, such as the

production of ECM, different cell lines, or types of cells will significantly improve the predictive ability of these tools.

2.6.1 Single-cell manipulation

Single-cell manipulation through negative magnetophoresis exploits the intrinsic diamagnetic properties of target cells in a heterogeneous cell suspension. The inherent differences in the densities of different cells or their status based on cellular events can be used to establish distinct levitational heights that serve as biophysical markers (**Figure 2.6**(**a**)).[67-70]

The combination of microfluidic channels and a magnetic field enhances cell separation in a homogeneous cell suspension.[50] Through the application of a high-gradient magnetic field (HGMF) produced by magnetic microstructures, whole blood fractionation was demonstrated utilizing the intrinsic magnetic susceptibilities of RBCs and WBCs.[138] The diamagnetic WBCs moved towards regions of low magnetic field strength while RBCs, being paramagnetic due to Fe^{3+} in methemoglobin, the oxidized form of hemoglobin, moved towards regions of higher magnetic field strength. This label-free cell separation is a basic design for clinical devices for whole blood fractionation.

Cells can also be suspended in a paramagnetic medium to enhance label-free manipulation. Human histolytic lymphoma monocytes (U937) have been separated from RBCs in a Gd-DTPA suspension contained in a polydimethylsiloxane (PDMS) microchannel (**Figure 2.6**(**b**)).[141] Based on theoretical analysis, as the concentration of Gd-

DTPA was increased from 0 to 80 mM, the separation of U937 and RBCs also increased, which is in good agreement with experimental measurements.[141]

Single living cells from a variety of organisms including mouse (NIH/3T3), yeast (*Saccharomyces cerevisiae, S. cerevisiae*), and algae (*Chlamydomonas reinhardtii, C. reinhardtii*) have been successfully levitated by suspending them in a solution of 40 mM Gd-[91] A suspension of Jurkat cells (human T lymphocytes) in 5-10 mM of GdDO3A was levitated above an Nd micromagnet array,[142] while *S. cerevisiae* was levitated in 20 mM Gd-DTPA with a CoPt micromagnet array (**Figure 2.6(c)**).[92] In a non-paramagnetic liquid nutrient broth, *E. coli* and *Staphylococcus epidermidis* (*S. epidermidis*) were levitated to study population growth.[143] The positioning of the levitated cells followed the magnetic field gradient. These magnetic cell traps have the potential to fabricate biological microsystems in lab-on-chip devices.[86]

Cells can also be suspended in a medium containing MNPs for label-free printing. An example is the use of a ferrofluid containing BSA-coated iron oxide MNPs to form linear cellular chains of HUVEC within minutes of applying a magnetic field (**Figure 2.6(d)**).[144] This form of label-free cell manipulation with a ferrofluid utilizes the higher magnetic susceptibility of the ferrofluid in comparison to a paramagnetic salt solution and avoids the cytotoxicity associated with internalized or attached MNPs. The MNPs are not used as labels by either attachment or internalization. Instead, the dipoles of the ferrofluid particles shepherd the cells into linear chains. The morphology of the patterned linear chains is unchanged upon removal of the external magnetic field or the ferrofluid. Control of the patterned linear structure is possible by changing the ferrofluid particle

concentration. Culturing endothelial cells in linear chains produces capillary-like structures, a formidable challenge for tissue engineering.[144]

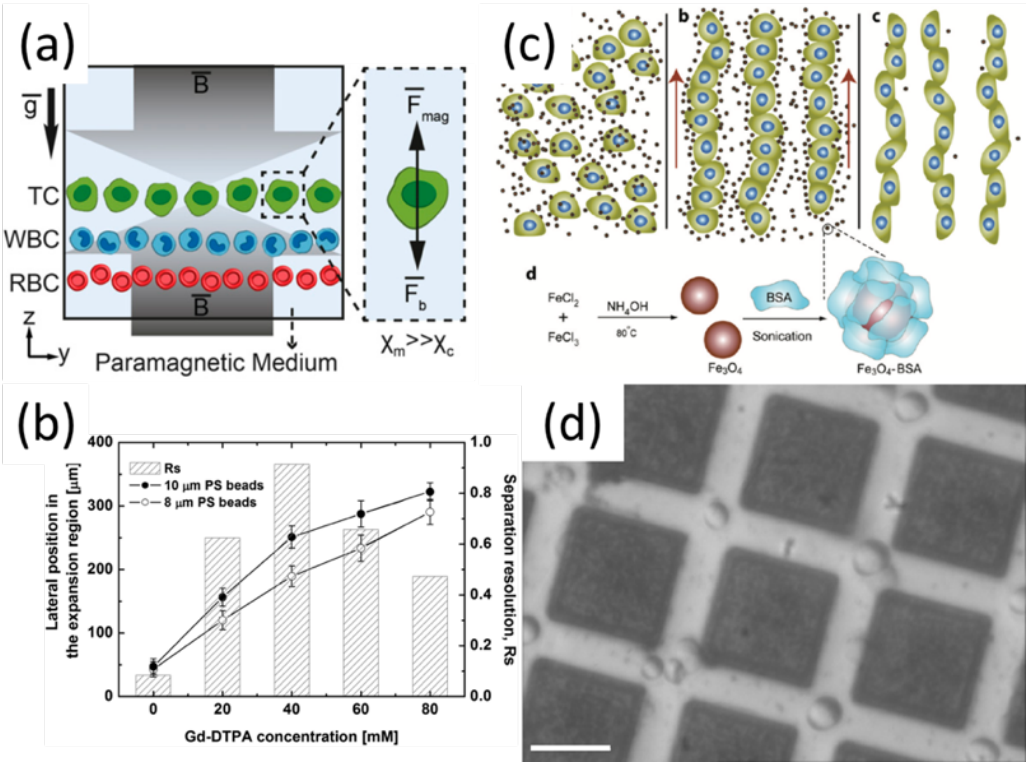

Figure 2.6: Label-free single-cell manipulation. (**a**) Final equilibrium height of cells in a paramagnetic medium. Due to magnetic induction (B) and gravity (g), cells are levitated in the channel and focused in an equilibrium plane where the magnetic ($\mathbf{F_{mag}}$) and buoyancy forces (F_b) equilibrate. The magnetic susceptibility of the medium (χ_m) is higher than the cell magnetic susceptibility (χ_c). Thus, different cell types with different densities, such as tumor cells (TC), WBC, and RBC, are separated from each other. Reprinted from Ref. 67. (**b**) Measured lateral positions and separation resolutions (Rs) of polystyrene (PS) beads with two different sizes in the expansion region according to Gd−DTPA concentration.

Reprinted from Ref. 141. (**c**) Schematic of the cell chain formation process in a ferrofluid. Reprinted from Ref. 144. (**d**) Diamagnetic trapping of yeast cells (*Saccharomyces cerevisiae*) on a CoPt micromagnet matrix electroplated on a silicon wafer with magnet dimensions of 8 x 25 μm, separated by a 10 μm gap between two adjacent magnets (scale bar: 20 μm). Reprinted from Ref. 92.

2.6.2 Formation of 3D cellular structures

Single cells suspended in a paramagnetic medium can be manipulated to form 3D cellular structures.[50] Polymeric beads have been used as cell surrogates to display the final printed construct.[66, 88] A proof-of-concept method of 3D diamagnetophoretic cell printing used whole blood and a paramagnetic solution of Gd-DTPA in PBS (**Figure 2.7**(**c**)).[62] WBCs and whole blood were examined separately for toxicity of Gd-DTPA. Various cell geometries were achieved by rearranging N52 magnets, where a line and three-pointed star were produced in circular vials. Simulations of the probable shape of the 3D cellular structure predicted equilibrium cell positions where the magnetic field strength was lowest. Similar to previous reports,[145] circular cell clusters were formed on top of a magnet array but were contained in a rectangular vial with 1 mL of paramagnetic solution. Increasing the distance between the vial and the magnet array decreased the effective magnetic field strength that increased the dimensions of the resulting clusters.[62]

3D and 2D morphologies using MCF-7 cell bioinks and HUVEC cells, respectively, were printed together on tissue culture-treated (TCT) surfaces, where these surfaces promoted cellular adhesion.[65] To produce co-cultures, HUVECs were used first to form a

2D monolayer in a regular culture medium without using a magnet. Subsequent replacement of the medium with an MCF-7 magnetic bioink and the use of magnet quartets facilitated the formation of a 3D cellular structure. Over time, cells on the periphery of the 3D cellular structure adhered to the TCT surface and interacted with the HUVECs to display a unique composite 2.5D morphology, namely, a 3D tumor adjacent to a 2D region containing endothelial cells that represents a metastatic tumor interacting with the vasculature. This method requires no moving parts and can be completed entirely *in situ*.[65]

The conditions affecting the formation of 3D cellular structures through diamagnetic printing have been identified.[64] MCF-7 cells were used as the biological elements of a magnetic bioink and, using diamagnetic printing, monotypic 2.5D and 3D cell structures were formed on TCT and ultra-low attachment (ULA) surfaces. These were compared by measuring their maximum projected areas and gene expressions for hypoxia-inducible factor 1-alpha (*HIF1α)* and vascular endothelial growth factor (*VEGF*). The formation time for both 3D and 2.5D cell structures was 6 hours. Such rapid formation has not been observed with other methods without adding components to the culture medium that accelerate 3D cell structure formation. Both 3D and 2.5D cell structures formed through magnetic printing had Gaussian distributions of their maximum projected areas, confirming that the method is both rapid and highly reproducible. The sequence of experimental controls was followed for subsequent studies to prevent over-exposure to the paramagnetic agent and minimize toxicity to the cell inks.

Multi-layered 3D cellular structures have also been printed by diamagnetophoresis, where the first *in situ* proof-of-concept utilized an MCF-7 magnetic cell bioink to form a

3D cellular structure (**Figure 2.7**(**b**)).[55] Subsequently, a mouse embryonic fibroblast cell line (3T3) magnetic bioink was used to form a second layer, around and above the MCF-7 structure. This label-free arrangement of cells has the potential to produce tissue architectures such as skin, liver, and tubular structures such as the gastrointestinal tract.[55]

3D co-cultures have also been produced with bioinks composed of 3T3 and MDA-MB-231 cell bioinks (**Figure 2.7**(**a**)).[63] Due to its triple-negative expression of estrogen, progesterone receptors, and human epidermal growth factor 2 (HER2), MDA-MB-231 is a clinically significant cell line for *in vitro* study, but this cell line is notoriously difficult to grow in 3D. Instead of producing an organized cell pattern, the two cell lines were mixed in different ratios. This study demonstrated the accelerated formation of 3D cellular structures and their reproducibility as the proportion of fibroblasts increased when printed with magnetic cell inks. For the first time, a 3D MDA-MB-231 cellular structure was formed by magnetic printing within 24 hours without using additional reagents or an artificial scaffold, whereas 48 hours were required for their formation through gravity. Reproducibility for all monotypic and binary mixtures was also higher for magnetic printing. The investigation verified the conceptual use of fibroblasts as a glue to promote cell adhesion, confirming their potential for studying clinically relevant cell lines or primary cells for disease modeling and personalized medicine.[63]

Typically, 3D cellular structures produced through label-free magnetic printing are formed in microfluidic devices or low-volume multiwall plates, making it difficult to handle medium replenishment. Recently, spheroids were formed using a high volume (800

μL) and low concentration of Gd.[146] This is a new fabrication method for the high-throughput formation of individual 3D spheroids for downstream applications.

2.6.3 Fabrication of engineered tissues

Diamagnetic repulsion produces larger, multicellular constructs using prefabricated 3D cellular structures as building blocks. The patterns produced from merging prefabricated spheroids can be predicted and coded for according to their surface tension.[140] Bone marrow stem cell spheroids (D1 ORL UVA) formed with a ring magnet were sequentially arranged into a cluster in a suspension of 200 mM Gd^{3+}. As the number of spheroids increased, the overall area of the merged cluster also increased. In a supporting experiment, adipogenic-differentiated mouse osteoblasts (7F2) spheroids were formed in 100, 150, and 200 mM gadobutrol (Gadavist), a chelate of Gd^{3+}. As the concentration of Gd^{3+} decreased, the projected areas and perimeters of the structures increased.[66] This suggests that the magnetic strength of the medium and the number of building block units can be optimized to construct 3D clusters of varying densities and dimensions. These same cell lines had been used previously to produce 3D monotypic and layered co-culture using a microcapillary platform[98] and as monotypic cultures in a horizontal levitation system.[147]

A functional tubular construct can be formed using a combination of magnetic levitation and acoustophoresis.[2] Here, tissue spheroids composed of human bladder smooth muscle cells (hbSMCs, myospheres) were produced in a day using gravity in non-adherent microwells. Following their assembly, the tissue spheroids were pooled together and suspended in a solution containing 20 mM gadobutrol. This suspension was contained in a

single cylindrical vessel inside an acoustic apparatus, which was itself placed inside a Bitter magnet. The assembly began by applying the magnetic field, which levitated the pooled spheroids in their culture vessel. To compensate for the low paramagnetic salt concentration, a high magnetic field intensity of 9.5T was required. Once levitated, an acoustic radiation force was used to distribute the tissue spheroids vertically to form a solid tube. Both the external magnetic and acoustic body forces were held for 8 hours to facilitate the fusion of the tissue spheroids into a tubular construct. To demonstrate functionality, the tubular hollow tissue-engineered structures were then exposed to 50 nM of endothelin-1 for 2 hours, which caused the tube to contract by 20% as compared to the control (no endothelin-1). This method of hybrid magnetoacoustic levitation makes it possible to bypass traditional techniques that require a scaffold, removing the need for artificial materials that can complicate bioprinting and introduce foreign compounds to the tissue construct.[2]

Magnetic printing can be expanded to produce 3D cellular assemblies in hydrogels and biological scaffolds using label-free methods. Prior to crosslinking a hydrogel, magnetic 3D cellular assembly can occur by magnetizing the hydrogel with appropriate concentrations of a paramagnetic salt or MNPs. This printing capability can be adjusted by increasing the concentration of magnetic material with increasing viscosity to facilitate rapid coalescence of the suspended cells. This ability to form 3D cellular constructs within material is a significant capability that can mimic mechanical stimulants, allowing the observation of unique cell-cell interactions. Without embedded MNPs, UV-cross-linkable hydrogel and polyethylene glycol (PEG) display paramagnetic behavior in a solution of

PBS. As the UV exposure is applied to crosslink the PEG hydrogels, their magnetic susceptibility also increases, attracting them to a magnet.[56]

Multistep mathematical and computational analyses have been performed to investigate the effects of magnetic susceptibility, hydrogel size, and distance from an external magnetic field.[56] Levitation increased with increasing magnetic susceptibility and the size of the paramagnetic gel. As the distance between the magnet and the hydrogel decreases, the magnetic force intensity acting on the hydrogel increases. To demonstrate superior control and intentional organization *in situ*, hydrogel units of varying dimensions were produced and arranged into linear shapes, and up to five units were used to form layered 3D structures.

Bottom-up tissue engineering can also be accomplished using cell-laden hydrogels levitated in a paramagnetic medium.[43, 56, 148] The levitation of hydrogels, including gelatin methacrylate (gelMa) and polyethylene glycol dimethacrylate (PEGDA), was demonstrated by fabricating microgels into 3D millimeter-scale assemblies. The size of the 3D assembly decreased over time and increasing Gd^{3+} concentrations and increased by increasing the number of microgels. The levitation height is a function of PEGDA density, where gels with lower precursor compositions levitated at a higher equilibrium height. Mouse fibroblast cells (NIH/3T3) were encapsulated in gelMa microgels and assembled into 3D assemblies, where they remained viable and produced ECM during their 7-day culture.[43] Cell-laden PEG also demonstrated the viability of NIH/3T3 cells for 10 days.[56]

The printing of 3D cellular structures is also possible *within* a hydrogel matrix. This was demonstrated by using polystyrene beads, followed by hollow poly(d, L-lactide-co-glycolide) (PLGA) drug delivery microcapsules and bovine MSCs.[147] Here, methacrylated hyaluronic acid (MeHA), a photo-cross-linkable hydrogel, was prepared with a solution of 200 mM gadodiamide (Gd) and a photoinitiator (0.5% w/v lithium phenyl-2,4,6-trimethyl-benzoyl phosphinate, LAP). Like magnetic printing in a fluid medium, diamagnetic objects were suspended in the solution and guided to areas of lowest magnetic field strength by an inhomogeneous magnetic field. Once the desired geometry was achieved, the hydrogel was crosslinked and the cell positions fixed. To reduce Gd toxicity, the crosslinked cell-laden hydrogels were washed to promote Gd release. the viability of the cells remained uncompromised during six weeks of observation and the printed geometry exhibited depth-dependent cellularity similar to native cartilage tissue.[149]

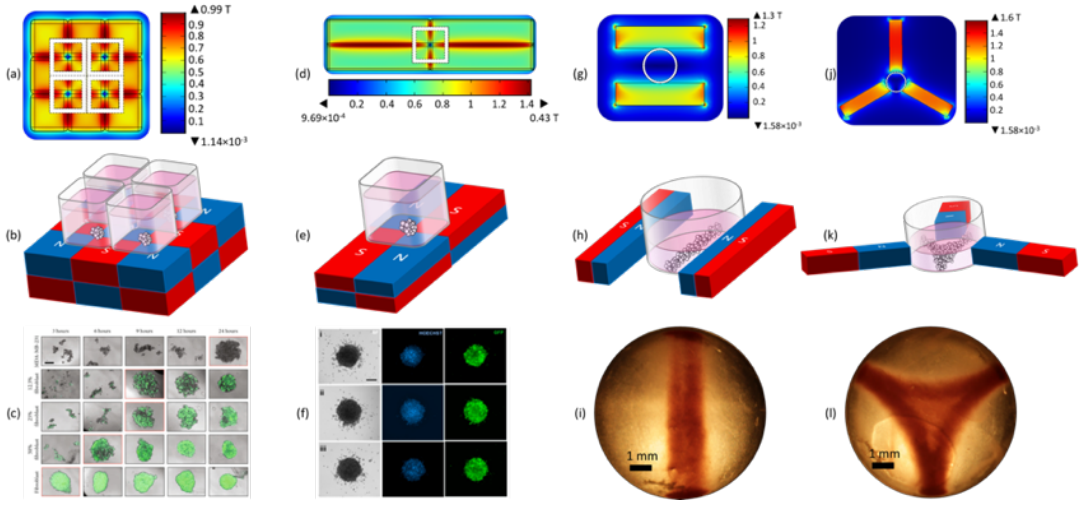

Figure 2.7: Label-free, contactless formation of 3D cellular structures formed from magnetic cell bioinks. (**a**, **d**, **g** and **j**) Magnetic flux density distribution at the

surface of the magnet arrangement, where the magnet is denoted by solid black lines while the well plate boundaries are denoted by a white void outlined by dashed black lines, (**b**, **e**, **h** and **k**) experimental setups, and realizations for (**c**) a spherical 3D cellular structure composed of various ratios of MDA-MB-231 and 3T3 (GFP+) cells formed on a ULA surface using four N52 4.5mm^3 magnets in N-S-N-S orientation, resulting in a minimum magnetic flux density at their intersection (scale bar: 100 mm; reprinted from Ref. 63); (**f**) a layer-on-layer structure formed from MCF-7 (core) and 3T3 cells (shell) on a hydrophobic plate using a magnet quartet in N-S-N-S orientation, resulting in a minimum magnetic flux density at their intersection (scale bar: 200 mm; reprinted from Ref. 55); (**i**) a line and (**l**) a three-pointed star composed of whole blood formed in a cylindrical glass cuvette using three and two rod magnets, respectively (scale bar: 1 mm; reprinted from Ref. 62).

2.7 Concerns and future outlook

2.7.1 Nanoparticle safety

The use of iron oxide nanoparticles is abundant in magnetic bioprinting. Iron is found naturally in red blood cells (RBCs) in the form of a heme molecule. Iron oxide nanoparticles can be metabolized by heme oxygenase-1 to form blood hemoglobin and hence maintain iron-cell homeostasis by entering the body's iron store as ferritin, and are generally considered biocompatible.[150, 151] To emphasize their safety and biocompatibility, the addition of iron oxide and titanium dioxide nanoparticles in tinted mineral sunscreens (applied topically) can effectively protect against UV and visible light.[152, 153] Due to their

superior magnetic properties and biocompatibility, superparamagnetic iron oxide nanoparticles (SPIONs) are often used as materials for magnetic fluid hyperthermia (MFH).[154]

In addition, the use of iron oxide nanoparticles has been shown to improve the imaging ability of MRI,[117] suggesting that conjugation with target-specific antibodies may further improve diagnosis and simultaneously heat to destroy tumors.[77] This therapeutic technique is also observed for magnetic drug targeting (MDT) through the use of hollow, nanoporous microspheres impregnated by MNPs and a drug.[52] These immunolabeled microspheres respond to an external stimulus, controlling the release of the chemotherapeutic agent. This delivery enhances drug efficacy and limits non-specific delivery of the medicinal entities to healthy regions of the body. Mathematical models can describe MDT *in vivo*.[155] As with all materials, the route of administration and dose are indicators of exposure and potential toxicity. *In vivo*, iron-based nanoparticles are shown to have organ-specific accumulation and toxicity towards the brain, lung, heart, reproductive systems, hypothalamus (endocrine response), and the immune system.[156]

The use of alternative materials can address the toxicity concerns associated with MNP internalization *in vitro*. The cytotoxicity of iron oxide nanoparticles was evaluated for two human glioblastoma cell lines (T98G and U251), a human urinary bladder carcinoma cell line (ECV304), and a mouse fibroblast cell line (BALB/3T3).[157] Here, magnetite nanoparticles were coated with rhamnose, a deoxy sugar, to induce cellular uptake and, due to the lack of standardized procedures for nano-sized materials, evaluated using various methods. A concentration of 100 μg Fe/mL was found to induce a cytotoxic

response, resulting in an average 35% cell death in the three cancerous cell lines due to mitochondrial damage. No cytotoxicity was observed for the fibroblast cell line.[157] For 3D magnetic printing via positive magnetophoresis, magnetoferritin (apoferritin-coated iron oxide nanoparticles) has been shown to improve cell viability compared to iron oxide MNPs and is considered to be a more biocompatible option. This is due to the activity of apoferritin that facilitates the oxidation of Fe(II) for subsequent iron storage by ferritin, an abundant protein found in our body that acts as an iron reserve.[61]

2.7.2 Gadolinium safety

Paramagnetic salts include different chelates of Gd^{3+} such as gadopentatic acid (Gd-DTPA) [55, 62-65, 81] and gadobutrol (Gd-BT-DO3A),[80, 90] and manganese salts such as manganese chloride ($MnCl_2$).[49] These agents must be selected after careful consideration of their toxic effects on cells. Short-term studies of 3 days on a monolayer of MCF-7 cells determined that exposure to 25 mM Gd-DTPA did not significantly reduce cell viability.[64] A similar evaluation of MDA-MB-231 and 3T3 cell monolayers established that 25 mM Gd-DTPA was safe for MDA-MB-231 and co-culture populations at 24 hours of exposure. However, subsequent long-term studies over 2 weeks determined that Gd-DTPA inhibited the growth of the 3D cellular structures even though the exposure had been within pre-determined limits.[63] Therefore, it is not appropriate to assume long-term safety from short-term studies. In a separate investigation, Gd-DTPA has been shown to behave as a xenoestrogen when used with MCF-7, an estrogen receptor (ER) positive breast cancer cell line.[71] At low concentrations of Gd-DTPA (0.1 and 1 mM), proliferation and cell migration increased.

This was not observed for the ER-negative cell lines, MDA-MB-231 and aneuploid mammary epithelial (Hs 578T).[71]

Chelates of Gd^{3+} influence cell morphology, which can affect intercellular interactions required for 3D cellular structure formation. For example, MCF-7 cells exposed to 25 mM of Gd-DTPA in a culture medium for 24 hours do not produce significant changes in their cell morphologies.[64] Here, concentrations of 50 mM and above that show less evidence of cell-substrate adhesion interactions were omitted from diamagnetic printing. Gadobutrol, however, has a less significant effect on the biomechanics of 3D cellular structures, where 250 mM of the substance decreased the elastic modulus of the 3D cellular structures significantly, but 20 and 50 mM did not.[2] When assembled, none of these gadobutrol concentrations influenced the fusion rate of the tissue spheroids within 24 hours.

In vivo, Gd-based MRI contrast agents have been used with caution, due to the development of nephrogenic systemic fibrosis (NSF) observed in patients with renal impairment.[158] Although accumulation of non-chelated Gd^{3+} ions is reported in numerous tissues, little is known regarding the exact mechanism of toxicity.[159] It is considered that non-chelated Gd^{3+} ions interact with macrophages and fibroblasts to incur damage to healthy tissue.[160] Aside from stronger chelation, methods of minimizing Gd^{3+} ion toxicity could be achieved by delivery through a nanoparticle or conjugation to a polymer, rather than a small chelating molecule.

Another important consideration is the effect of the osmotic pressures on cells in a suspension of a paramagnetic salt.[43] For reference, the osmotic pressure of a mammalian

cell is 300 milliosmoles (mOsm), while that of a 40 mM solution of Gd-DTPA in Dulbecco's Modified Eagle Medium (DMEM) is 278 mOsm.[91] As the concentration of ions in the surrounding medium increases, the cells lose water to reach equilibrium. To overcome toxicity risks and minimize osmotic pressure in cells to fabricate living tissue, a lower concentration of the paramagnetic salt should be used. However, this comes at the cost of decreasing $\Delta\chi$, necessitating the use of stronger magnetic field gradients to achieve similar levitations. The environmental impact of wastewater accumulation of Gd^{3+} is not yet fully known or understood.

2.7.3 Magnetic printing of cells

The formation of vasculature, hollow tube, and vessel-like structures is a critical challenge for tissue engineering and has been the focus of numerous bioprinting efforts.[161-165] These tubular structures are like those found in cardiovascular, respiratory, urinary, and gastrointestinal systems. Other challenges to the printing of cells relate to technical obstacles associated with handling samples and the limited number of assays optimized for 3D cellular structures. A widely used method is the CellTiter-Glo 3D bioluminescent assay which detects adenosine triphosphate (ATP).[2, 63] This kit lyses 3D cellular structures to quantify total cellular ATP. However, this quantification does not differentiate ATP obtained from cells in actively proliferative, quiescent, or senescent stages, which are often observed in the separate layers of 3D cellular structures.

Another approach to assess toxicity was used during magnetic 3D bioprinting of 3T3 spheroids by measuring the degree of spheroid contraction, since it is an indication of

cell health.[107] After exposure to five toxic compounds, the reduction in the projected areas of the spheroids was lower for larger concentrations of the paramagnetic compounds over a 150 minute incubation time. This dose-dependent response correlated with fluorescent staining of 3D spheroids that indicated cell arrangement and organization, and gene expression. A similar study used ring structures to imitate wound healing.[137] A microfluidic device was employed to characterize the growth of colorectal cancer cell lines formed into spheroids using mass, projected size (diameter) and mass density in response to anti-tumor natural killer (NK) cell-mediated infiltration and cytotoxicity. Here, a cell-line specific response was observed. This approach is a step towards standardization of 3D cell structure analysis.[166] Similar approaches using intermediary measures are helpful but may ultimately be unsatisfactory due to the complexity of 3D samples and pre-characterization requirements. The field will benefit from benchmark measures for 3D samples using reputable and widely used 2D assays for ease of use, such as mitochondrial analysis using the MTT assay, ATP measurements for assessing viability, and apoptosis and necrosis assays to assess cell death. Histology should also be used to observe tissue structure and distinguishing tissue markers of 3D-printed constructs, as compared to tissues *in vivo*. These methods, will require optimization to standardize evaluation of 3D-printed cellular constructs.

The ability to form complex *in vitro* 3D cellular co-cultures using magnetic cell bioinks is an important step towards the formation of engineered tissues and models of diseases.[55, 106] However, as multiple cell types are introduced into a single model, the selection of the culture medium is critically important.

The ultimate goal of tissue engineering is the production of complex human tissues and organs, and *in vitro* based models of human disease for clinical applications such as drug discovery and drug toxicity.[167] An *in vitro* model that is rapid, compatible with standard multi-well plate format, and cost-effective is desirable.[13]

2.7.4 Space exploration

The growing interest in space exploration and possible inhabitation of other planets has motivated microgravity research related to long-term spaceflight. By subjecting 3D cellular constructs to the forces experienced during space travel, it is possible to mimic the biological effects of weightlessness. [143] Of particular interest is the study of weightlessness on the musculoskeletal system and bone density, demonstrated through studies using bioreactor cultures of chondrocytes on polyglycolic acid scaffolds[168] and porcine articular cartilage chondrocytes[169] in space. These early investigations determined that prolonged weightlessness experienced in microgravity environments compromises the mechanical stiffness of the engineered cartilage-cell constructs. These effects were not observed in microgravity simulations and normal gravity (1g) experiments on earth.[169]

Using magnetic levitation and printing of a 3D tissue construct in space,[170] the focus of recent studies has been to understand the short- and long-term effects of weightlessness.[90] Studies have also been conducted to understand the effects on cell cycle and cell viability in a paramagnetic medium suspension.[171] Such studies are rare since they are expensive, time-consuming, require the cooperation of national and international space agencies, and training of astronauts to handle biological specimens.

2.7.5 Translational outlook

Development of 3D cell culturing and *in vitro* testing is driven by animal welfare and a shift towards plant-based alternatives to meat and polymers. Recent advances in 3D bioprinting offer solutions to these concerns with the development of lab-grown meat[172] and use of plant-derived materials for tissue engineering,[173, 174] hemp for microfluidic paper-based analytic devices,[175] and biodegradable patches.[176]

The potential of magnetic bioinks and 3D bioprinting to assist patient-specific diagnosis and treatment is becoming a reality. Recent advances include the formation of spheroids composed of neonatal primary rat cardiomyocytes,[177] primary human hepatocytes formed into spheroids to study cytochrome P450 (CYP450) activity,[178] and primary human myometrial smooth muscle cells formed into rings[128] using magnetic labels. In the study for uterine contractility, three patient-derived cell sources from biopsy during cesarean section displayed different responses to tocolytic drugs, indomethacin and nifedipine.[128] These differences validate the importance of patient-specific diagnosis towards efforts of personalized medicine.

In addition to academic institutions, clinical research organizations (Crown Bioscience Inc., Aurelia Biosciences) have adopted 3D cell culture testing methods. However, widespread adoption within the industry is limited due to challenges posed by systematic assessments of 3D cultures to optimize comparability to *in vivo* tissue, lack of standardization of assay protocols, limitations of imaging systems, and acceptance of the 3D cell culture data by regulatory agencies.

Despite these challenges, the future of 3D cell culture is evident by the multitude of suppliers that provide reagents, cells, assays, equipment, and consumables for 3D cell culture. Bioinstrumentation companies (Luminex Corporations, Curiox Biosystems) offer magnetic bead-based immunoassay platforms and suppliers of magnetic beads used for cell manipulation and producing 3D structures (Thermofisher, N3D Biosciences, Luna Nanotech, Creative Diagnostics, Bioclone Inc., and Sigma Aldrich). N3D Biosciences offers a magnetic 3D bioprinting technology that uses magnetic beads to label cells (NanoShuttles^{TM}) and forms 3D constructs using a magnetic assembler. Levitas Bio employs label-free magnetic manipulation to enrich and purify cells. The global 3D bioprinting market was valued at 1.4B USD in 2020 and is expected to expand with a compound annual growth rate (CAGR) of 15.8%.[179] Although magnetic bioink-based bioprinting is a fraction of this market size, because it improves control, speed, and accuracy, it is expected to expand with a CAGR of 17%. As the bioprinting industry grows, there is a need to organize and accumulate databases and build digital twins of physical experimental data.[180]

2.8 Conclusions

A *magnetic bioink* is a binary solution containing any combination of magnetic agents (e.g. MNPs, paramagnetic salts) and biological components (e.g. cells, proteins, biological fluids), which can be used for *in vitro* and *in vivo* applications. We describe how 3D magnetic bioprinting with these bioinks is used in scaffold-free and scaffold-based *in situ* technology. The term *magnetic levitation* is used to describe both positive[106] and negative[90, 139] magnetophorses. In both cases, magnetic susceptibility differences between the levitated

object and the medium in which is it is levitated allow a magnetic force to overcome the force of gravity.

The versatility of magnetic bioinks allows their use in many applications, including cell separation, *in vitro* modeling, *in vivo* therapies such as MFH and MDT, and biosensing. The ability to be manipulated by action-from-a distance and high control over their movement make magnetic bioinks suitable for enhancing biomedical innovation, reinventing traditional approaches. As the development of physiologically relevant *in vitro* models improves, 3D cellular structures printed with magnetic bioinks containing cells will be able to improve drug discovery by accelerating meaningful experiments, improve existing technologies, and transform the treatment of disease.

2.9 Acknowledgements

Author contributions: S. Mishriki is the lead author of the manuscript, and prepared the figures and table with guidance from I. K. Puri and R. P. Sahu. T. Gupta lead the section on *Magnetophoresis Fundamentals* with contributions from S. Mishriki and assistance from R. P. Sahu and I. K. Puri. R. P. Sahu led the section on *Translational Outlook* with contributions from S. Mishriki. I. K. Puri is the corresponding author. All authors contributed to initial drafts and the final version of the manuscript by reviewing and editing it before submission.

Competing interests: All authors declare that there are no competing conflicts of interest.

2.10 References

1. H. Jaganathan, J. Gage, F. Leonard, S. Srinivasan, G. R. Souza, B. Dave and B. Godin, *Scientific reports*, 2014, **4**, 6468.

2. V. A. Parfenov, E. V. Koudan, A. A. Krokhmal, E. A. Annenkova, S. V. Petrov, F. D. Pereira, P. A. Karalkin, E. K. Nezhurina, A. A. Gryadunova and E. A. Bulanova, *Advanced Healthcare Materials*, 2020, 2000721.

3. N. Charbe, P. A. McCarron and M. M. Tambuwala, *World journal of clinical oncology*, 2017, **8**, 21.

4. V. Brancato, J. M. Oliveira, V. M. Correlo, R. L. Reis and S. C. Kundu, *Biomaterials*, 2020, **232**, 119744.

5. J. Kang, D. W. Lee, H. J. Hwang, S.-E. Yeon, M.-Y. Lee and H.-J. Kuh, *Lab on a Chip*, 2016, **16**, 2265-2276.

6. M. Cooper, M. Tanaka and I. Puri, *Cell Proliferation*, 2010, **43**, 542-552.

7. R. Ganguly and I. Puri, *Cell proliferation*, 2007, **40**, 338-354.

8. P. A. Kenny, G. Y. Lee, C. A. Myers, R. M. Neve, J. R. Semeiks, P. T. Spellman, K. Lorenz, E. H. Lee, M. H. Barcellos-Hoff and O. W. Petersen, *Molecular oncology*, 2007, **1**, 84-96.

9. S. Ghosh, S. Kumar, I. Puri and S. Elankumaran, *Cell proliferation*, 2016, **49**, 134-144.

10. H. Tseng, J. A. Gage, R. M. Raphael, R. H. Moore, T. C. Killian, K. J. Grande-Allen and G. R. Souza, *Tissue Engineering Part C: Methods*, 2013, **19**, 665-675.

11. E. C. Costa, A. F. Moreira, D. de Melo-Diogo, V. M. Gaspar, M. P. Carvalho and I. J. Correia, *Biotechnology advances*, 2016, **34**, 1427-1441.

12. L. A. Kunz-Schughart, J. P. Freyer, F. Hofstaedter and R. Ebner, *Journal of biomolecular screening*, 2004, **9**, 273-285.

13. X. Xin, H. Yang, F. Zhang and S.-T. Yang, *Process biochemistry*, 2019, **78**, 148-160.

14. M. Zanoni, F. Piccinini, C. Arienti, A. Zamagni, S. Santi, R. Polico, A. Bevilacqua and A. Tesei, *Scientific reports*, 2016, **6**, 19103.

15. H. Clevers, *Cell*, 2016, **165**, 1586-1597.

16. F. Schutgens and H. Clevers, *Annual Review of Pathology: Mechanisms of Disease*, 2020, **15**, 211-234.

17. F. Soto, C. F. Guimarães, R. L. Reis, W. Franco, I. Rizvi and U. Demirci, *Cancer Letters*, 2021, **504**, 116-124.

18. N. S. Bhise, V. Manoharan, S. Massa, A. Tamayol, M. Ghaderi, M. Miscuglio, Q. Lang, Y. S. Zhang, S. R. Shin and G. Calzone, *Biofabrication*, 2016, **8**, 014101.

19. A. Essaouiba, R. Jellali, M. Shinohara, B. Scheidecker, C. Legallais, Y. Sakai and E. Leclerc, *Journal of Biotechnology*, 2021, **330**, 45-56.

20. H.-F. Tsai, A. Trubelja, A. Q. Shen and G. Bao, *Journal of The Royal Society Interface*, 2017, **14**, 20170137.

21. M. Ustun, S. Rahmani Dabbagh, I. S. Ilci, T. Bagci-Onder and S. Tasoglu, *Micromachines*, 2021, **12**, 490.

22. E. M. Langer, B. L. Allen-Petersen, S. M. King, N. D. Kendsersky, M. A. Turnidge, G. M. Kuziel, R. Riggers, R. Samatham, T. S. Amery and S. L. Jacques, *Cell reports*, 2019, **26**, 608-623. e606.

23. A. E. Jakus, A. L. Rutz, S. W. Jordan, A. Kannan, S. M. Mitchell, C. Yun, K. D. Koube, S. C. Yoo, H. E. Whiteley and C.-P. Richter, *Science translational medicine*, 2016, **8**, 358ra127-358ra127.

24. S. V. Murphy and A. Atala, *Nature biotechnology*, 2014, **32**, 773.

25. J. Arenas-Herrera, I. Ko, A. Atala and J. Yoo, *Biomedical materials*, 2013, **8**, 014106.

26. H.-W. Kang, S. J. Lee, I. K. Ko, C. Kengla, J. J. Yoo and A. Atala, *Nature biotechnology*, 2016, **34**, 312-319.

27. D. Madhuri and I. T. Ozbolat, *Scientific Reports (Nature Publisher Group)*, 2020, **10**.

28. J. M. Lee, S. L. Sing, M. Zhou and W. Y. Yeong, *International Journal of Bioprinting*, 2018, **4**.

29. A. Atala, S. B. Bauer, S. Soker, J. J. Yoo and A. B. Retik, *The lancet*, 2006, **367**, 1241-1246.

30. P. Macchiarini, P. Jungebluth, T. Go, M. A. Asnaghi, L. E. Rees, T. A. Cogan, A. Dodson, J. Martorell, S. Bellini and P. P. Parnigotto, *The Lancet*, 2008, **372**, 2023-2030.

31. M. J. Elliott, P. De Coppi, S. Speggiorin, D. Roebuck, C. R. Butler, E. Samuel, C. Crowley, C. McLaren, A. Fierens and D. Vondrys, *The Lancet*, 2012, **380**, 994-1000.

32. Z. Wan, P. Zhang, Y. Liu, L. Lv and Y. Zhou, *Acta biomaterialia*, 2020, **101**, 26-42.

33. B. Gao, Q. Yang, X. Zhao, G. Jin, Y. Ma and F. Xu, *Trends in biotechnology*, 2016, **34**, 746-756.

34. T. Gupta, R. Ghosh and R. Ganguly, *International journal for numerical methods in biomedical engineering*, 2018, **34**, e2943.

35. B. Kang, J. Shin, H.-J. Park, C. Rhyou, D. Kang, S.-J. Lee, Y.-s. Yoon, S.-W. Cho and H. Lee, *Nature communications*, 2018, **9**, 1-13.

36. R. Fan, M. Piou, E. Darling, D. Cormier, J. Sun and J. Wan, *Journal of biomaterials applications*, 2016, **31**, 684-692.

37. H. Huang, X. Qi, Y. Chen and Z. Wu, *Saudi Pharmaceutical Journal*, 2019, **27**, 990-999.

38. S. Knowlton, B. Yenilmez, S. Anand and S. Tasoglu, *Bioprinting*, 2017, **5**, 10-18.

39. E. M. Benetti, M. K. Gunnewiek, C. A. van Blitterswijk, G. J. Vancso and L. Moroni, *Journal of Materials Chemistry B*, 2016, **4**, 4244-4257.

40. A. Shahin-Shamsabadi and P. Selvaganapathy, *Materials Today Bio*, 2020, **7**, 100070.

41. E. Turker and A. Arslan-Yildiz, *ACS Biomaterials Science & Engineering*, 2018, **4**, 787-799.

42. Q.-H. Gao, W.-M. Zhang, H.-X. Zou, W.-B. Li, H. Yan, Z.-K. Peng and G. Meng, *Materials Horizons*, 2019.

43. S. Tasoglu, C. H. Yu, V. Liaudanskaya, S. Guven, C. Migliaresi and U. Demirci, *Advanced healthcare materials*, 2015, **4**, 1469-1476.

44. E. Türker, N. Demirçak and A. Arslan-Yildiz, *Biomaterials Science*, 2018.

45. N. Ashammakhi, S. Ahadian, F. Zengjie, K. Suthiwanich, F. Lorestani, G. Orive, S. Ostrovidov and A. Khademhosseini, *Biotechnology journal*, 2018, **13**, 1800148.

46. F. Ozefe and A. A. Yildiz, in *Magnetic Levitation*, IntechOpen, 2020.

47. J. Adhikari, A. Roy, A. Das, M. Ghosh, S. Thomas, A. Sinha, J. Kim and P. Saha, *Macromolecular Bioscience*, 2021, **21**, 2000179.

48. V. A. Parfenov, S. V. Petrov, F. D. Pereira, A. A. Levin, E. V. Koudan, E. K. Nezhurina, P. A. Karalkin, M. M. Vasiliev, O. F. Petrov and V. S. Komlev, *International Journal of Bioprinting*, 2020, **6**.

49. C. Zhang, P. Zhao, F. Gu, X. Zhang, J. Xie, Y. He, H. Zhou, J. Fu and L.-S. Turng, *Analytical Chemistry*, 2020.

50. S. Yaman, M. Anil-Inevi, E. Ozcivici and H. C. Tekin, *Frontiers in bioengineering and biotechnology*, 2018, **6**, 192.

51. M. Latorre and C. Rinaldi, *Puerto Rico health sciences journal*, 2009, **28**.

52. J.-B. Fan, C. Huang, L. Jiang and S. Wang, *Journal of Materials Chemistry B*, 2013, **1**, 2222-2235.

53. R. Ganguly and I. K. Puri, *Wiley Interdisciplinary Reviews: Nanomedicine and Nanobiotechnology*, 2010, **2**, 382-399.

54. M. Okochi, T. Matsumura and H. Honda, *Biosensors and Bioelectronics*, 2013, **42**, 300-307.

55. T. Gupta, S. Aithal, S. Mishriki, R. P. Sahu, F. Geng and I. K. Puri, *ACS Biomaterials Science & Engineering*, 2020.

56. S. Tasoglu, D. Kavaz, U. A. Gurkan, S. Guven, P. Chen, R. Zheng and U. Demirci, *Advanced Materials*, 2013, **25**, 1137-1143.

57. K. A. Mirica, F. Ilievski, A. K. Ellerbee, S. S. Shevkoplyas and G. M. Whitesides, *Advanced Materials*, 2011, **23**, 4134-4140.

58. W. L. Haisler, D. M. Timm, J. A. Gage, H. Tseng, T. Killian and G. R. Souza, *Nature protocols*, 2013, **8**, 1940-1949.

59. V. Zavisova, M. Koneracka, A. Gabelova, B. Svitkova, M. Ursinyova, M. Kubovcikova, I. Antal, I. Khmara, A. Jurikova and M. Molcan, *Journal of Magnetism and Magnetic Materials*, 2019, **472**, 66-73.

60. H. Tseng, J. A. Gage, W. L. Haisler, S. K. Neeley, T. Shen, C. Hebel, H. G. Barthlow, M. Wagoner and G. R. Souza, *Scientific reports*, 2016, **6**, 30640.

61. B. Mattix, T. R. Olsen, Y. Gu, M. Casco, A. Herbst, D. T. Simionescu, R. P. Visconti, K. G. Kornev and F. Alexis, *Acta biomaterialia*, 2014, **10**, 623-629.

62. A. R. Abdel Fattah, E. Meleca, S. Mishriki, A. Lelic, F. Geng, R. P. Sahu, S. Ghosh and I. K. Puri, *ACS Biomaterials Science & Engineering*, 2016.

63. S. Mishriki, S. Aithal, T. Gupta, R. P. Sahu, F. Geng and I. K. Puri, *Research*, 2020, **2020**.

64. S. Mishriki, A. A. Fattah, T. Kammann, R. Sahu, F. Geng and I. Puri, *Research*, 2019, **2019**, 9854593.

65. A. R. A. Fattah, S. Mishriki, T. Kammann, R. P. Sahu, F. Geng and I. K. Puri, *Biomaterials science*, 2018, **6**, 683-694.

66. M. Anil-Inevi, K. Delikoyun, G. Mese, H. C. Tekin and E. Ozcivici, *bioRxiv*, 2021.

67. N. G. Durmus, H. C. Tekin, S. Guven, K. Sridhar, A. A. Yildiz, G. Calibasi, I. Ghiran, R. W. Davis, L. M. Steinmetz and U. Demirci, *Proceedings of the National Academy of Sciences*, 2015, **112**, E3661-E3668.

68. K. Delikoyun, A. A. Demir and H. C. Tekin, 2021.

69. N. Puluca, N. G. Durmus, S. Lee, N. Belbachir, F. X. Galdos, M. G. Ogut, R. Gupta, K. i. Hirano, M. Krane and R. Lange, *Advanced biosystems*, 2020, **4**, 1900300.

70. K. Delikoyun, S. Yaman, E. Yilmaz, O. Sarigil, M. Anil-Inevi, E. Ozcivici and H. C. Tekin, *bioRxiv*, 2020.

71. A. R. A. Fattah, S. Mishriki, T. Kammann, R. P. Sahu, F. Geng and I. K. Puri, *BioMetals*, 2018, 1-12.

72. C. Zhang, P. Zhao, F. Gu, J. Xie, N. Xia, Y. He and J. Fu, *Analytical chemistry*, 2018, **90**, 9226-9233.

73. M. V. Berry and A. K. Geim, *European Journal of Physics*, 1997, **18**, 307.

74. M. Zborowski, L. Sun, L. R. Moore, P. S. Williams and J. J. Chalmers, *Journal of Magnetism and Magnetic Materials*, 1999, **194**, 224-230.

75. T. Zhu, F. Marrero and L. Mao, 2010.

76. S. A. Peyman, E. Y. Kwan, O. Margarson, A. Iles and N. Pamme, *Journal of Chromatography A*, 2009, **1216**, 9055-9062.

77. P. Cherukuri, E. S. Glazer and S. A. Curley, *Advanced drug delivery reviews*, 2010, **62**, 339-345.

78. D. Sardari and N. Verga, *Cancer treatment with hyperthermia*, Citeseer, 2011.

79. R. Kappiyoor, M. Liangruksa, R. Ganguly and I. K. Puri, *Journal of Applied Physics*, 2010, **108**, 094702.

80. S. Yaman and H. C. Tekin, *Analytical Chemistry*, 2020.

81. A. R. Abdel Fattah, A. M. Abdalla, S. Mishriki, E. Meleca, F. Geng, S. Ghosh and I. K. Puri, *ACS Applied Materials & Interfaces*, 2017.

82. M. Mahmoudi, *Molecular Pharmaceutics*, 2020.

83. K. Leirs, P. Tewari Kumar, D. Decrop, E. Pérez-Ruiz, P. Leblebici, B. Van Kelst, G. Compernolle, H. Meeuws, L. Van Wesenbeeck and O. Lagatie, *Analytical chemistry*, 2016, **88**, 8450-8458.

84. D. J. Griffiths, *Journal*, 2005.

85. D. T. Grob, N. Wise, O. Oduwole and S. Sheard, *Journal of Magnetism and Magnetic Materials*, 2018, **452**, 134-140.

86. V. Iacovacci, G. Lucarini, L. Ricotti and A. Menciassi, *Lab-On-A-Chip Fabrication and Application*, 2016, **40**.

87. J. A. Patton, *Radiographics*, 1994, **14**, 1083-1096.

88. D. Ghosh, T. Gupta, R. P. Sahu, P. K. Das and I. K. Puri, *Physics of Fluids*, 2020, **32**, 072001.

89. M. Sepioni, R. Nair, S. Rablen, J. Narayanan, F. Tuna, R. Winpenny, A. Geim and I. Grigorieva, *Physical review letters*, 2010, **105**, 207205.

90. M. Anil-Inevi, S. Yaman, A. A. Yildiz, G. Mese, O. Yalcin-Ozuysal, H. C. Tekin and E. Ozcivici, *Scientific reports*, 2018, **8**, 7239.

91. A. Winkleman, K. L. Gudiksen, D. Ryan, G. M. Whitesides, D. Greenfield and M. Prentiss, *Applied physics letters*, 2004, **85**, 2411-2413.

92. M. Frenea-Robin, H. Chetouani, N. Haddour, H. Rostaing, J. Laforet and G. Reyne, 2008.

93. R. Ganguly, A. P. Gaind, S. Sen and I. K. Puri, *Journal of Magnetism and Magnetic Materials*, 2005, **289**, 331-334.

94. J. W. Park, N. R. Lee, S. M. Cho, M. Y. Jung, C. Ihm and D. S. Lee, *Etri Journal*, 2015, **37**, 233-240.

95. R. Ganguly and I. K. Puri, *Advances in applied mechanics*, 2007, **41**, 293-335.

96. M. Zahn, 1979.

97. K. Smistrup, O. Hansen, H. Bruus and M. F. Hansen, *Journal of magnetism and magnetic materials*, 2005, **293**, 597-604.

98. O. Sarigil, M. Anil-Inevi, B. Firatligil-Yildirir, Y. C. Unal, O. Yalcin-Ozuysal, G. Mese, H. C. Tekin and E. Ozcivici, *Biotechnology and bioengineering*, 2021, **118**, 1127-1140.

99. V. Mironov, R. P. Visconti, V. Kasyanov, G. Forgacs, C. J. Drake and R. R. Markwald, *Biomaterials*, 2009, **30**, 2164-2174.

100. M. W. Laschke and M. D. Menger, *Trends in biotechnology*, 2017, **35**, 133-144.

101. S. B. Ozler, C. Kucukgul and B. Koc, in *Bioprinting in Regenerative Medicine*, Springer, 2015, pp. 67-88.

102. M. E. Prendergast, R. D. Solorzano and D. Cabrera, *Journal of 3D printing in medicine*, 2017, **1**, 49-62.

103. S. Nath and G. R. Devi, *Pharmacology & therapeutics*, 2016, **163**, 94-108.

104. V. A. Parfenov, V. A. Mironov, K. A. van Kampen, P. A. Karalkin, E. V. Koudan, F. D. Pereira, S. V. Petrov, E. K. Nezhurina, O. F. Petrov and M. Myasnikov, *Biofabrication*, 2020.

105. V. A. Parfenov, E. V. Koudan, E. A. Bulanova, P. A. Karalkin, F. D. Pereira, N. E. Norkin, A. D. Knyazeva, A. A. Gryadunova, O. F. Petrov and M. M. Vasiliev, *Biofabrication*, 2018, **10**, 034104.

106. H. Tseng, L. R. Balaoing, B. Grigoryan, R. M. Raphael, T. Killian, G. R. Souza and K. J. Grande-Allen, *Acta biomaterialia*, 2014, **10**, 173-182.

107. H. Tseng, J. A. Gage, T. Shen, W. L. Haisler, S. K. Neeley, S. Shiao, J. Chen, P. K. Desai, A. Liao and C. Hebel, *Scientific reports*, 2015, **5**, 13987.

108. A. R. Abdel Fattah, T. Majdi, A. M. Abdalla, S. Ghosh and I. K. Puri, *ACS applied materials & interfaces*, 2016, **8**, 1589-1593.

109. A. R. A. Fattah, S. Ghosh and I. K. Puri, *Journal of Magnetism and Magnetic Materials*, 2016, **401**, 1054-1059.

110. A. R. Abdel Fattah, S. Ghosh and I. K. Puri, *ACS Applied Materials & Interfaces*, 2016, **8**, 11018-11023.

111. R. Gilchrist, R. Medal, W. D. Shorey, R. C. Hanselman, J. C. Parrott and C. B. Taylor, *Annals of surgery*, 1957, **146**, 596.

112. A. Schröfel, G. Kratošová, I. Šafařík, M. Šafaříková, I. Raška and L. M. Shor, *Acta biomaterialia*, 2014, **10**, 4023-4042.

113. T. I. Shabatina, O. I. Vernaya, V. P. Shabatin and M. Y. Melnikov, *Magnetochemistry*, 2020, **6**, 30.

114. A. R. Abdel Fattah and A. Ranga, *Frontiers in bioengineering and biotechnology*, 2020, **8**, 240.

115. Y. Wang, Y. Li, R. Wang, M. Wang and J. Lin, *Journal of separation science*, 2017, **40**, 1540-1547.

116. V. Goranov, T. Shelyakova, R. De Santis, Y. Haranava, A. Makhaniok, A. Gloria, A. Tampieri, A. Russo, E. Kon and M. Marcacci, *Scientific reports*, 2020, **10**, 1-8.

117. L. Zwi-Dantsis, B. Wang, C. Marijon, S. Zonetti, A. Ferrini, L. Massi, D. J. Stuckey, C. M. Terracciano and M. M. Stevens, *Advanced Materials*, 2020, **32**, 1904598.

118. E. A. Tarim, B. Karakuzu, C. Oksuz, O. Sarigil, M. Kizilkaya, M. K. A. Al-Ruweidi, H. C. Yalcin, E. Ozcivici and H. C. Tekin, *Emergent Materials*, 2021, 1-26.

119. N. Pamme, *Current opinion in chemical biology*, 2012, **16**, 436-443.

120. H.-C. Lai, C.-H. Wang, T.-M. Liou and G.-B. Lee, *Lab on a Chip*, 2014, **14**, 2002-2013.

121. C. Coarsey, B. Coleman, M. A. Kabir, M. Sher and W. Asghar, *RSC advances*, 2019, **9**, 8159-8168.

122. L. Fabiani, M. Saroglia, G. Galatà, R. De Santis, S. Fillo, V. Luca, G. Faggioni, N. D'Amore, E. Regalbuto and P. Salvatori, *Biosensors and Bioelectronics*, 2021, **171**, 112686.

123. J. M. Luk and A. A. Lindberg, *Journal of immunological methods*, 1991, **137**, 1-8.

124. M. Varshney and Y. Li, *Biosensors and Bioelectronics*, 2007, **22**, 2408-2414.

125. B. D. Plouffe, S. K. Murthy and L. H. Lewis, *Reports on Progress in Physics*, 2014, **78**, 016601.

126. K. Nandy, S. Chaudhuri, R. Ganguly and I. K. Puri, *Journal of Magnetism and Magnetic Materials*, 2008, **320**, 1398-1405.

127. A. C. Daquinag, G. R. Souza and M. G. Kolonin, *Tissue Engineering Part C: Methods*, 2013, **19**, 336-344.

128. G. R. Souza, H. Tseng, J. A. Gage, A. Mani, P. Desai, F. Leonard, A. Liao, M. Longo, J. S. Refuerzo and B. Godin, *International journal of molecular sciences*, 2017, **18**, 683.

129. L. G. Sabino, P. F. Menezes, V. S. Bagnato, G. Souza, T. C. Killian and C. Kurachi, 2014.

130. E. Kaemmerer, T. E. R. Garzon, A. M. Lock, C. J. Lovitt and V. M. Avery, *Drug Discovery Today: Disease Models*, 2016, **21**, 11-16.

131. K. E. Sung, X. Su, E. Berthier, C. Pehlke, A. Friedl and D. J. Beebe, *PloS one*, 2013, **8**.

132. S. C. Wei and J. Yang, *Trends in cell biology*, 2016, **26**, 111-120.

133. W. Chen, S. Park, C. Patel, Y. Bai, K. Henary, A. Raha, S. Mohammadi, L. You and F. Geng, *Heliyon*, 2021, **7**, e06252.

134. G. R. Souza, J. R. Molina, R. M. Raphael, M. G. Ozawa, D. J. Stark, C. S. Levin, L. F. Bronk, J. S. Ananta, J. Mandelin and M.-M. Georgescu, *Nature nanotechnology*, 2010, **5**, 291-296.

135. L. A. A. Neto, T. M. Pereira and L. P. Silva, *Materials Science and Engineering: C*, 2020, **116**, 111267.

136. S. Varchetta, D. Mele, B. Oliviero, S. Mantovani, S. Ludovisi, A. Cerino, R. Bruno, A. Castelli, M. Mosconi and M. Vecchia, *Cellular & molecular immunology*, 2021, **18**, 604-612.

137. D. M. Timm, J. Chen, D. Sing, J. A. Gage, W. L. Haisler, S. K. Neeley, R. M. Raphael, M. Dehghani, K. P. Rosenblatt and T. Killian, *Scientific reports*, 2013, **3**, 3000.

138. A. R. A. Fattah, S. Ghosh and I. K. Puri, *Journal of Chromatography B*, 2016, **1027**, 194-199.

139. A. B. Subramaniam, D. Yang, H.-D. Yu, A. Nemiroski, S. Tricard, A. K. Ellerbee, S. Soh and G. M. Whitesides, *Proceedings of the National Academy of Sciences*, 2014, **111**, 12980-12985.

140. A. Tocchio, N. G. Durmus, K. Sridhar, V. Mani, B. Coskun, R. El Assal and U. Demirci, *Advanced Materials*, 2018, **30**, 1705034.

141. F. Shen, H. Hwang, Y. K. Hahn and J.-K. Park, *Analytical chemistry*, 2012, **84**, 3075-3081.

142. P. Kauffmann, N. Dempsey, D. O'Brien, S. Combe, B. Schaack, V. Haguet and G. Reyne, 2010.

143. C. E. Dijkstra, O. J. Larkin, P. Anthony, M. R. Davey, L. Eaves, C. E. Rees and R. J. Hill, *Journal of the Royal Society Interface*, 2011, **8**, 334-344.

144. M. D. Krebs, R. M. Erb, B. B. Yellen, B. Samanta, A. Bajaj, V. M. Rotello and E. Alsberg, *Nano letters*, 2009, **9**, 1812-1817.

145. Y. Akiyama and K. Morishima, 2012.

146. R. Onbas and A. Arslan Yildiz, *ACS Applied Bio Materials*, 2021, **4**, 1794-1802.

147. O. Sarigil, M. Anil-Inevi, E. Yilmaz, O. Ozcelik, G. Mese, H. C. Tekin and E. Ozcivici, 2020.

148. S. Guven, P. Chen, F. Inci, S. Tasoglu, B. Erkmen and U. Demirci, *Trends in biotechnology*, 2015, **33**, 269-279.

149. H. M. Zlotnick, A. T. Clark, S. E. Gullbrand, J. L. Carey, X. M. Cheng and R. L. Mauck, *Advanced Materials*, 2020, **32**, 2005030.

150. C. S. Kumar and F. Mohammad, *Advanced drug delivery reviews*, 2011, **63**, 789-808.

151. B. Hu, F. Dai, Z. Fan, G. Ma, Q. Tang and X. Zhang, *Advanced Materials*, 2015, **27**, 5499-5505.

152. E. F. Bernstein, H. W. Sarkas and P. Boland, *Journal of Cosmetic Dermatology*, 2020.

153. A. B. Lyons, C. Trullas, I. Kohli, I. H. Hamzavi and H. W. Lim, *Journal of the American Academy of Dermatology*, 2021, **84**, 1393-1397.

154. S. Laurent, S. Dutz, U. O. Häfeli and M. Mahmoudi, *Advances in colloid and interface science*, 2011, **166**, 8-23.

155. S. Shaw, P. Sibanda and P. Murthy, 2013.

156. V. V. Chrishtop, V. A. Mironov, A. Y. Prilepskii, V. G. Nikonorova and V. V. Vinogradov, *Nanotoxicology*, 2020, 1-38.

157. A. Paolini, C. P. Guarch, D. Ramos-López, J. de Lapuente, A. Lascialfari, Y. Guari, J. Larionova, J. Long and R. Nano, *Journal of Applied Toxicology*, 2016, **36**, 510-520.

158. M. Rogosnitzky and S. Branch, *Biometals*, 2016, **29**, 365-376.

159. J. Ramalho, M. Ramalho, M. Jay, L. M. Burke and R. C. Semelka, *Magnetic resonance imaging*, 2016, **34**, 1394-1398.

160. L. Pasquini, A. Napolitano, E. Visconti, D. Longo, A. Romano, P. Tomà and M. C. R. Espagnet, *CNS drugs*, 2018, **32**, 229-240.

161. D. Richards, J. Jia, M. Yost, R. Markwald and Y. Mei, *Annals of biomedical engineering*, 2017, **45**, 132-147.

162. D. B. Kolesky, K. A. Homan, M. A. Skylar-Scott and J. A. Lewis, *Proceedings of the national academy of sciences*, 2016, **113**, 3179-3184.

163. S. Ravi and E. L. Chaikof, *Regenerative medicine*, 2010, **5**, 107-120.

164. R. Attalla, E. Puersten, N. Jain and P. R. Selvaganapathy, *Biofabrication*, 2018, **11**, 015012.

165. L. A. Kunz-Schughart, J. A. Schroeder, M. Wondrak, F. van Rey, K. Lehle, F. Hofstaedter and D. N. Wheatley, *American Journal of Physiology-Cell Physiology*, 2006, **290**, C1385-C1398.

166. A. Sargenti, F. Musmeci, F. Bacchi, C. Delprete, D. A. Cristaldi, F. Cannas, S. Bonetti, S. Pasqua, D. Gazzola and D. Costa, *Frontiers in immunology*, 2020, **11**, 3293.

167. V. Mironov, V. Kasyanov, C. Drake and R. R. Markwald, 2008.

168. L. E. Freed, R. Langer, I. Martin, N. R. Pellis and G. Vunjak-Novakovic, *Proceedings of the National Academy of Sciences*, 1997, **94**, 13885-13890.

169. V. Stamenković, G. Keller, D. Nesic, A. Cogoli and S. P. Grogan, *Tissue Engineering Part A*, 2010, **16**, 1729-1736.

170. V. A. Parfenov, Y. D. Khesuani, S. V. Petrov, P. A. Karalkin, E. V. Koudan, E. K. Nezhurina, F. D. Pereira, A. A. Krokhmal, A. A. Gryadunova and E. A. Bulanova, *Science advances*, 2020, **6**, eaba4174.

171. M. Anil-Inevi, Y. C. Unal, S. Yaman, H. C. Tekin, G. Mese and E. Ozcivici, 2020.

172. A. Shahin-Shamsabadi and P. R. Selvaganapathy, *Cells Tissues Organs*, 1-9.

173. A. C. Bilirgen, M. Toker, S. Odabas, A. K. Yetisen, B. Garipcan and S. Tasoglu, *ACS Biomaterials Science & Engineering*, 2021, **7**, 926-938.

174. M. Guzelgulgen, D. Ozkendir-Inanc, U. H. Yildiz and A. Arslan-Yildiz, *International Journal of Biological Macromolecules*, 2021, **180**, 729-738.

175. M. Temirel, S. R. Dabbagh and S. Tasoglu, *Micromachines*, 2021, **12**, 182.

176. M. Temirel, C. Hawxhurst and S. Tasoglu, *Micromachines*, 2021, **12**, 195.

177. M. Hogan, G. Souza and R. Birla, *AIMS Bioeng*, 2016, **3**, 277-288.

178. P. K. Desai, H. Tseng and G. R. Souza, *International journal of molecular sciences*, 2017, **18**, 1085.

179. *Global 3D Bioprinting Market Size & Trends Report 2021-2028*, 2021.

180. J. An, C. K. Chua and V. Mironov, *International Journal of Bioprinting*, 2021, **7**.

3 In Situ 3D Label-Free Contactless Bioprinting of Cells Through Diamagnetophoresis

This chapter is reproduced from *In situ label-free contactless bioprinting of cells through diamagnetophoresis, 2(12), 2133-2138, 2016, ACS Biomaterials Science & Engineering, Abdel Fattah Abdel Rahman, Elvira Meleca,* ***Sarah Mishriki****, Alina Lelic, Fei Geng, Rakesh P. Sahu, Suvojit Ghosh, and Ishwar K. Puri, https://doi.org/10.1021/acsbiomaterials.6b00614*. The author of this thesis co-authored this publication with A.R. Abdel Fattah and E. Meleca, who each contributed equally to the work. S. Mishriki proposed the idea of placing magnets beneath the vessel, resulting in the formation of spheroids, determined viability of whole blood, and contributed to writing of the manuscript.

3.1 Abstract

Using whole blood, we demonstrate the first realization of a novel macroscale, contactless, label-free method to print *in situ* three-dimensional (3D) cell assemblies of different morphologies and sizes. This novel bioprinting method does not use nozzles that can contaminate the cell suspension, or to which cells can adhere. Instead, we utilize the intrinsic diamagnetic properties of whole blood cells to magnetically manipulate them *in situ* in a nontoxic paramagnetic medium, creating (a) rectangular bar, (b) three-pointed star, and (c) spheroids of varying sizes. We envision the technique to be transferable to other cell lines, with potential applications in tissue engineering and drug screening.

3.2 Introduction

Separation, concentration and overall manipulation of cells has been of significant interest in cell biological assays and medical diagnostics. Specifically, manipulation of cells into three-dimensional (3D) cultures have gained attention due such cell assemblies to better mimic physiological conditions compared cultured cell monolayers. Printing 3D cell assemblies and patterns can further simplify tissue engineering, cell-on-chip devices and drug screening applications.[1-2]

3.3 Experimental results

We magnetically manipulate cells by utilizing their intrinsic magnetic properties to print *in situ* 3D cell assemblies through a contactless method. A paramagnetic buffer is mixed into a solid-fluid suspension, leading to a difference between the magnetic susceptibilities of the solid and its surrounding medium, which induces differential magnetic forces on the mixture constituents.[3-5] When an external magnetic field is applied on such a cell-medium system, a cell behaves as a diamagnetic material that migrates towards region of lower magnetic field strength. For instance, the susceptibility contrast between the hemoglobin present in the oxygenated and deoxygenated states of red blood cells (RBCs) and its carrying medium can be exploited for label and label-free cell separation.[6-22] However, previous applications of diamagnetophoresis to manipulate and pattern cells have employed high gradient magnetic field microstructures,[23-25] which restrict the method to micron size cell assemblies that rely on an externally generated fluid flow to transport cells from high to low magnetic field strength regions. Instead, using non-

adherent whole blood, we present the first realization of a novel macroscale method to print *in situ* cell assemblies of different sizes and morphologies without introducing external flows or surfaces. A schematic is provided in **Figure 3.1**.

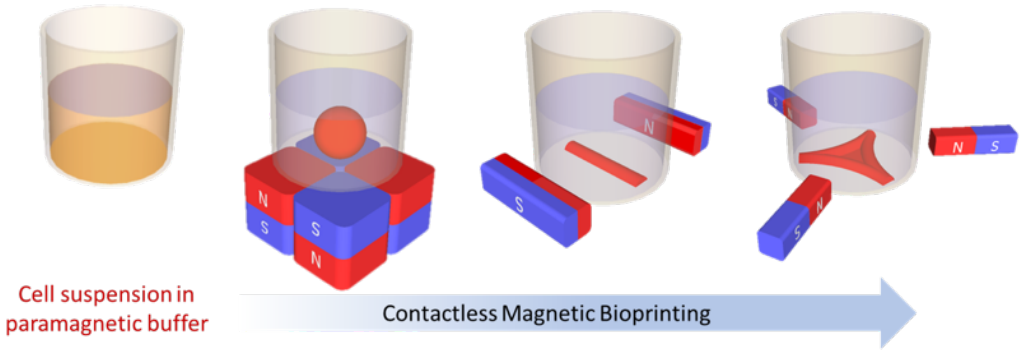

Figure 3.1: Schematic for macroscale method to print in situ cell assembles of different sizes and morphologies.

A typical method to create 3D cell structures utilizes the hanging drop technique, which limits assemblies to spherical geometries of relatively small sizes.[26] While 3D bioprinters deposit cells or their aggregates in layers with spatial precision,[27] they are relatively slow and expensive, and use nozzles, which can damage cells unless embedded in a hydrogel[28]. Other alternative methods include label-free manipulation of cells, for example electrophoresis, and acoustophoresis. Such methods employ external fields, subjecting cells to body forces thereby serving several applications such as continuous separation of cells from a mixture within a microfluidic channel with high concentration and throughput. However, while electrophoresis suffers from laborious electrode fabrication, and microfluidic design and assemblies, acoustophoresis is restricted to concentrate cells at the pressure nodes along the length of a microchannel.

Since it does not require nozzles, additional surfaces, electrodes, or microfluidics, diamagnetophoretic printing is an *in situ* method that requires only cells, an appropriate paramagnetic medium and a suitable magnetic field. Due to the differential force that cells experience *in situ* in such a system, they move towards regions of lower magnetic field strength, $\mathbf{B}_{low}$. While some cells settle there immediately, others are transported away through inertia, but the differential force returns these escaped cells back towards $\mathbf{B}_{low}$. This back and forth cell motion induces fluid recirculation through momentum transfer between the cells and fluid, settling an increasing number of cells around $\mathbf{B}_{low}$ over time with an equivalent depletion elsewhere in the medium. The recirculation eventually ceases, as shown in **Figure 3.2**. Additionally, after assembly cells can still be subjected to varying magnetic fields, which is anticipated to induce mechanical stresses on the mimicking those in physiological conditions. This may add to the degree of similarity between *in vitro* and *in vivo* experimentation.

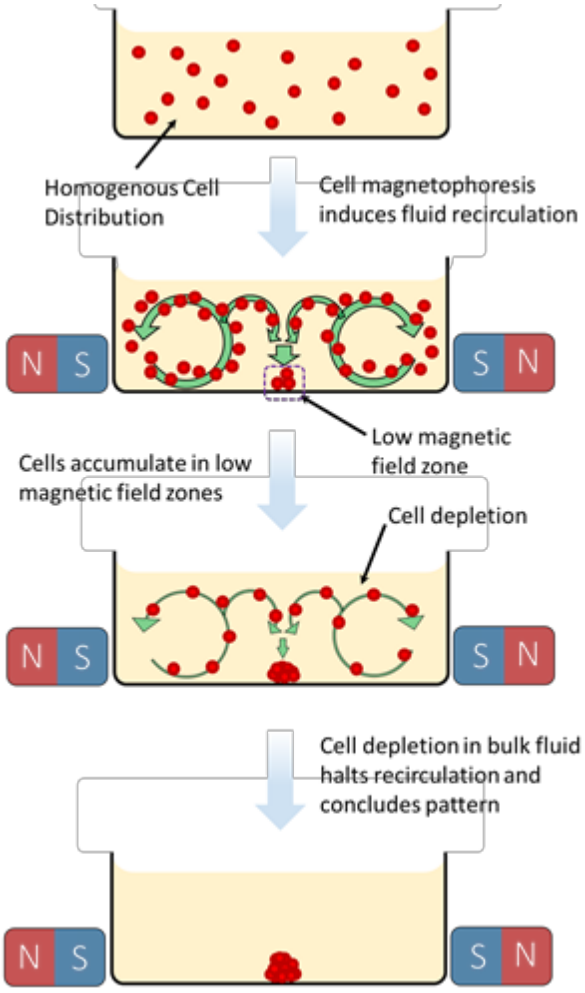

Figure 3.2: Macroscale in situ 3D printing of cells. During diamagnetophoretic cell printing, cells are homogeneously suspended in a paramagnetic medium. The differential diamagnetic forces between the cells and the medium move cells towards regions of lower magnetic field strength $\mathbf{B}_{low}$. While some cells settle there immediately, others are transported away due to their inertia but, due to the differential force, return towards $\mathbf{B}_{low}$. This back and forth cell motion induces fluid recirculation, eventually settling all cells around $\mathbf{B}_{low}$ after which fluid recirculation ceases. The coupling between the magnetic field, diamagnetophoretic force on the

cells and fluid recirculation allows control over the sizes and morphologies of the printed features.

The magnetic force on a cell,[16, 22, 29] $\mathbf{F}_m$ is expressed as

$$\mathbf{F}_m = ((\chi_c - \chi_m)/2\mu_0)V_c\nabla|\mathbf{B}|^2, \quad (3.1)$$

where χ_c and χ_m denote the magnetic susceptibilities of the cell and fluid medium, V_c and μ_o the cell volume and permeability of free space, and $\nabla|\mathbf{B}|$ the magnetic field gradient. Hence, $\mathbf{F}_m$ depends on the (1) difference in the magnetic susceptibilities between the cell and fluid medium, (2) cell volume, and (3) magnetic field gradient. Assuming that all cells are spherical, the drag force that they experience due to Stokes flow is $\mathbf{F}_d = 6\pi\eta\mathbf{U}R$, where η denotes the medium viscosity, **U** cell velocity, and R cell radius. This force can be appropriately modified for cells with other sizes and morphologies. Since cells have negligible inertia, $\mathbf{F}_d = \mathbf{F}_m$. Hence, the terminal velocity of a cell with $V_c = (4/3)\pi R^3$ is,

$$\mathbf{U} = 2R^2\mathbf{f}_c/(9\eta) \quad (3.2)$$

Where $\mathbf{f}_c$, the magnetic body force on the cell is given as,

$$\mathbf{f}_c = ((\chi_c - \chi_m)/2\mu_0)\nabla|\mathbf{B}|^2 \quad (3.3).$$

Assuming a strong paramagnetic host medium, $(\chi_c - \chi_m) \approx -\chi_m$,

$$\mathbf{U} = -((R^2\chi_m)/9\eta\mu_0)\nabla|\mathbf{B}|^2, \text{ i.e.,} \quad (3.4)$$

the terminal velocity scales with R^2. The printing time and induced convection depend on $\mathbf{U}$. Hence larger cells undergo more rapid magnetophoresis and print *in situ* patterns faster

than their smaller counterparts. Furthermore, it is anticipated that since adherent cells form clusters, their larger equivalent radius would improve the print speed over that when non-adherent cells that have smaller sizes are used.

Dissolving gadopentatic acid (Gd-DTPA) in phosphate-buffered saline (PBS) imparts paramagnetic properties to the solution. We created four solutions at 300 K with different Gd-DTPA concentrations and loaded 50 μL of each sample in a size 5 capsule to conduct superconducting quantum interference device (SQUID) measurements. For reference, a sample containing only PBS was also examined. The SQUID performed a temperature sweep from 5 to 30 K that provided 25 measurements, one magnetic moment measurement (emu) per degree, with a 1 kOe field. The paramagnetic susceptibility was calculated using the inverse Curie-Weiss law. This susceptibility increases with increasing Gd-DTPA concentration, as shown in **Figure 3.3**(**a**), where $\chi_m = 7.00\times10^{-6}$, 2.33×10^{-6}, 1.33×10^{-6}, and 1.00×10^{-6} for the 0.2 M, 0.1 M, 0.05 M and 0.025 M Gd-DTPA concentrations. The PBS sample exhibits typical diamagnetic response with a negative susceptibility $\chi_m = -2.32\times10^{-7}$ and no temperature dependence. Therefore, a buffer solution can be tailored by varying the added amount of a paramagnetic salt, which alters the diamagnetic response of cells. This variation can be controlled to print *in situ* macroscopic cellular structures.

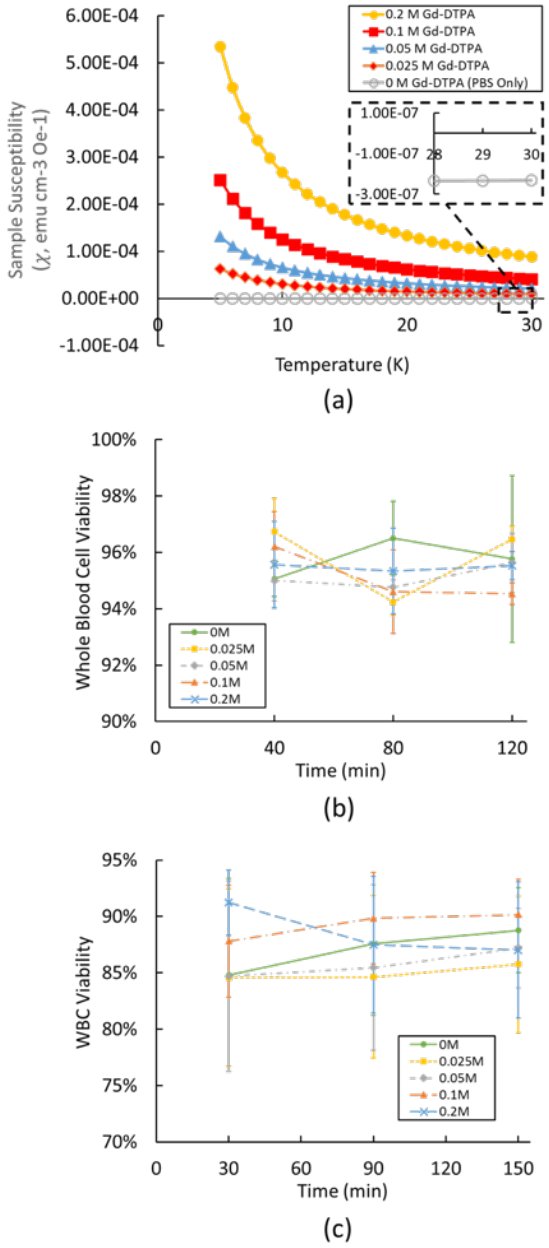

Figure 3.3: Gadopentatic acid (Gd-DTPA) susceptibility measurements and cell viability. (**a**) Magnetic susceptibility measurements for Gd-DTPA concentrations of 0.2 M, 0.1 M, 0.05 M, 0.025 M and 0 M in phosphate -buffered saline (PBS) using SQUID. Cell viability for (**b**) whole blood and (**c**) WBCs in

mixtures with the aforementioned four Gd-DTPA concentrations. (The 0 M sample contains only PBS). Cell viability was determined with trypan blue stain by live cell counts at each time instant compared to initial live cell count. Measurements were made 40, 80 and 120 mins for whole blood and 30, 90 and 150 min for WBCs after the cells were introduced into the mixtures and do not show significant influence of Gd-DTPA concentration or time on cell viability when compared to a PBS only buffer solution.

The viability of whole human blood was first investigated to examine Gd-DTPA toxicity towards them for the four aforementioned concentrations. The pH of the solutions was initially acidic ~1.7, but was adjusted to the isotonic value of ~ pH 7.4 with sodium hydroxide and hydrochloric acid. The whole blood was first suspended in each Gd-DTPA solution and incubated at standard conditions (37^{o}C and 5% CO_2) for 40, 80 and 120 mins, along with another sample that contained the blood in a reference PBS-only control. Viability of whole blood was examined using a Nexcelom Cellometer Auto 2000 Cell Viability Counter after staining with trypan blue, results for which are present in **Figure 3.2(b**). High salt concentrations increase the osmotic pressure from its isotonic value of ~ 310 mOsm[15] and cause cells to lyse.[17] However, **Figure 3.3**(**b**) shows that, even at the highest concentration of 0.2 M, Gd-DTPA toxicity cannot be distinguished from that of PBS within experimental error. The exposure time over the test duration of 120 mins has negligible influence on viability. Following a similar protocol, the viability of only white blood cells (WBCs) was examined. WBCs were separated from whole human blood using centrifugation and ficol separation. Their viability are presented for 30, 90 and 150 mins

incubation times in **Figure 3.3**(**c**). Again the toxicity of Gd-DTPA is found to be negligible compared to the PBS only sample over the duration of the experiment of 150 min.

Next, we demonstrate contactless label-free *in situ* 3D printing of cell assemblies for (1) two magnetic configurations that create (a) rectangular bar and (b) three-pointed star morphologies, and (2) a magnet bank that is arranged to create whole blood spheroids of monotonically varying sizes. For the first case, the buffer solution consisted of 450 μL of 0.2M Gd-DTPA in PBS. Here, 3 μL of human whole blood was drawn and mixed with the paramagnetic buffer using a micropipette in a circular glass vial. Neodymium N52 magnets were placed in two different configurations to create a magnetic field whose strength was minimum at the center of the vial. These two configurations, presented schematically in **Figure 3.4**, includes (1) two adjacent magnets with 180° pole angles placed side by side, and (2) three magnets with 120° pole angles placed next to each other. The configurations were also simulated based on the actual experimental design to determine the force phase portrait on cells using the Finite Element Magnetic Method (FEMM, version 4.2) in combination with MATLAB software (R2014b, The Mathworks, Inc.).

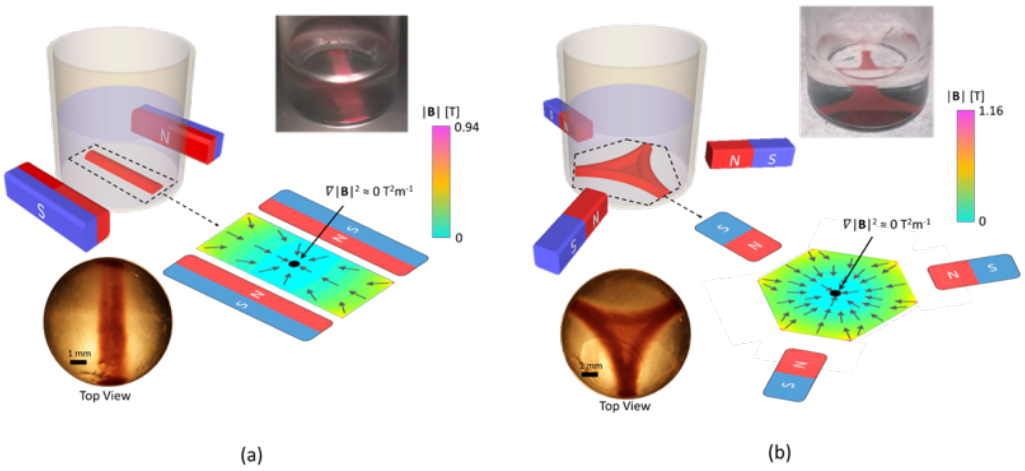

Figure 3.4: In situ 3D printing of cells is assisted by magnetically-induced fluid recirculation. Simulations show the magnetic force $\mathbf{F}_m$ phase portrait for cells in a highly paramagnetic buffer solution with a single magnetic field minima, where $\nabla|\mathbf{B}|^2 \sim 0\ T^2m^{-1}$, regardless of magnet configuration. However, while simulations predict cell convergence to the magnetic minima, experimental observations reveal the importance of fluid recirculation in defining the final bioprinted feature. Thus when a homogeneous cell distribution is first introduced to a magnetic field, macroscale cell diamagnetophoresis, induces fluid recirculation. Varying the magnet configuration induces different recirculation patterns and thus dissimilar cell transport, which creates 3D cell assemblies with diverse morphologies, such as (**a**) a line, or (**b**) three pointed star.

The simulations reveal that the magnetic force $\mathbf{F}_m$ experienced by diamagnetic RBCs in the paramagnetic buffer has a single minimum value, regardless of the multiple magnet configurations employed. This single $\mathbf{F}_m$ minimum implies that cells should converge around its spatial location, resulting in spherical assemblies. This is clearly not the case in

the experiments since the simulations do not account for fluid recirculation or cell-substrate adhesion. Hence, instead of agglomerating symmetrically around the $\mathbf{F}_m$ minimum, different 3D cell morphologies are printed due to the influence of fluid circulation. The force phase portrait, however, can foretell changes in fluid circulation associated with different magnet arrangements as seen by the vastly different phase portraits in **Figures 3.4**(**a**) and (**b**). Changing the magnet configuration, thus, alters the recirculation, which modifies cell transport and creates different morphologies for the 3D cell assemblies, such as the (**a**) bar, or (**b**) three pointed star. Since the final settling place of cells depend on recirculation currents, the bioprinted features will inherently have variations in its thickness. For example, the relative thickness of the 3D cell assemblies in **Figure 3.4**(**a**) and (**b**) is conveyed qualitatively through the intensity of light passing through the features, where lighter colours is interpreted as thinner sections compared to darker thicker ones. The bar feature in **Figure 3.4**(**a**) has thinner peripheries than its center, while the center section in **Figure 3.4**(**b**) is thinner than its thicker peripheries, which highlight the main areas of cell settlement. Once printed *in* situ, the cell assemblies remain unchanged even two hours after the experiment has concluded by removing the magnets. Once the magnetic field is removed, convection currents are no longer present and there is no driving force to move the cells.

Other magnetic field geometries create spheroid assemblies. In the configuration of **Figure 3.5**(**a**), the poles of adjacent magnets alternate to produce a spatially varying field along the cuvette that contains a whole blood suspension in 0.15 M Gd-DTPA-PBS buffer. Simply tilting the cuvette results in the formation of blood spheroids, which are separated

by different sizes *in situ* as shown in **Figure 3.5**(**b**). When the separation between a drop and the magnet that is placed below is made smaller, the magnetic field strength increases, which reduces the sizes of the whole blood spheres. The experiment was repeated three times to ensure the repeatability of spheroid formation. The variation in the sizes of different blood spheroids, of characteristic 600 – 1000 μm dimensions, formed with an inclination angle of ~ 5° at various spatial locations is shown in **Figure 3.5**(**c**). For each location A-E in **Figure 3.5**(**b**), the measured standard deviation of spheroid diameters are all within 5% of the average calculated diameter. This form of control over spherical cell assembly is superior to what is possible, for instance, with the hanging drop method. Since different size cell spheres are expected to have different cell densities, the *in situ* bioprinting method is capable of inducing mechanical stresses on a cell assembly by simply varying the magnet-cuvette separation. Subjecting a cell assembly to mechanical stress can mimic physiological conditions, which is not readily possible with conventional methods.

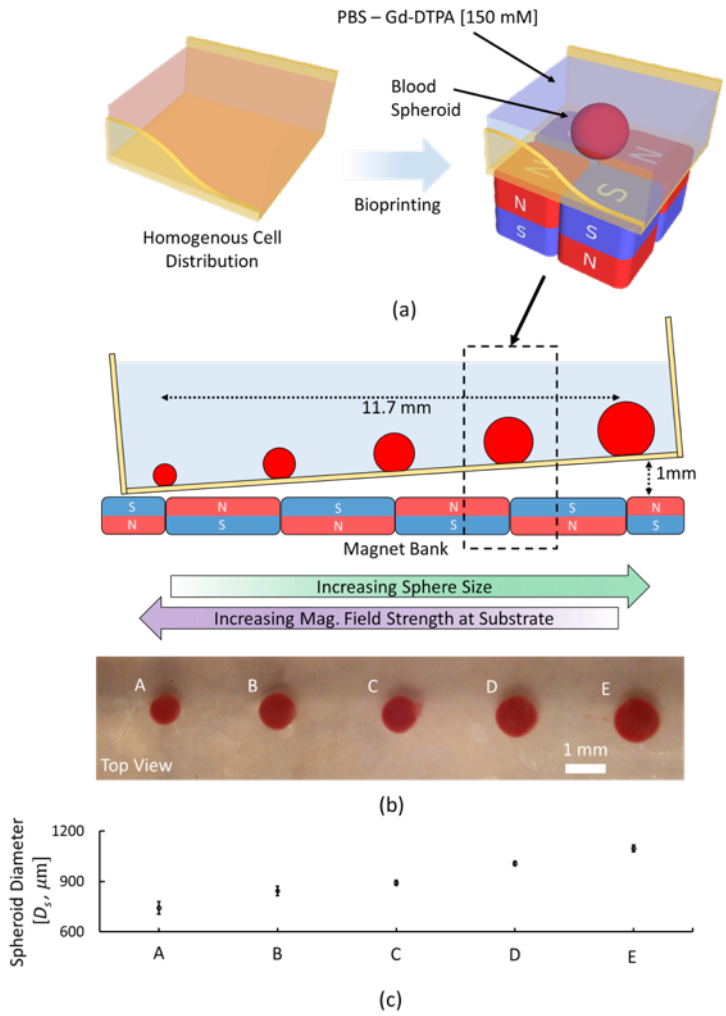

Figure 3.5: Blood spheroids of different diameters. (**a**) A 6 μL homogenous suspension of whole blood cells is mixed in a cuvette with a solution containing 1 mL PBS and 150 mM Gd-DTPA. (**b**) Once the cuvette is placed on the magnet bank, the local diamagnetic forces produce spheroidal cell assemblies. Because the cuvette is tilted, the magnetic field strength varies along the bank. As the local separation between the assembly and magnet bank increases, the diamagnetic force experienced by a printed assembly decreases, producing larger spheroids. (**c**) The

experiment was repeated three times to ensure repeatability. There exists a linear correlation between spheroid size and magnet separation. This simple arrangement provides a straightforward method to control spheroid size, which likely also influences the density of the cell assembly.

3.4 Conclusions

This method of printing 3D cell assemblies could be miniaturized to achieve better control over the resolution and smaller sizes of spheroids by either using smaller magnets or fabricating magnetic microstructures using lithographic or micromachining techniques. The microstructures could thus provide high gradient magnetic field, thus enabling patterning of cells with single cell resolution. The limiting factor with such miniaturization is the strength of the magnetic field necessary for diamagnetophoresis and hence need further study on the topic.

In summary, we present the first realization of a contactless bioprinting technique that magnetically manipulates diamagnetic whole blood in a nontoxic paramagnetic Gd-DTPA and PBS medium to print *in situ* label-free 3D cell assemblies. Although there is no practical significance to assembling whole blood, this method can be used to manipulate mammalian cells into 3D assemblies for clinical and/or research purposes. The bioprinting method does not contain nozzles, the surfaces of which can become sources of contamination or where cells can adhere. Due to the difference between their susceptibilities, diamagnetic cells in a paramagnetic medium experience a differential force that moves them towards region of lower magnetic field strength $\mathbf{B}_{low}$. While some cells

immediately settle there, others are transported away through inertia, only to return towards $\mathbf{B}_{low}$. This back and forth cell motion triggers fluid recirculation, which eventually ceases. The terminal velocity of a cell scales with its size. Hence, larger cells and adhered clusters are expected to undergo more rapid magnetophoresis and print *in situ* patterns faster than their smaller counterparts. The buffer solution can be tailored to vary the diamagnetic response of the cells and tune the bioprinting method. We print 3D cell assemblies with (1) two magnetic configurations that create (a) rectangular bar and (b) three-pointed star morphologies, and (2) a magnet bank that creates whole blood spheroids of varying sizes. Since the different size spheres are expected to have different cell densities, this bioprinting technique can also induce mechanical stresses to mimic physiological conditions. Printing 3D cell assemblies and patterns can further improve tissue engineering, cell-on-chip devices and microfluidic drug screening applications.

3.5 Acknowledgements

General: We thank Laura de Rooij of the McMaster Stem Cell and Cancer Research Institute for assisting with whole blood viability testing. We thank Dr. Jonathan Bramson of the McMaster Immunology Research Center for helpful discussions. We thank Dr. Paul Dube of the Brockhouse Institute for Materials Research, McMaster University for his assistance with SQUID measurements.

Funding: This work is supported by a Natural Sciences and Engineering Research Council of Canada (Grant RGPIN-2014-04066) Discovery Grant (NSERC-DG), Canada Foundation for Innovation John R. Evans Leaders Fund (CFI-JELF), Ontario Research

Fund Research Infrastructure (ORF-RI) grants (Grant no. 33016) and a seed grant from the Fraunhofer-McMaster Project Center for Biomedical Engineering and Advanced Manufacturing (BEAM).

Author contributions: A. R. Abdel Fattah, E. Meleca, and S. Mishriki have contributed equally to the work. The manuscript was written through contributions of all authors. All authors have given approval to the final version of the manuscript.

3.6 References

1. Ghosh, S.; Kumar, S.; Puri, I.; Elankumaran, S., Magnetic assembly of 3D cell clusters: visualizing the formation of an engineered tissue. *Cell proliferation* **2016,** *49* (1), 134-144.

2. Dababneh, A. B.; Ozbolat, I. T., Bioprinting Technology: A Current State-of-the-Art Review. *Journal of Manufacturing Science and Engineering* **2014,** *136* (6), 061016-061016.

3. Abdel Fattah, A. R.; Ghosh, S.; Puri, I. K., High gradient magnetic field microstructures for magnetophoretic cell separation. *J Chromatogr B Analyt Technol Biomed Life Sci* **2016,** *1027*, 194-9.

4. Shen, F.; Hwang, H.; Hahn, Y. K.; Park, J. K., Label-free cell separation using a tunable magnetophoretic repulsion force. *Anal Chem* **2012,** *84* (7), 3075-81.

5. David klelville, F. P. a. S. R., Fractionation of Blood Components Using High Gradient Magnetic Separation. *IEEE Transactions on Magnetics* **1982,** *MAG-18* (6), 1680-1685.

6. Pauling, L.; Coryell, C. D., The Magnetic Properties and Structure of Hemoglobin, Oxyhemoglobin and Carbonmonoxyhemoglobin. *PROC. N. A. S.* **1936,** *22*, 210-216.

7. Fabry, M. E.; San George, R. C., Effect of Magnetic Susceptibility on Nuclear Magnetic Resonance Signals Arising from Red Cells: A Warning. *Biochem.* **1983,** *22*, 4119-4125.

8. Savicki, J. P. S.; Lang, G.; Ikeda-Saito, M., Magnetic Suceptibility of oxy- and carbonmonoxyhemoglobins. *Proc. Natl. Acad. Sci. USA* **1984,** *81*, 5417-5419.

9. Hackett, S.; Hamzah, J.; Davis, T. M.; St Pierre, T. G., Magnetic susceptibility of iron in malaria-infected red blood cells. *Biochim Biophys Acta* **2009,** *1792* (2), 93-9.

10. Spees, W. M.; Yablonskiy, D. A.; Oswood, M. C.; Ackerman, J. J. H., Water Proton MR Properties of Human Blood at 1.5 Tesla: Magnetic Susceptibility, T1, T2, T* and Non-Lorentzian Signal Behavior. *Magn. Reson. Med.* **2001,** *45*, 533-542.

11. Zborowski, M.; Ostera, G. R.; Moore, L. R.; Milliron, S.; Chalmers, J. J.; Schechter, A. N., Red Blood Cell Magnetophoresis. *Biophys. J.* **2003,** *84* (2638-2645).

12. Inglis, D. W.; Riehn, R.; Sturm, J. C.; Austin, R. H., Microfluidic high gradient magnetic cell separation. *J. Appl. Phys.* **2006,** *99* (8), 08K101.

13. Jung, J.; Han, K.-H., Lateral-driven continuous magnetophoretic separation of blood cells. *Appl. Phys. Lett.* **2008,** *93* (22), 223902.

14. Han, K. H.; Frazier, A. B., Paramagnetic capture mode magnetophoretic microseparator for high efficiency blood cell separations. *Lab Chip* **2006,** *6* (2), 265-73.

15. Graham, M. D., Comparison of Volume and Surface Mechanisms for Magnetic Filtration of Blood Cells. *J. Phys.-Paris Colloques* **1984,** *45* (C1), C1-779-C1-784.

16. F. Paul, S. R., Direct Magnetic Separation of Red Blood Cells from Whole Blood. *Nature* **1975,** *225*, 706.

17. Melville, D.; Paul, F.; Roath, S., Fractionation of Blood Components Using High Gradient Magnetic Sepration. *IEEE Trans. Magn.* **1982,** *MAG-18*, 1680-1685.

18. Furlani, E. P., Magnetophoretic separation of blood cells at the microscale. *J. Appl. Phys. D* **2007,** *40* (5), 1313-1319.

19. M. Takayasu, D. R. K., J. V. Minervini, Continuous Magnetic Separation of Blood Components from Whole Blood. *IEEE Transactions on Applied Superconductivity* **2000,** *10* (1), 927-930.

20. Miltenyi, S.; Muller, W.; Weichel, W.; Radnruch, A., High Gradient Magnetic Cell Separation With MACS. *Cytometry* **1990,** *11*, 231-238.

21. Inglis, D. W.; Riehn, R.; Austin, R. H.; Sturm, J. C., Continuous microfluidic immunomagnetic cell separation. *Appl. Phys. Lett.* **2004,** *85* (21), 5093.

22. Morgunov, R. B.; Mushenok, F. B.; Aldoshin, S. M.; Sanina, N. A.; Yur'eva, E. A.; Shilov, G. V.; Tkachev, V. V., Thermally-induced paramagnetism of spiropyrane iodides. *New Journal of Chemistry* **2009,** *33* (6), 1374.

23. Tsunehisa Kimura; Yukiko Sato; Fumiko Kimura; Masakazu Iwasaka; Ueno, a. S., Micropatterning of Cells Using Modulated Magnetic Fields. *Langmuir* **2005,** *21*, 830-832.

24. Winkleman, A.; Gudiksen, K. L.; Ryan, D.; Whitesides, G. M.; Greenfield, D.; Prentiss, M., A magnetic trap for living cells suspended in a paramagnetic buffer. *Applied Physics Letters* **2004,** *85* (12), 2411.

25. Durmus, N. G.; Tekin, H. C.; Guven, S.; Sridhar, K.; Arslan Yildiz, A.; Calibasi, G.; Ghiran, I.; Davis, R. W.; Steinmetz, L. M.; Demirci, U., Magnetic levitation of single cells. *Proc Natl Acad Sci U S A* **2015,** *112* (28), E3661-8.

26. Tasoglu, S.; Demirci, U., Bioprinting for stem cell research. *Trends in biotechnology* **2013,** *31* (1), 10-19.

27. Xu, C.; Zhang, M.; Huang, Y.; Ogale, A.; Fu, J.; Markwald, R. R., Study of Droplet Formation Process during Drop-on-Demand Inkjetting of Living Cell-Laden Bioink. *Langmuir* **2014,** *30* (30), 9130-9138.

28. Malda, J.; Visser, J.; Melchels, F. P.; Jüngst, T.; Hennink, W. E.; Dhert, W. J.; Groll, J.; Hutmacher, D. W., 25th anniversary article: engineering hydrogels for biofabrication. *Advanced materials* **2013,** *25* (36), 5011-5028.

29. Tsutsui, H.; Ho, C. M., Cell Separation by Non-Inertial Force Fields in Microfluidic Systems. *Mech. Res. Commun.* **2009,** *36* (1), 92-103.

4 Rapid magnetic 3D Printing of Cellular Structures with MCF-7 Cell Inks

This chapter is reproduced from *Rapid magnetic 3D printing of cellular structures with MCF-7 cell inks, 2019, Research, **Sarah Mishriki**, Abdel Fattah Abdel Rahman, Tobias Kammann, Rakesh P. Sahu, Fei Geng, and Ishwar K. Puri, https://doi.org/10.34133/2019/9854593*. The author of this thesis is the main contributor of this publication.

4.1 Abstract

A contactless label-free method using a diamagnetophoretic ink to rapidly print three-dimensional (3D) scaffold-free multicellular structure is described. The inks consist of MCF-7 cells that are suspended in a culture medium to which a paramagnetic salt, diethylenetriaminepentaacetic acid gadolinium (III) dihydrogen salt hydrate (Gd-DTPA), is added. When a magnetic field is applied, the host fluid containing the paramagnetic salt is attracted towards regions of high magnetic field gradient, displacing the ink towards regions with a low gradient. Using this method, 3D structures are printed on ultra-low attachment (ULA) surfaces. On a tissue culture treated (TCT) surface, a 3D printed spheroid coexists with a two-dimensional (2D) cell monolayer, where the composite is termed as a 2.5D structure. The 3D structures can be magnetically printed within 6 hours in a medium containing 25 mM Gd-DTPA.

The influence of the paramagnetic salt on MCF-7 cell viability, cell morphology and ability of cells to adhere to each other to stabilize the printed structures on both ULA and TCT surfaces is investigated. Gene expressions of hypoxia-inducible factor 1-alpha (*HIF1α*) and

vascular endothelial growth factor (*VEGF*) allow comparison of the relative stresses for the printed 3D and 2.5D cell geometries with those for 3D spheroids formed without magnetic assistance. This magnetic printing method can be potentially scaled to a higher throughput to rapidly print cells into 3D heterogeneous cell structures with variable geometries with repeatable dimensions for applications such as tissue engineering and tumor formation for drug discovery.

4.2 Introduction

Two-dimensional (2D) environments, where cells are grown on a tissue culture treated (TCT) surface, have limited clinical relevance since they do not correctly mimic the interactions that influence living cells. In contrast, three dimensional (3D) models provide more accurate representations of physiologic environments. For 3D cell geometries composed of human carcinoma cells, these interactions involve cell-cell signaling, presence of extracellular matrix (ECM), mechanical cues, hypoxic environments, gene expressions, and drug resistance[1-4]. Examples include multicellular tumors[5-6], mammospheres formed with mammary cells[7], and tissue spheroids that are embedded in a hydrogel matrix as building blocks to produce larger cell structures[8].

Traditional methods to create 3D spheroid-like cultures require that suspended cells adhere to each other to form nucleation sites that initiate 3D growth. This necessitates the use of non-adhesive surfaces or a liquid-air interface to prevent adherent cells from coalescing and spreading into 2D monolayers. Thus, 3D aggregates are typically grown in a hanging drop setup[9] or on ultra-low attachment (ULA) surfaces[10]. Since culturing

techniques limit the ability of some cell lines of forming 3D structures, chemically formulated media, containing reduced amounts of nutrient serum[11] growth factors and additives (including L-glutamine, epidermal growth factor (EGF), basic fibroblast growth factor (bFGF), and reconstituted basement membrane (rBM)[6, 12-14]), are used.

When adherent cells are suspended in medium on flat-bottom ULA plates, multiple 3D masses can be produced in a single well. However, since these masses have non-uniform dimensions, the numbers of spheroids vary from well to well. The hanging drop method circumvents this limitation, allowing cells to aggregate along the liquid-air interface of a cell suspension[15], enabling a structure with uniform dimensions and a specific number of cells for each spheroid. Despite its advantages, the hanging drop method is laborious and time consuming, and also difficult for producing large numbers of spheroids, thereby limiting throughput[16]. Advances in cell manipulation and microscale 3D cell structure formation have incorporated the production of a high-gradient magnetic field in microfluidic devices[17] and for label-free magnetic manipulation[18-22], and into agarose[5] and polydimethylsiloxane (PDMS)[23] microwells.

The addition of diethylenetriaminepentaacetic acid gadolinium (III) dihydrogen salt hydrate (Gd-DTPA) to a cell suspension transforms the medium into a magnetic bioink, where the liquid component of the ink has a higher magnetic susceptibility than the cells contained within it. Therefore, the paramagnetic liquid is more susceptible to a magnetic field than are the suspended diamagnetic cells suspended[18, 24-25], i.e., the liquid is preferentially attracted towards the magnetic field while the cells are not. Placing magnets at suitable locations induces ink movement within a vessel, which focuses the suspended

cells into 3D structures at locations of lower magnetic field strength, a process called diamagnetophoresis. Since cell patterning through diamagnetophoresis can be controlled and the method foregoes use of nozzles and complicated equipment which can introduce contaminants, it is a convenient technique to rapidly print multicellular spheroids. Potential applications include tissue engineering and drug discovery, allowing the emulation of *in vivo* phenomena in an adjustable *in vitro* environment.

We have previously demonstrated a method to print 3D cellular structures through diamagnetophoresis using a whole blood ink to demonstrate proof of concept[26], and another ink containing a binary mixture of mammalian cell cultures to observe morphological and phenotypic changes in a co-culture[27]. Although it is used as a magnetic resonance imaging (MRI) contrast agent, large Gd-DTPA concentrations can be toxic. Hence, we have evaluated the effect of the paramagnetic salt on human breast cancer cell lines[28]. Cells suspended in a Gd-DTPA medium can also be patterned through diamagnetophoresis on a TCT surface to which cells adhere, forming a relatively small central 3D lump, where a monolayer spreading outward from a central lump is useful for investigating cell migration and fabrication of co-cultures[27]. We call this latter geometry a 2.5D structure since it contains features of both a small 3D spheroid and a 2D monolayer of actively proliferating cells, traditionally observed in transwell assays[29-30]. This unique cell microarchitecture can be used to simultaneously observe a growing tumor with a non-cancerous, monolayer cell type, such as epithelial.

We print five types of cell structures with and without diamagnetophoresis using bioinks containing MCF-7 (Michigan Cancer Foundation-7) cells, a human breast cancer

cell line. These structures are created to compare diamagnetophoretic printing with traditional methods to characterize the time required to forms spheroids, their dimensions and gene expressions. Magnetically assisted bioprinting rapidly prints reproducible 3D and 2.5D structures without compromising the behaviours of the printed structures.

4.3 Results

4.3.1 Effect of Gd-DTPA on cell proliferation

The paramagnetic culture medium consists of Gd-DTPA salt dissolved in DMEM supplemented with 10% FBS, as described in Materials and Methods. Since the salt is toxic at high concentrations and prolonged exposures[18, 27-28, 31], we assess the proliferation of MCF-7 monolayers incubated with 0, 1, 10, 25, 50, 75, 100, and 125 mM Gd-DTPA dissolved in the cell culture medium. For cells exposed to each concentration of Gd-DTPA, an MTT assay indirectly quantifies viable cells at 3, 24, 48, and 72 hours through mitochondrial activity. **Figure 4.1**(**a**) shows that, as the exposure time and Gd-DTPA concentration increase, the number of viable cells is diminished. At three hours of exposure to Gd-DTPA, there is an observable increase in cell proliferation, but at 10 mM there is a decrease in cell proliferation. The proliferation increase is explained in part by the increase in the metabolic activity of the cells in presence of Gd-DTPA. Regardless, the effect of Gd-DTPA is indistinguishable from that of the control (0 mM Gd-DTPA) within the first 24 hours of exposure to the salt, as shown in **Figure 4.1**(**b**), which reports the cell viability normalized to that for a Gd-DTPA-free medium for each incubation period. For all concentrations of Gd-DTPA, at 3 and 24 hours of incubation variabilities in the percent

normalized viability are insignificant using SEM and a two-way ANOVA with Bonferroni post-tests.

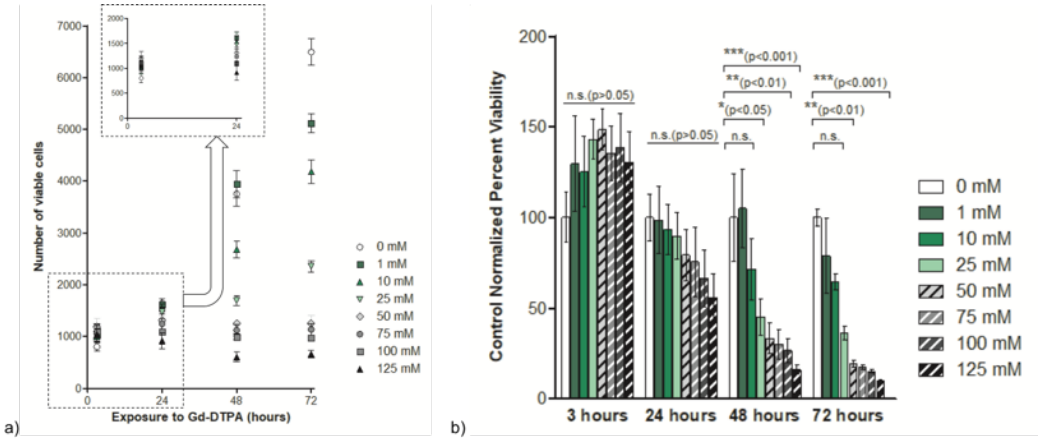

Figure 4.1: Effect of Gd-DTPA on cell proliferation. Approximately, 1000 MCF-7 cells are incubated in 0, 1, 10, 25, 50, 75, 100, and 125 mM Gd-DTPA. Cell proliferation is measured by MTT assay at 3, 24, 48, and 72 hours. The viable cells are (**a**) quantified by a standard curve (for n=3 analyzed by standard error) and (**b**) control normalized percent viability using Gd-DTPA free medium (0 mM) using SEM and a two-way ANOVA with Bonferroni post-tests to evaluate the relative differences in viability for each concentration of Gd-DTPA. A $p < 0.05$ is considered to be statistically significant. As the Gd-DTPA concentration increases, cell proliferation is reduced. However, at 24 hours, the effects of Gd-DTPA to cell viability are similar to that of Gd-DTPA free medium. Significant decreases in cell viability are observed for MCF-7 cells in 25 mM and above Gd-DTPA at 48 and 72 hours. Therefore, exposure to Gd-DTPA should be limited to a maximum of 24 hours in order to limit harmful effects of Gd-DTPA on cell proliferation.

4.3.2 Effect of Gd-DTPA on cell morphology

The appropriate incubation period for MCF-7 cells in Gd-DTPA and the influence of a magnetic field for cell patterning are next evaluated. **Figure 4.2** presents results for MCF-7 cells incubated on ULA and TCT surfaces in the 0, 1, 10, 25, 50, 75, 100, and 125 mM Gd-DTPA solutions. Cell proliferation is observed at 1, 3, 6, and 24 hours (**Figure 4.1**). This indicates that Gd-DTPA has a limited effect on proliferation, however observations to observe the longer-term effects of Gd-DTPA are needed. For the ULA plate (**Figure 4.2**(**a**)), there is no difference between cells contained in all concentrations of Gd-DTPA and the Gd-DTPA-free medium (0 mM) at 1 and 3 hours. At 6 hours, cell-cell adhesion observed through a transition from flat to fused structures is only seen for 0-25 mM Gd-DTPA solutions, resulting in robust 3D cellular assemblies. This indicates that higher concentrations of Gd-DTPA impede cell adhesion, which is required to produce 3D spheroids. At 24 hours, adhesion is observed for all Gd-DTPA concentrations. For cells incubated on TCT surfaces (**Figure 4.2**(**b**)), MCF-7 cells display a variety of morphologies as both time and Gd-DTPA concentrations increase, including circular single-cells prior to attachment to the TCT surface, as well as elongated structures after some time, providing evidence of cell-surface adhesion and attachment. Similar to cells on the ULA surface, from 1 to 3 hours Gd-DTPA concentrations of 50 mM and above prevent cell-surface adhesion. At 6 hours, cell-surface adhesion overcomes the influence of Gd-DTPA that limits cell-cell attachment. Therefore, the concentration of Gd-DTPA for cells on both surfaces is limited to 25 mM to produce either spheroids or healthy monolayers during a maximum exposure of 24 hours, which is the doubling time of MCF-7 cells.

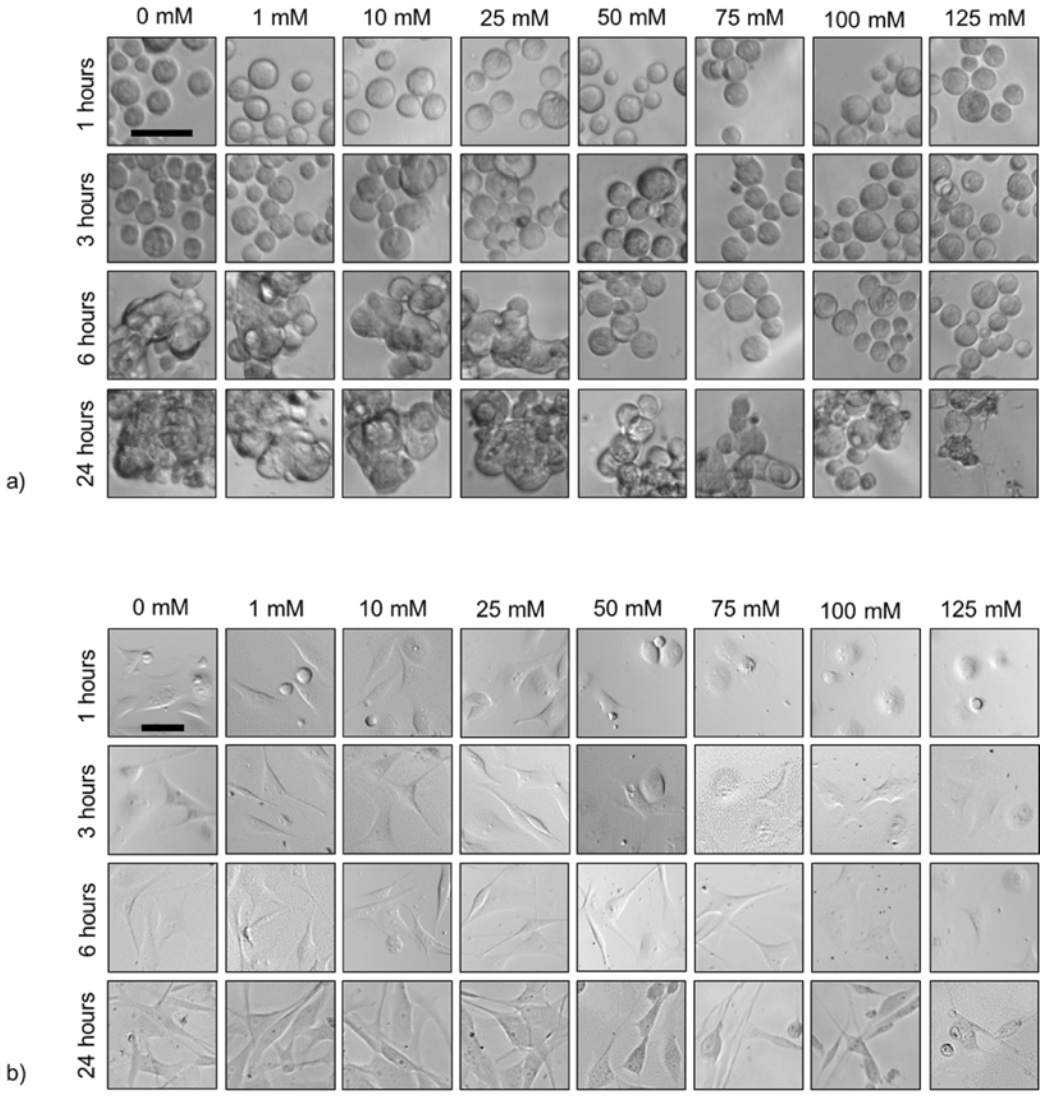

Figure 4.2: Effect of Gd-DTPA on cell morphology. MCF-7 cell morphologies in 0, 1, 10, 25, 50, 75, 100, and 125 mM Gd-DTPA (n=12) within 24 hours when incubated on (**a**) a ULA plate and (**b**) TCT plate. Within 6 hours, there are no apparent effects on cell morphology. At concentrations above 25 mM Gd-DTPA at 6 hours, the cell morphologies begin to differ from structures produced with 0 mM Gd-DTPA (control samples) for both ULA and TCT surfaces. In (**a**), as the

concentration of Gd-DTPA ≥ 50 mM, the ability of cells to adhere together diminishes. Cell-cell adhesion is key for formation of a 3D structure. Similarily, in (**b**) concentrations of ≥ 50 mM limit intercellular attachment within 1-3 hours exposure to Gd-DTPA. However, at 6 hours, intercellular adhesion overcomes the limiting influence of Gd-DTPA on cell-cell attachment. Therefore, to reduce harmful effects on cell morphology, exposure to Gd-DTPA should be limited to 25 mM for at most 6 hours. Scale bar = 50 μm.

4.3.3 Effect of Gd-DTPA to guide 3D and 2.5D structure formation

Figure 4.3 provides the minimum Gd-DTPA concentration required to coalesce cells together through diamagnetophoretic printing, which is determined by the formation of singular and concentrated 3D and multidimensional (2.5D) cell structures on ULA and TCT surfaces within 24 hours. For inks incubated in 0-25 mM Gd-DTPA and printed through diamagnetophoresis on the ULA surface (**Figure 4.3**(**a**)), while the 10 and 25 mM Gd-DTPA solutions allow 3D spheroids to form, the spheroid diameter *D* decreases significantly for both cases between 6 and 24 hours. Spheroids are unable to form within 6 hours of incubation with 0 and 1 mM solutions (**Figure 4.3**(**a**,**i**)). Use of a 10 mM solution results in the formation of multiple globular clusters and at 24 hours more than ten such clusters are observed (**Figure 4.3**(**a**,**ii**)). For cells magnetically printed on a TCT surface in 0-25 mM Gd-DTPA (**Figure 4.3**(**b**)), again with 10 and 25 mM Gd-DTPA solutions, the diameters of the centered and mostly circular 2.5D cell structures increase over 24 hours, while 0 and 1 mM solutions are unable to direct magnetic assembly (**Figure 4.3**(**b**,**ii**)). The

25 mM solution also produces smaller structures than one with 10 mM (**Figure 4.3**(**b**,**i**)). Therefore, the 25 mM Gd-DTPA solution is used for further experiments with both ULA and TCT surfaces due to its ability to form the desired 3D and 2.5D structures, and its limited influence on cell viability and morphology.

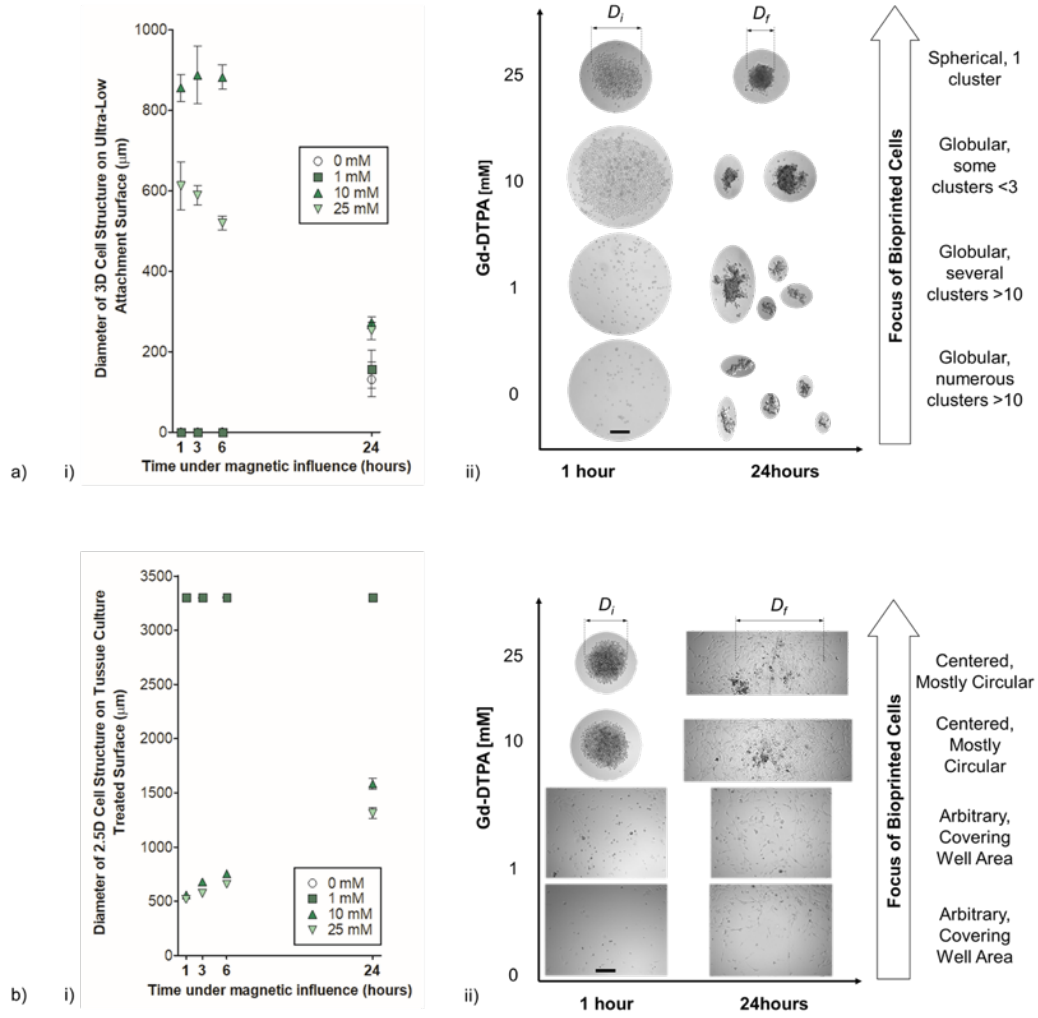

Figure 4.3: Effect of Gd-DTPA on diamagnetic cell printing. Formation of 3D and multidimentional cell structures (2.5D) through diamagnetophoresis on (**a**) a ULA surface and (**b**) a TCT surface. Approximately 1000 cells (n=5 analyzed by

SD) are incubated in both cases. For (**a**,**i**), 0 and 1 mM Gd-DTPA are insuffucuent to coalesce cells into a 3D structure. At 24 hours, accumulation of numerous globular cluster aggregates is observed. Only 25 and 10 mM Gd-DTPA are able to print cells through diamagnetophoresis. (**a**,**ii**) As the concentration of Gd-DTPA decreases from 25 mM, the formation of globular cell clusters increases and their ability to form a single spherical 3D structure is reduced. Only 25 mM is able to produce a single spherical cluster that remained intact until 24 hours. For (**b**,**i**), concentrations of 0 and 1 mM are again insufficient to coalesce cells into a 3D structure. The diameters of the cellular structures are equivalent those of their wells since these cells have formed 2D monolayers. Only 10 and 25 mM Gd-DTPA were able to produce a 3D structure, however, for (**b**,**ii**) 25 mM Gd-DTPA produced a denser 3D structure. Therefore, 25 mM Gd-DTPA is an appropriate concentration for forming 3D cell structures using diamagnetophoresis. Scale bar = 50 μm.

4.3.4 Optimization of incubation period with Gd-DTPA and magnetic field

The presence of Gd-DTPA is only required to coalesce, or print, the cell suspension, into a single, circular cell structure. After the intended structure has been printed, the medium can be changed to remove the paramagnetic salt. As shown in **Figure 4.3**, one hour is sufficient time to print cells into the region of minimal magnetic field strength. However, if the medium is subsequently replaced after 1 or 3 hours of incubation, the intercellular adhesion is insufficient for the spheroid to remain intact and maintain its structural integrity. After 6 hours, the cell-cell adhesion is sufficient to maintain the 3D morphology following a medium change for both ULA (**Figure 4.4**(**a**)) and TCT surfaces (**Figure 4.4**(**b**)). This is

consistent with observations of cell morphology from **Figure 4.2**, where intercellular adhesion is observed for the 25 mM Gd-DTPA solution after a 6-hour incubation. Hence, in our experiments, in the presence of magnetic field with a 25 mM solution, a 6 hour minimum incubation is maintained to ensure the integrity of a 3D MCF-7 structure following medium change.

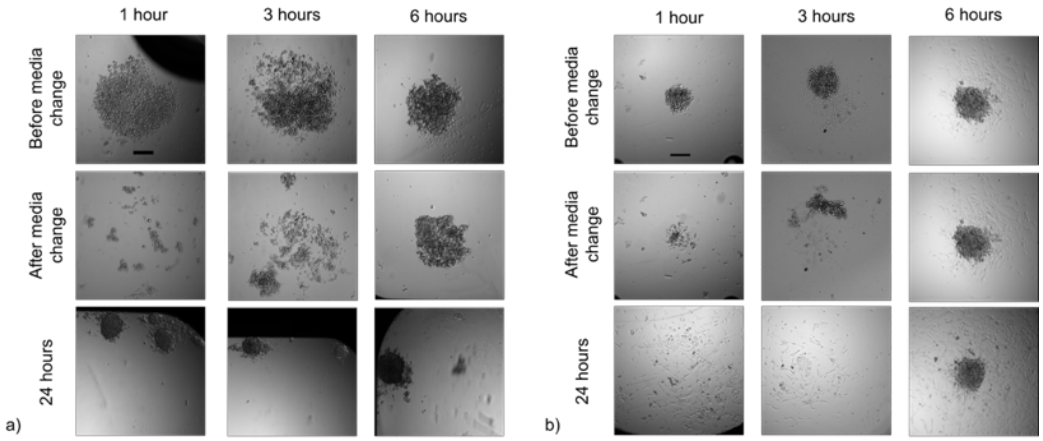

Figure 4.4: Incubation period of cells in the presence of external magnetic field. Cell aggregates following washes with a non-paramagnetic medium after diamagnetic 3D cell printing of (**a**) 5000 MCF-7 cells on a ULA surface (n=3) and (**b**) 3000 MCF-7 cells on a TCT surface (n=3) in 25 mM Gd-DTPA for 1, 3, 6, and 24 hours. Incubations periods indicate durations for exposure to the paramagnetic medium and the externally applied magnetic field after which the medium is replaced by 0 mM Gd-DTPA removed to prevent over-exposure of Gd-DTPA and the magnetic field. At 1 and 3 hours of incubation, the cells are successfully concentrated to the zones of low magnetic field strength, which are determined by the arrangements of the magnets. However, following medium changes to remove

Gd-DTPA, the 3D structures do not maintain their aggregated structures. Only for 6 hours exposure do the cells remain as a 3D structure following medium changes. Therefore, a minimum of 6 hours is sufficient for producing a single cell structure for cell suspensions in both ULA and TCT surfaces. Scale bar = 200 μm.

4.3.5 Formation and growth of spheroids on various surfaces

After 6 hours of incubation in the paramagnetic medium in the presence of a magnetic field, the culture medium is changed to remove the Gd-DTPA, as shown in **Figure 4.4**. The structures are then observed for an additional 66 hours, i.e., a total of 72 hours. Cell coalescence by the magnetic field initiates intercellular interactions that form the spheroid, but the 3D structures contract due to the dynamic activity of cadherins, a family of Ca^{+}-dependent transmembrane proteins involved in epithelial cell anchorage [12, 16, 32]. Live/dead staining is performed for the spheroids at 24, 48, and 72 hours (**Figure 4.5**). DAPI (blue) stains all cell nuclei present, while EGFP (green) is specific to dead cells. Overlays of these two images provides references for live (blue) and dead (green) areas. The spheroids, grown for 72 hours, maintain a viable 3D core structure.

A box-and-whisker plot is used to display a non-normal distribution of the measured dimensions for 3D spheroids formed on various surfaces. The 25^{th} percentile (first quartile, Q1), 50^{th} percentile (median), and 75^{th} percentile (third quartile, Q3) are shown as lines of the box from bottom to top, respectively. The interquartile range (IQR) is the difference between the 25^{th} and 75^{th} percentile for each sample population. Upper and lower whiskers are plotted at the 95^{th} and 5^{th} percentile, respectively. Points beyond the range of the

whiskers are plotted as single dots while the mean of each sample is identified by a '+' symbol. For 3D spheroids formed diamagnetically in a flat ULA surface (**Figure 4.5**(**a**)), the IQR ranges from 213,000 μm^2 to 252,000 μm^2 at 6 hours, and reduces to 110,000 μm^2 to 132,000 μm^2 at 24 hours. Mean and median values are similar to one another at 6, 24, 48, and 72 hours, indicating a normal distribution of spheroid dimensions. For 2.5D cell structures formed on TCT surfaces (**Figure 4.5**(**b**)), the IQR ranges from 133,000 μm^2 and 155,000 μm^2 at 6 hours, and 52,500 μm^2 to 69,200 μm^2 at 24 hours. Again, the box-and whisker plot is symmetrical and the median is close to the mean value, indicating a normal distribution of the 3D structure. For self-assembled spheroids on a round ULA surface (**Figure 4.5**(**c**)), the IQR ranges from 266,000 μm^2 to 566,000 μm^2 at 6 hours, and contracts to 125,000 μm^2 to 168,000 μm^2 at 24 hours. Since a symmetrical box-and-whisker plot indicates a normal distribution of data, a non-normal distribution is observed at 6 hours due to the irregularities of spheroid dimensions. Although the final IQR for dimensions of diamagnetically-formed spheroids on a flat ULA surface and a round-bottom ULA surface structures at 72 hours are equivalent (97,700 μm^2 to 119,000 μm^2 and 98,100 μm^2 to 168,000 μm^2, respectively), at 6 hours the sizes of the self-assembled spheroids printed on round-bottom ULA surfaces are larger in comparison to the diamagnetically formed spheroids that are printed on flat ULA surfaces. When a cell suspension is placed on a flat-bottom ULA surface, numerous spheroids are formed in each well, where it is not possible to control either their numbers or dimensions, and hence these are termed as *spontaneously-formed* spheroids. The sizes of the spontaneously-formed spheroids in different wells remain virtually unchanged between 6 and 72 hours (**Figure 4.5**(**d**)), but the size

distributions however decrease. **Figure 4.6** shows the mean projected area measurements of 3D spheroids grown on various surfaces and their respective circularity values, which is summarized in **Table 4.1**. The circularity of the projected areas of magnetically formed spheroids approaches unity, indicating a perfect circle in comparison to that for self-assembled spheroids and spontaneously-formed spheroids which are more irregular.

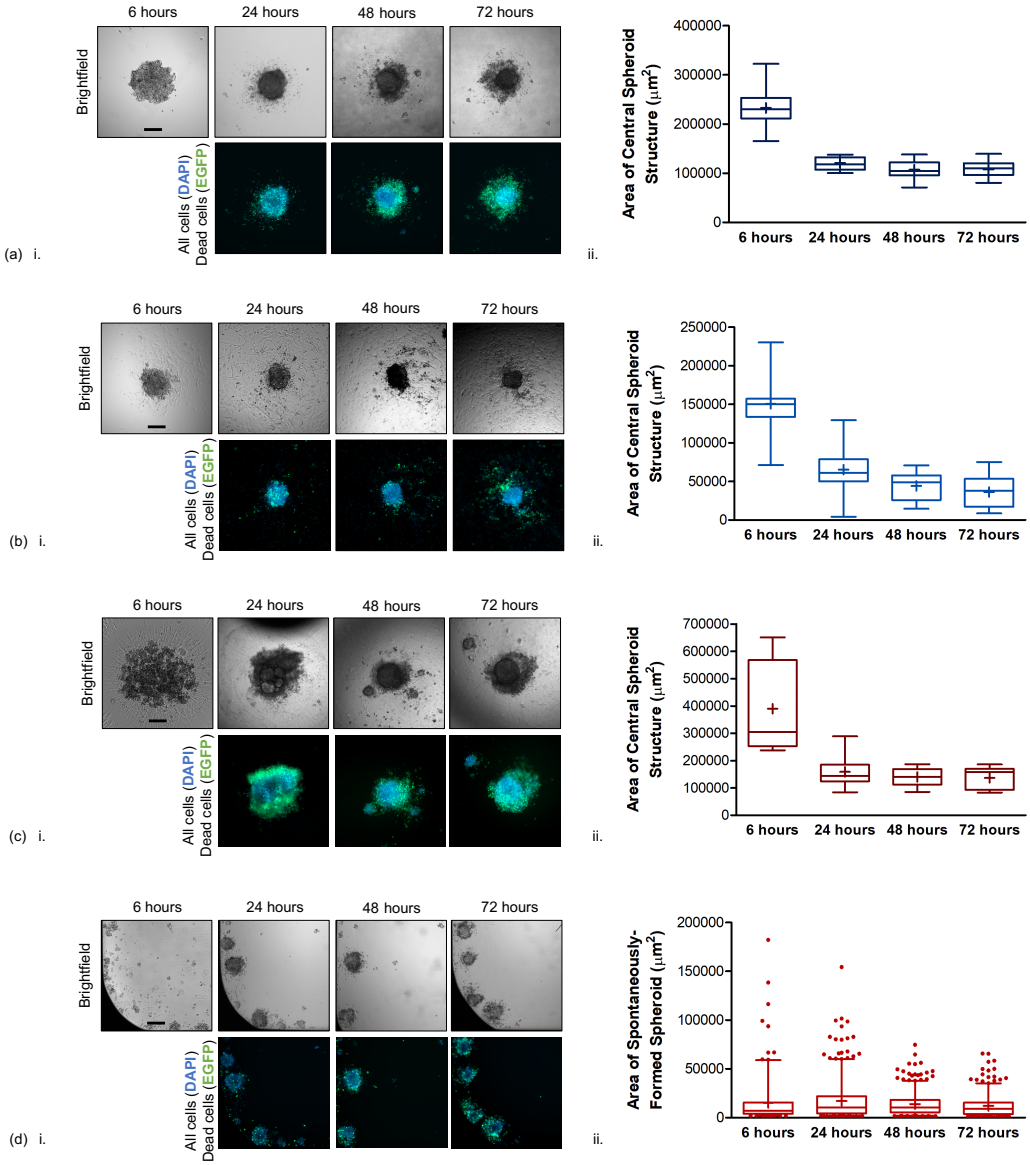

Figure 4.5: Growth and viability of cell structures formed by diamagnetophoresis. Box-and-whisker plots for area measurements of 3D cell structures (n=3) are formed on (**a**) a flat ULA surface (3D) and (**b**) a TCT surface (2.5D), as well as 3D structures using (**c**) round ULA plates that allow the formation of self-assembled spheroids and (**d**) flat ULA plates to allow the formation of numerous spontaneously-formed spheroids per well. Central 3D cell structures were (**i**) imaged and (**ii**) measured at 6 hours (following medium changes to remove Gd-DTPA), 24, 48, and 72 hours. Upper and lower whiskers are placed at the 95th and 5th percentile, respectively. Points beyond the whisker ranges are plotted as single dots. At 6 hours, there is a relatively large variation between the forms of the 3D structures. However, at 6 hours, the level of variation between (**a**) 3D spheroids printed with diamagnetophoresis on a flat ULA surface is much lower than for (**c**) 3D spheroids printed on a round ULA surface. At 24 hours, the projected areas of both samples are equivalent. Scale bar = 200 μm.

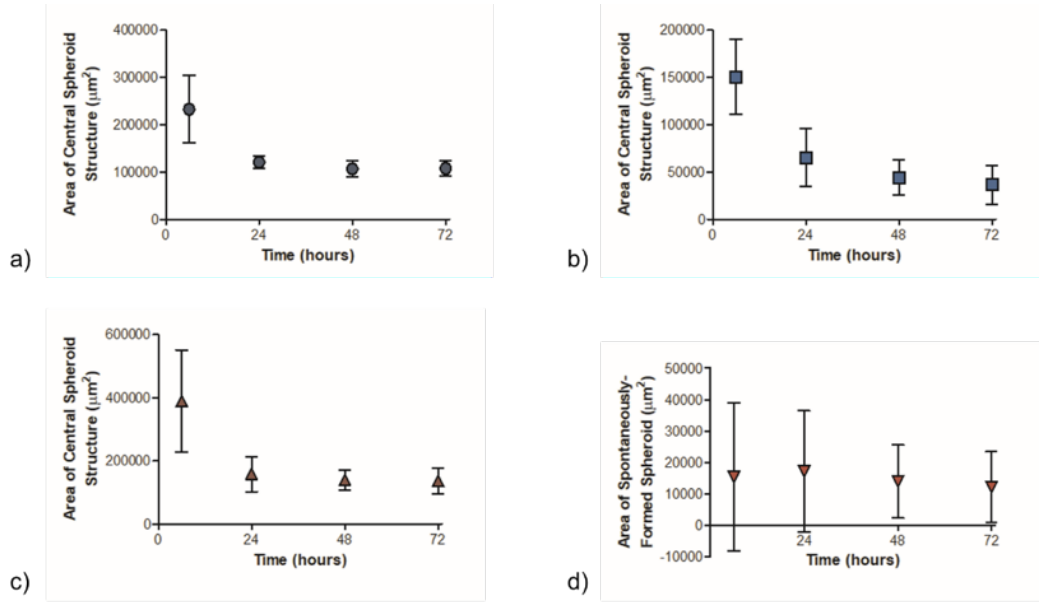

Figure 4.6: Area of 3D spheroids on various surfaces analyzed by SD. (**a**) For magnetically printed spheroids on flat ULA surfaces, their central structures have initial areas of approximately 233,000 ± 71,000 μm^2 at 6 hours, which contract to 121,000 ± 12,800 μm^2 at 24 hours. (**b**) For similarly printed 2.5D structures on TCT surfaces, the 3D central structures have initial areas of approximately 151,000 ± 39,600 μm^2 at 6 hours, which contract to 65,300 ± 30,800 μm^2 at 24 hours. (**c**) When 3D spheroids are self-assembled on round-bottom ULA plates, the central structures have initial areas of approximately 390,000 ± 162,000 μm^2 at 6 hours, which also contract to 159,000 ± 55,700 μm^2 at 24 hours. At 48 and 72 hours, the projected areas of the printed spheroids remain unchanged. (**d**) For spontaneously-formed spheroids, the area distribution is significantly skewed at 6 and 24 hours. The dimensions again remain similar at 48 and 72 hours.

Table 4.1. Area and circularity measurements of 3D structures up to 72 hours.

	3D Cell Structure	**Area of central spheroid structure (mean ± SD μm^2)**	**Circularity (mean ± SD)**
6 hours	3D diamagnetic spheroids	233,000 ± 71,000	0.46 ± 0.15
	2.5D cell structures	158,000 ± 39,600	0.4c ± 0.09
	Self-assembled spheroids	390,000 ± 162,000	0.33 ± 0.13
	Spontaneously-formed spheroids	15,300 ± 23,500	0.50 ± 0.17
24 hours	3D diamagnetic spheroids	121,000 ± 12,800	0.77 ± 0.08
	2.5D cell structures	65,300 ± 30,800	0.75 ± 0.12
	Self-assembled spheroids	159,000 ± 55,700	0.67 ± 0.16
	Spontaneously-formed spheroids	17,100 ± 19,300	0.65 ± 0.14
48 hours	3D diamagnetic spheroids	107,000 ± 17,700	0.86 ± 0.08
	2.5D cell structures	44,300 ± 18,400	0.89 ± 0.03
	Self-assembled spheroids	140,000 ± 31,500	0.72 ± 0.13
	Spontaneously-formed spheroids	13,900 ± 11,700	0.74 ± 0.11
72 hours	3D diamagnetic spheroids	108,000 ± 15,900	0.88 ± 0.06
	2.5D cell structures	36,400 ± 20,800	0.91 ± 0.02
	Self-assembled spheroids	137,000 ± 39,300	0.79 ± 0.07
	Spontaneously-formed spheroids	12,100 ± 11,200	0.79 ± 0.11

4.3.6 Gene expression

Gene analysis is performed with real-time (RT) quantitative polymerase chain reaction (qPCR) to assess the relative stresses for the magnetically printed 3D and 2.5D structures and compared with those for 3D structures produced without a magnetic field and Gd-DTPA. Four samples, (1) 3D diamagnetically printed structures on a flat ULA surface, (2) 2.5D diamagnetically printed structures on a flat TCT surface, (3) 3D self-assembled spheroids on a round-bottom ULA surface, and (4) spontaneously-formed spheroids, are normalized by their fold-change gene expressions relative to control glyceraldehyde 3-phosphate dehydrogenase (*GAPDH*) in 2D cultures grown on a flat TCT surface.

Hypoxia-inducible factor 1-alpha (*HIF1α*) is a general marker of stress for stress caused by hypoxia, or lack of oxygen. Above a critical diameter of roughly 500 μm, aqueous nutrients in the microenvironment and oxygen are unable to penetrate a 3D MCF-7 structure, leading to hypoxic regions and a necrotic core[2, 33-34]. *HIF1α* is typically over-expressed in 3D structures but can also appear in 2D monolayers of highly proliferative cells[35]. Vascular endothelial growth factor (*VEGF*) is an angiogenic factor that is a classic marker for hypoxic stress shown to be correlated with chemoresistance typically observed in 3D cell structures[5]. 3D tumor structures overexpress *VEGF* to induce tumor vascularization, which is characteristic of tumors *in vivo*.

Primer sequences used in the qPCR analysis are described in **Table 4.2**. The gene expressions for *HIF1α* and *VEGF* are shown in **Figure 4.7**. For *HIF1α* gene expression, all cell structures are not observed to be under significant hypoxic stress in comparison to

the normalized expression in 2D monolayers. This is attributed to the small dimensions of the 3D cell structures, which permit sufficient oxygen diffusion and prevent the formation of a hypoxic region. In comparison to the normalized expression in 2D monolayers, no significant changes are observed for *VEGF* expression 3D diamagnetic spheroids, self-assembled spheroids, and spontaneously-formed spheroids. However, 2.5D cell structures overexpress *VEGF* in comparison to 2D monolayers, which can be attributed to the different morphologies observed in the 2.5D cell landscape[27], that suggest the presence of unique gene expressions found in human breast cancers[36].

Table 4.2. Primer sequences used for RT-qPCR analysis.

Gene	Forward Sequence (5'-3')	Reverse Sequence (5'-3')
HIF1α	ATTTTGGCAGCAACGACACA	TGGGTGAGGGGAGCATTACA
VEGF	TCAAGCCATCCTGTGTGCC	CTTGGTGAGGTTTGATCCGC
GAPDH	ATCAAGAAGGTGGTGAAGCAGG	GCGTCAAAGGTGGAGGAGTG

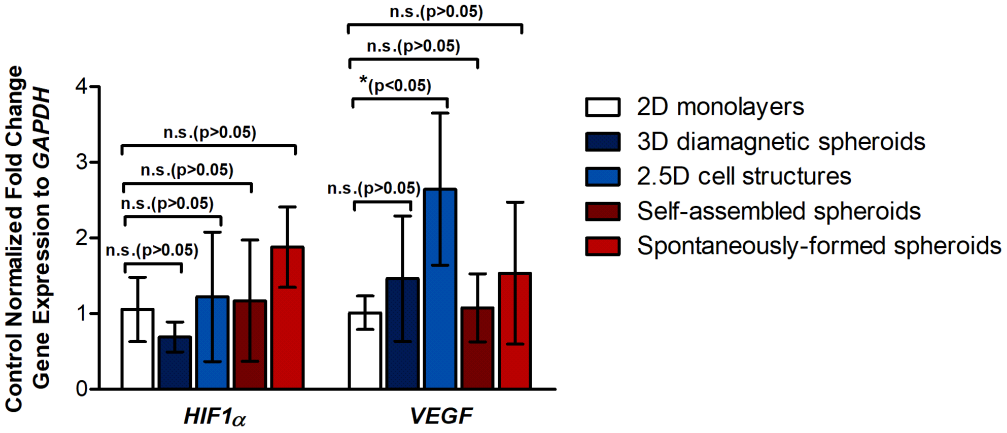

Figure 4.7: Control normalized fold change gene expression to GAPDH. Expression of *HIF1*α is not significant for 3D and 2.5D cell structures in comparison to the normalized expression in 2D monolayers. Expression of *VEGF* is significant only for 2.5D cell structures.

4.4 Discussion

We describe a rapid method to print multidimensional tumors with bioinks containing MCF-7 cells. The resulting cell structures include two types formed through diamagnetophoresis, i.e., 3D spheroids on (1) a ULA plate and (2) a 2.5D lump and spreading monolayer on a TCT surface, as well as three structures formed without magnetic assistance, i.e., (3) 3D spheroids on a round-bottom ULA plate (self-assembled spheroids) (4) 3D spheroids produced on a flat bottom ULA plate (spontaneously-formed spheroids), the counterpart to Case 1, and (5) 2D monolayers grown on a TCT surface, the counterpart to Case 2. The magnetically printed tumors have reproducible geometries that can be varied by adjusting the strength and orientation of the magnetic field external to the wells. These tumors can be printed within 6 hours, more rapidly than self-assembled tumors can be

formed on round-bottom ULA plates. Varying the number of cells changes the spheroid size. Gene expression analysis of printed and self-assembled spheroids, i.e., cells that coalesce without being magnetically manipulated, is indistinguishable, proving that the method is capable of producing viable cell structures in 3D geometries. The actual viability of cells in 3D-printed constructs can be assessed over time by measuring a sample of 3D-printed constructs from a batch made at t_0, at different intervals of time. Measurements include adenosine triphosphate (ATP), projected size, and protein and gene expressions. Gd-DTPA is removed by replacing paramagnetic culture medium with regular, non-paramagnetic culture medium.

MCF-7 cells are among the most-researched human breast cancer cell lines.[37] MCF-7 cells have been reported in numerous studies for the formation of 3D spheroids and mammospheres, making them a suitable candidate for the investigation of magnetic printing of 3D cell structures through diamagnetophoresis. An *in vitro* 3D cell structure composed of human adenocarcinoma cells is relevant for studies of drug response and metastasis. This cancer drug model can be complexed through the addition of stromal cells[38] to mimic the microenvironment of the tumour site, thereby creating a model which can provide greater clinical relevance than a monotypic cell landscape.

It is possible to magnetically print 3D cellular structures using less robust cell lines. It is anticipated that cells with less cell-cell adhesions and/or lower ECM production rate would take longer to form stable 3D cellular assemblies, fibroblast cell lines being the optimal candidate. Despite their clinical relevance, it is expected that primary cells will be more sensitive to Gd, challenging their ability to magnetically 3D printed. More research

and troubleshooting is needed in this area to make magnetic 3D printing a practical approach to all cell types, cell lines, and cells from all origins.

This method is feasible for other cell lines. However, careful consideration of the total exposure to Gd-DTPA (including concentration and incubation time) must be made to optimize the formation of 3D cell structures. The magnetic force on a cell, $\mathbf{F}_m$[26], is described as:

$$\mathbf{F}_m = ((\chi_c - \chi_m)/2\mu_0)V_c \nabla|\mathbf{B}|^2 \quad (4.1)$$

when χ_c and χ_m are the magnetic susceptibilities of the cell and of the fluid culture media, respectively, μ_0 is the permeability of free space, V_c is the cell volume, and $\nabla|\mathbf{B}|^2$ is the magnetic field gradient. For cells of the same size and magnetic susceptibility, their movement of within the medium behaves similarly when the magnetic field gradient is maintained. Therefore, the incubation time required to form a stable 3D cell structure depends on the excretion of extracellular proteins to provide structural support and maintain the integrity of the printed cell structure. Using this method, it is expected that the use of other cell lines will demonstrate accelerated 3D formation, as observed with MCF-7, due to the decreased proximity of cells to one another, which increases the cell-cell contacts to produce ECM proteins.

This system offers a label-free, scaffold-less approach to printing 3D cell structures *in vitro*. However, this system may be limited by the ability to generate sufficient convection within the cell suspension for low cell numbers, using the current setup, to achieve a 3D cell geometry. To circumvent this, the well volume can be decreased to

promote spatial displacement of the cells from the movement of the paramagnetic media towards high magnetic field force. In addition, the number of occupied wells in each plate is limited by the size of the magnets underneath each well which is used to form a single spheroid. Therefore, the use of smaller magnets can be used, only in the case that they are able to induce sufficient magnetic force on the cell suspension.

This technique for magnetic assembly offers a solution to forming reproducibly sized 3D MCF-7 cell structures more rapidly (within 6 hours), compared to those formed by the use of agarose microwells, which require a 24-hour sedimentation period to prevent breaking of the 3D cell structure.[39] In addition, this scaffold-less method does not require additives in culture media, as is seen in hanging drop[40] and liquid overlay[41] techniques. This intentional bioprinting method of cell coalescence has applications to tissue engineering, drug testing, and cell-on-chip devices, thus providing a means to miniaturize simple *in vivo* cell structures for physiologically relevant cell models.

4.5 Materials and methods

4.5.1 Materials and reagents

Dulbecco Modified Eagle's medium (DMEM, Life Technologies, cat# 12800-082) containing 10% fetal bovine serum (FBS, cat# 12484028). Diethylenetriaminepentaacetic acid gadolinium (III) dihydrogen salt hydrate (97%, gadopentatic acid, Gd-DTPA) was purchased from Sigma Aldrich, Canada (cat# 381667). MTT (3-(4,5-dimethylthiazol-2-yl)-2,5-diphenyltetrazolium bromide) reagent was purchased from Invitrogen, Canada (cat# M6494). For cell culture maintenance phosphate buffered saline (PBS, cat# 10010023) and

Trypsin-EDTA (0.25%), phenol red (cat# 25200056) were purchased from Life Technologies, Canada. Dimethyl sulfoxide (DMSO) was purchased from Sigma Aldrich, Canada (cat# D4540). Various cell culture plates were utilized for the preparation of 2D and 3D samples (Corning, Canada): 6-well tissue culture-treated plates for 2D monolayers (ref# 353046); 384-well ultra-low attachment (ULA) plates (cat# 3837) with and without an external magnetic field for the formation of 3D spheroids and spontaneously-formed spheroids, respectively; 96-well tissue culture treated (TCT) plates (ref# 4680) with an external magnetic field for the formation of 2.5D spheroids; and 384-well spheroid microplates (ref# 4516) were used for the formation of self-assembled spheroids. The NdFeB grade N52 magnets were purchased from Zigmyster Magnets, with dimensions of 3×3×3 mm. Other reagents used include: sodium hydroxide (NaOH) (Alfa Aesar, cas# A16037), 2-mercaptoethanol (99%, Sigma Aldrich, Canada), and ethanol (Commercial Alcohols, Canada, cat# P016EAAN).

4.5.2 Characterization methods and instruments

ReadyProbes™ Cell Viability Imaging Kit, Blue/Green (Invitrogen, Canada, cat# R37609) was used to stain spheroid samples for fluorescence imaging. Optical brightfield and fluorescence imaging (enhanced green fluorescent protein (EGFP), and 4',6-diamidino-2-phenylindole (DAPI) nuclei stains) were performed using a Carl Zeiss Axio Observer.Z1 microscope. Excitation and emission wavelengths of 395/509 and 358/461 were used for EGFP and DAPI, respectively. The Tecan Infinite M200 Pro was used for MTT absorbance readings. Size measurements of the central assembled 3D structures was evaluated using

ImageJ. The Dual 48/48W Fast and CFX96 thermal cyclers (BioRad, United States) were used for reverse transcriptase and real time quantitative-PCR, respectively.

4.5.3 Synthesis of paramagnetic Gd-DTPA medium

A stock solution of 150 mM of Gd-DTPA was prepared by mixing 5.47 g of Gd-DTPA in 50 mL of culture medium, and adjusted by adding 17 mL of NaOH to reach an isotonic pH of approximately 7.4±0.2. Contents were constantly mixed on a stir plate as Gd-DTPA and NaOH were added. **Note**: re-adjusting pH of the culture medium following the addition of Gd-DTPA must be done quickly order to preserve the medium's nutritional contents.

4.5.4 MTT assay analysis

MCF-7 cells were trypsinized from a culture plate and allowed to form monolayers containing 1000 cells per well were incubated in 100 μL 0, 1, 10, 25, 50, 75, 100, and 125 mM Gd-DTPA medium in 96-well TCT plates. At 3, 24, 48, and 72 hours, cell proliferation was analyzed by the MTT assay. MTT reagent was diluted in PBS to achieve a final concentration of 5 mg/mL. At each incubation time i.e. 3, 24, 48, and 72 hours, a standard curve was prepared to quantify the unknown number of viable cells present in each incubated sample of Gd-DTPA. 10 μL MTT reagent was added to each well, and left to incubate at standard conditions for 3 hours. Following incubation with MTT reagent, all but 25 μL sample volume was removed from each well. 50 μL DMSO was then added to each well, and the plate left to incubate at standard conditions for 10 minutes. The plate was shaken for 5 seconds, and the absorbance read at 570 nm. For each exposure time,

three biological triplicates (n=3) with six technical triplicates for each Gd-DTPA concentration was performed.

4.5.5 Morphology analysis

To observe effect of Gd-DTPA on cell morphology, 1000 MCF-7 cells were incubated in 0, 1, 10, 25, 50, 75, 100, and 125 mM Gd-DTPA culture medium in 96-well tissue culture-treated and 384-well ULA plates. Plates were incubated under standard conditions. Images were taken at 1, 3, 6, and 24 hours at 40x magnification using optical brightfield microscopy.

4.5.6 Preparation of 3D and 2.5D geometries formed by dimagnetophoresis.

MCF-7 cells were plated in ULA and TCT plates for the preparation of 3D and 2.5D samples, respectively. Cells were suspended in paramagnetic medium under the influence of a magnetic field by arranging a quartet of magnets in N-S-N-S orientation centered directly underneath each well. After cells in the 3D and 2.5D samples have reached maximum accumulation into a single zone of zero magnetic field strength, medium changes were performed in each well using 0 mM Gd-DTPA to dilute concentration of Gd-DTPA to below 1 mM Gd-DTPA.

4.5.7 Effect of Gd-DTPA to form spheroids

1000 MCF-7 cells were plated in a 384-well ULA plate in 1, 1, 10, and 25 mM Gd-DTPA to form 3D geometries as described above. Images were taken at 1, 3, 6, and 24 hours at 5x magnification using phase contrast microscopy. ImageJ was used to analyze changes in

spheroid size. This was repeated in a 96-well TCT plate to form 2.5D geometries. A sample size of n=5 was used for each concentration of Gd-DTPA for both 3D and 2.5D samples. 3D and 2.5D geometries were formed in 80 μL of medium per well.

4.5.8 Effect of incubation period with Gd-DTPA and magnetic field for formation of 3D and 2.5D structures

5000 MCF-7 cells were plated in a 384-well ULA plate in 25 mM Gd-DTPA to form 3D geometries as described above. At 1, 3, 6, and 24 hours, magnets were removed from underneath the samples, and the paramagnetic medium was diluted to approximately 0.4 mM Gd-DTPA. Images were taken at 5x magnification. This was repeated for the formation of 2.5D geometries be seeding 3000 MCF-7 cells in a 96-well TCT plate. A sample size of n=5 was used for each concentration of Gd-DTPA for both 3D and 2.5D samples in biological duplicates. 3D and 2.5D geometries were formed in 80 μL of medium per well.

4.5.9 Preparation of 2D, 3D, and 2.5D samples for gene expression analysis

2D monolayer samples were prepared by seeding 100,000 MCF-7 cells in 0 mM Gd-DTPA (sample control) in a 6-well tissue culture-treated plate, and incubated under standard conditions. 3D spheroids and 2.5D cell structures formed through diamagnetophoresis were formed by seeding 5000 and 3000 MCF-7 cells in a 384-well ULA plate and 96-well TCT plate, respectively, in 80 μL of 25 mM Gd-DTPA medium. After 6 hours of incubation, 25 mM Gd-DTPA was diluted to approximately 0.4 mM following medium changes with 0 mM Gd-DTPA. For self-assembled spheroids, 5000 cells were seeded into a 384-well spheroid microwell plate containing 80 μL of 0 mM Gd-DTPA medium. For

spontaneously-formed spheroids, 5000 cells were seeded in 384-well ULA plate using 80 μL of 0 mM Gd-DTPA medium.

4.5.10 qPCR measurements for gene expression analysis

RNA was extracted from spheroid and monolayer samples using E.N.Z.A.® HP Total RNA Kit (Omega Bio-Tek, United States, cat# R6812) according to the manufacturer's specifications. 1 μg of RNA was reverse transcribed using SuperScript™ IV VILO Master Mix (Invitrogen, Canada, cat# 11756050) for the synthesis of cDNA. The cDNA product was then used for quantitative polymerase chain reaction (qPCR) analysis using PowerUp™ SYBR™ Green Master Mix (Invitrogen, Canada, cat# A25918). PCR protocol was performed as follows: 50.0°C for 2 minutes, 95.0°C for 2 minutes, and 40 cycles of: 95.0°C for 15 seconds, 60.0°C for 15 seconds, 72.0°C for 1 minute. The plate was read at the end of each cycle. Primer sequences were purchased from IDT (Canada). The gene expression of each sample (relative to the expression levels of 2D monolayer samples) was calculated using the delta-delta (ΔΔ) cycle threshold (C_T), $2^{(-\Delta\Delta CT)}$[42], method as follows:

Fold change gene expression = $2^{(-\Delta\Delta CT)}$ when

$$\Delta\Delta C_T = [(\textit{HIF1}\alpha/\textit{VEGF}\ C_T - \textit{GAPDH}\ C_T) \text{ of 2.5D/3D cell structures}]$$

$$- [(\textit{HIF1}\alpha/\textit{VEGF}\ C_T - \textit{GAPDH}\ C_T) \text{ of 2D monolayer}] \quad (4.2)$$

4.5.11 Statistical analysis

MTT semi-quantitative results were analyzed by standard error (n=3). Statistical analysis on the control normalized percent viability was performed using standard error of the mean

(SEM) and a two-way analysis of variance (ANOVA) with Bonferroni post-tests to compare replicate means to Gd-DTPA free media values. Morohology analysis was performed using n=12 for each concentration of Gd-DTPA. The effect of Gd-DTPA to coalesce cells was performed using n=5 for each concentration of Gd-DTPA and results were analyzed by standard deviation. Preparation of 2D, 3D and 2.5D geometries for gene expression analysis was performed by preparing biological triplicates (n=3) of each sample. 3D and 2.5D samples contained a minmum of 45 technical replicates for each biological triplicate. Statistical analysis was performed using SD and a two-way ANOVA with Bonferroni post-tests to compare triplicate means to 2D monolayers. Results were analyzed by standard deviation (SD). 5 samples were from each prepared 3D and 2.5D samples for gene expression analysis were imaged for analysis of size measurements. All statistical analysis was performed using GraphPad Prism software with a 95% confidence interval.

4.6 Acknowledgements

Funding: This work was supported by the Natural Sciences and Engineering Research Council of Canada (NSERC) Discovery Grant [RGPIN-2014-04066], and the NSERC Engage Grant [EGP 513882-17], Canada Foundation for Innovation John R. Evans Leaders Fund (CFI-JELF), the Ontario Research Fund Research Infrastructure [ORF-RI: Grant No. 33016], and the Mitacs Globalink Program and the German Academic Exchange Service (DAAD).

Author contributions: S. Mishriki and A. R. Abdel Fattah contributed equally to this work. The manuscript was written through contributions of all authors. A. R. Abdel

Fattah is now at KU Leuven, Leuven, Belgium in the Department of Mechanical Engineering. All authors have given approval to the final version of the manuscript.

Competing interests: The authors declare that there are no competing financial interests in the regarding the publication of this article. The authors declare that there is no conflict of interest regarding the publication of this article.

4.7 References

1. Phung, Y. T.; Barbone, D.; Broaddus, V. C.; Ho, M., Rapid generation of in vitro multicellular spheroids for the study of monoclonal antibody therapy. *J Cancer* **2011,** *2*, 507-514.

2. Costa, E. C.; Moreira, A. F.; de Melo-Diogo, D.; Gaspar, V. M.; Carvalho, M. P.; Correia, I. J., 3D tumor spheroids: an overview on the tools and techniques used for their analysis. *Biotechnology advances* **2016,** *34* (8), 1427-1441.

3. Sanyal, S., Culture and assay systems used for 3D cell culture. *Corning* **2014,** *9*, 1-18.

4. Bielecka, Z. F.; Maliszewska-Olejniczak, K.; Safir, I. J.; Szczylik, C.; Czarnecka, A. M., Three-dimensional cell culture model utilization in cancer stem cell research. *Biological Reviews* **2017,** *92* (3), 1505-1520.

5. Gong, X.; Lin, C.; Cheng, J.; Su, J.; Zhao, H.; Liu, T.; Wen, X.; Zhao, P., Generation of multicellular tumor spheroids with microwell-based agarose scaffolds for drug testing. *PloS one* **2015,** *10* (6), e0130348.

6. Ivascu, A.; Kubbies, M., Rapid generation of single-tumor spheroids for high-throughput cell function and toxicity analysis. *Journal of biomolecular screening* **2006,** *11* (8), 922-932.

7. Guttilla, I.; Phoenix, K.; Hong, X.; Tirnauer, J.; Claffey, K.; White, B., Prolonged mammosphere culture of MCF-7 cells induces an EMT and repression of the estrogen receptor by microRNAs. *Breast cancer research and treatment* **2012,** *132* (1), 75-85.

8. Mironov, V.; Visconti, R. P.; Kasyanov, V.; Forgacs, G.; Drake, C. J.; Markwald, R. R., Organ printing: tissue spheroids as building blocks. *Biomaterials* **2009,** *30* (12), 2164-2174.

9. Horman, S. R.; To, J.; Orth, A. P.; Slawny, N.; Cuddihy, M. J.; Caracino, D., High-content analysis of three-dimensional tumor spheroids: Investigating signaling pathways using small hairpin RNA. *Nature Methods* **2013,** *10* (10).

10. Amaral, R. L.; Miranda, M.; Marcato, P. D.; Swiech, K., Comparative Analysis of 3D Bladder Tumor Spheroids Obtained by Forced Floating and Hanging Drop Methods for Drug Screening. *Frontiers in physiology* **2017,** *8*, 605.

11. Hong, X.; Chedid, K.; Kalkanis, S. N., Glioblastoma cell line-derived spheres in serum-containing medium versus serum-free medium: A comparison of cancer stem cell properties. *International journal of oncology* **2012,** *41* (5), 1693-1700.

12. Iglesias, J. M.; Beloqui, I.; Garcia-Garcia, F.; Leis, O.; Vazquez-Martin, A.; Eguiara, A.; Cufi, S.; Pavon, A.; Menendez, J. A.; Dopazo, J., Mammosphere formation in breast carcinoma cell lines depends upon expression of E-cadherin. *PloS one* **2013,** *8* (10), e77281.

13. Pedersen, P. H.; Ness, G. O.; Engebraaten, O.; Bjerkvig, R.; Lillehaug, J. R.; Laerum, O. D., Heterogeneous response to the growth factors [EGF, PDGF (bb), TGF-α, BFGF, il-2] on glioma spheroid growth, migration and invasion. *International journal of cancer* **1994,** *56* (2), 255-261.

14. Tannock, I.; Steele, D.; Roberts, J., Influence of reduced concentration of L-glutamine on growth and viability of cells in monolayer, in spheroids, and in experimental tumours. *British journal of cancer* **1986,** *54* (5), 733.

15. Kelm, J. M.; Timmins, N. E.; Brown, C. J.; Fussenegger, M.; Nielsen, L. K., Method for generation of homogeneous multicellular tumor spheroids applicable to a wide variety of cell types. *Biotechnology and bioengineering* **2003,** *83* (2), 173-180.

16. Lin, R. Z.; Chang, H. Y., Recent advances in three-dimensional multicellular spheroid culture for biomedical research. *Biotechnology journal* **2008,** *3* (9-10), 1172-1184.

17. Akiyama, Y.; Morishima, K. In *Label-free ultrarapid spheroid formation in microfluidic chip using magneto-Archimedes effect*, Micro Electro Mechanical Systems (MEMS), 2012 IEEE 25th International Conference on, IEEE: 2012; pp 116-119.

18. Akiyama, Y.; Morishima, K., Label-free cell aggregate formation based on the magneto-Archimedes effect. *Applied Physics Letters* **2011,** *98* (16), 163702.

19. Durmus, N. G.; Tekin, H. C.; Guven, S.; Sridhar, K.; Yildiz, A. A.; Calibasi, G.; Ghiran, I.; Davis, R. W.; Steinmetz, L. M.; Demirci, U., Magnetic levitation of single cells. *Proceedings of the National Academy of Sciences* **2015,** *112* (28), E3661-E3668.

20. Anil-Inevi, M.; Yaman, S.; Yildiz, A. A.; Mese, G.; Yalcin-Ozuysal, O.; Tekin, H. C.; Ozcivici, E., Biofabrication of in situ Self Assembled 3D Cell Cultures in a Weightlessness Environment Generated using Magnetic Levitation. *Scientific reports* **2018,** *8* (1), 7239.

21. Türker, E.; Demirçak, N.; Arslan-Yildiz, A., Scaffold-free three-dimensional cell culturing using magnetic levitation. *Biomaterials Science* **2018**.

22. Turker, E.; Arslan-Yildiz, A., Recent Advances in Magnetic Levitation: A Biological Approach from Diagnostics to Tissue Engineering. *ACS Biomaterials Science & Engineering* **2018,** *4* (3), 787-799.

23. Bhise, N. S.; Manoharan, V.; Massa, S.; Tamayol, A.; Ghaderi, M.; Miscuglio, M.; Lang, Q.; Zhang, Y. S.; Shin, S. R.; Calzone, G., A liver-on-a-chip platform with bioprinted hepatic spheroids. *Biofabrication* **2016,** *8* (1), 014101.

24. Frenea-Robin, M.; Chetouani, H.; Haddour, N.; Rostaing, H.; Laforet, J.; Reyne, G. In *Contactless diamagnetic trapping of living cells onto a micromagnet array*, Engineering in Medicine and Biology Society, 2008. EMBS 2008. 30th Annual International Conference of the IEEE, IEEE: 2008; pp 3360-3363.

25. Winkleman, A.; Gudiksen, K. L.; Ryan, D.; Whitesides, G. M.; Greenfield, D.; Prentiss, M., A magnetic trap for living cells suspended in a paramagnetic buffer. *Applied physics letters* **2004,** *85* (12), 2411-2413.

26. Abdel Fattah, A. R.; Meleca, E.; Mishriki, S.; Lelic, A.; Geng, F.; Sahu, R. P.; Ghosh, S.; Puri, I. K., In Situ 3D Label-Free Contactless Bioprinting of Cells Through Diamagnetophoresis. *ACS Biomaterials Science & Engineering* **2016**.

27. Fattah, A. R. A.; Mishriki, S.; Kammann, T.; Sahu, R. P.; Geng, F.; Puri, I. K., 3D cellular structures and co-cultures formed through the contactless magnetic manipulation of cells on adherent surfaces. *Biomaterials science* **2018,** *6* (3), 683-694.

28. Fattah, A. R. A.; Mishriki, S.; Kammann, T.; Sahu, R. P.; Geng, F.; Puri, I. K., Gadopentatic acid affects in vitro proliferation and doxorubicin response in human breast adenocarcinoma cells. *BioMetals* **2018**, 1-12.

29. Kuo, C.-T.; Liu, H.-K.; Huang, G.-S.; Chang, C.-H.; Chen, C.-L.; Chen, K.-C.; Huang, R. Y.-J.; Lin, C.-H.; Lee, H.; Huang, C.-S., A spatiotemporally defined in vitro microenvironment for controllable signal delivery and drug screening. *Analyst* **2014,** *139* (19), 4846-4854.

30. Sundarakrishnan, A.; Chen, Y.; Black, L. D.; Aldridge, B. B.; Kaplan, D. L., Engineered cell and tissue models of pulmonary fibrosis. *Advanced drug delivery reviews* **2017**.

31. Akiyama, Y.; Morishima, K. In *Spheroid array formation by non-label cell manipulation using magneto-Archimedes effect*, Micro-NanoMechatronics and Human Science (MHS), 2011 International Symposium on, IEEE: 2011; pp 45-50.

32. Lin, R.-Z.; Chou, L.-F.; Chien, C.-C. M.; Chang, H.-Y., Dynamic analysis of hepatoma spheroid formation: roles of E-cadherin and β1-integrin. *Cell and tissue research* **2006,** *324* (3), 411-422.

33. Däster, S.; Amatruda, N.; Calabrese, D.; Ivanek, R.; Turrini, E.; Droeser, R. A.; Zajac, P.; Fimognari, C.; Spagnoli, G. C.; Iezzi, G., Induction of hypoxia and necrosis in multicellular tumor spheroids is associated with resistance to chemotherapy treatment. *Oncotarget* **2017,** *8* (1), 1725.

34. Groebe, K.; Mueller-Klieser, W., On the relation between size of necrosis and diameter of tumor spheroids. *International Journal of Radiation Oncology* Biology* Physics* **1996,** *34* (2), 395-401.

35. Aschauer, L.; Gruber, L. N.; Pfaller, W.; Limonciel, A.; Athersuch, T. J.; Cavill, R.; Khan, A.; Gstraunthaler, G.; Grillari, J.; Grillari, R., Delineation of the key aspects in the regulation of epithelial monolayer formation. *Molecular and cellular biology* **2013,** *33* (13), 2535-2550.

36. Kenny, P. A.; Lee, G. Y.; Myers, C. A.; Neve, R. M.; Semeiks, J. R.; Spellman, P. T.; Lorenz, K.; Lee, E. H.; Barcellos-Hoff, M. H.; Petersen, O. W., The morphologies of breast cancer cell lines in three‐dimensional assays correlate with their profiles of gene expression. *Molecular oncology* **2007,** *1* (1), 84-96.

37. Lacroix, M.; Leclercq, G., Relevance of breast cancer cell lines as models for breast tumours: an update. *Breast cancer research and treatment* **2004,** *83* (3), 249-289.

38. Studebaker, A. W.; Storci, G.; Werbeck, J. L.; Sansone, P.; Sasser, A. K.; Tavolari, S.; Huang, T.; Chan, M. W.; Marini, F. C.; Rosol, T. J., Fibroblasts isolated from common sites of breast cancer metastasis enhance cancer cell growth rates and invasiveness in an interleukin-6–dependent manner. *Cancer research* **2008,** *68* (21), 9087-9095.

39. Zhang, W.; Li, C.; Baguley, B. C.; Zhou, F.; Zhou, W.; Shaw, J. P.; Wang, Z.; Wu, Z.; Liu, J., Optimization of the formation of embedded multicellular spheroids of MCF-7 cells: How to reliably produce a biomimetic 3D model. *Analytical biochemistry* **2016,** *515*, 47-54.

40. Kuo, C.-T.; Wang, J.-Y.; Lin, Y.-F.; Wo, A. M.; Chen, B. P.; Lee, H., Three-dimensional spheroid culture targeting versatile tissue bioassays using a PDMS-based hanging drop array. *Scientific Reports* **2017,** *7* (1), 4363.

41. Froehlich, K.; Haeger, J.-D.; Heger, J.; Pastuschek, J.; Photini, S. M.; Yan, Y.; Lupp, A.; Pfarrer, C.; Mrowka, R.; Schleußner, E., Generation of multicellular breast cancer tumor spheroids: Comparison of different protocols. *Journal of mammary gland biology and neoplasia* **2016,** *21* (3-4), 89-98.

42. Livak, K. J.; Schmittgen, T. D., Analysis of relative gene expression data using real-time quantitative PCR and the 2− ΔΔCT method. *methods* **2001,** *25* (4), 402-408.

5 Fibroblasts accelerate formation and improve reproducibility of 3D cellular structures printed with magnetic assistance

This chapter is reproduced from *Fibroblasts accelerate formation and improve reproducibility of 3D cellular structures printed with magnetic assistance, 2020, Research,* ***Sarah Mishriki****, Srivatsa Aithal, Tamaghna Gupta, Rakesh P. Sahu, Fei Geng, and Ishwar K. Puri, https://doi.org/10.34133/2020/3970530.* The author of this thesis is the main contributor of this publication.

5.1 Abstract

Fibroblasts (mouse, NIH/3T3) are combined with MDA-MB-231 cells to accelerate the formation and improve the reproducibility of 3D cellular structures printed with magnetic assistance. Fibroblasts and MDA-MB-231 cells are co-cultured to produce 12.5:87.5, 25:75 and 50:50 total population mixtures. These mixtures are suspended in a cell medium containing a paramagnetic salt, Gd-DTPA, which increases the magnetic susceptibility of the medium with respect to the cells. A 3D monotypic MDA-MB-231 cellular structure is printed within 24 hours with magnetic assistance, whereas it takes 48 hours to form a similar structure through gravitational settling alone. The maximum projected areas and circularities, and cellular ATP levels of the printed structures are measured for 336 hours. Increasing the relative amounts of the fibroblasts mixed with the MDA-MB-231 cells decreases the time taken to form the structures and improves their reproducibility. Structures produced through gravitational settling have larger maximum projected areas, but their cellular ATP and are deemed less reproducible. The distribution of individual cell

lines in the co-cultured 3D cellular structures shows that printing with magnetic assistance yields 3D cellular structures that resemble *in vivo* tumors more closely than those formed through gravitational settling. The results validate our hypothesis that (1) fibroblasts act as 'glue' that support the formation of 3D cellular structures, and (2) the structures are produced more rapidly and with greater reproducibility with magnetically assisted printing than through gravitational settling alone. Printing of 3D cellular structures with magnetic assistance has applications relevant to drug discovery, lab-on-chip devices and tissue engineering.

5.2 Introduction

Three-dimensional (3D) cellular structures representing tumor models provide more physiologically relevant research data than from two-dimensional (2D) cell cultures. These 3D models exploit *in vivo* cellular phenomena such as cell-cell interactions, cell polarization, increased drug resistance, diffusion gradients of O_2, CO_2, nutrients, and metabolites that lead to proliferative, quiescent and necrotic regions, and similar gene expressions,[1-3] which are unattainable and therefore not observed in 2D cell models. MDA-MB-231, a human epithelial triple-negative metastatic breast cancer cell line, is notorious for being difficult to grow in 3D.[4-5] Efforts to form 3D cellular structures with MDA-MB-231 often incorporate biologically-based extracellular matrix (ECM) constituents, such as recombinant basement membrane (rBM)[1] or Matrigel[6-8].

MDA-MB-231 lacks adequate capacity to form a stable structure. These cells display stellate morphologies when grown in 3D in the presence of an extracellular matrix,

indicating a malignant phenotype.[9-10] Matrigel, which promotes intercellular interactions for cell agglomeration[7], is derived from mouse Englebreth-Holm-Swarm tumor[11] and contains a mixture of ECM proteins and growth factors[7, 11]. It is used in numerous scaffold-based 3D culture models.[12-14] However, the batch-to-batch variability of endogenous components and uncontrolled matrix constituents[15-17] in Matrigel limits the reproducibility of the structures that are formed. In addition, it does not appropriately represent a human microenvironment due to its murine-derived origin.[8, 17-18] The use of cell adhesive ECM components as additives can also be used. Fibronectin, an important ECM ligand, is studied as a facilitator of metastasis[19] and up-regulation of pro-matrixmetalloprotease-9, important for angiogenesis and metastatic nodules[20] in breast cancers. Regulating the formation of these 3D cellular structures is critical for a drug discovery process.[7, 16, 21-22]

The use of scaffold-free aggregations of tumor cells are an appropriate model for cancer research.[2] Adherent or anchorage-dependent cells cultured on an ultra-low attachment (ULA) surface undergo spontaneous agglomeration, referred to as the *forced floating*[23] or *liquid overlay technique*[7]. On a flat ULA surface, this forced floating results in the formation of numerous 3D cellular structures of variable dimensions[24], limiting the reproducibility of the desired 3D model. In a geometric-bottom well plate, cells are able to aggregate in numerous cavities and form 3D cell spheres (spheroids) with greater uniformity.[3] Although a high throughput is achieved in both cases, the isolation of these single 3D cellular structures poses difficulty. Alternatively, the use of a round-bottom ULA surface facilitates the formation of a single 3D cell structure in each well.[25] Here, only gravity is active in the formation of these structures. It follows that an externally applied

force could concentrate the cells into a denser area and form a single 3D cellular structure on a flat ULA surface.

Magnetic printing is an engineering solution to create reproducible 3D cellular structures that can be used for *in vitro* cellular studies. [26-29] Here, using a unique bottom-up approach, 3D cellular assemblies can be formed by exploiting the magnetic properties of cells. Most mammalian cells are diamagnetic[30], i.e., they exhibit a repulsive magnetic force when in the presence of a magnetic field. This is also true of their culture medium, which is an aqueous solution of proteins, sugars, and nutrients to maintain their growth.

With the addition of a paramagnetic salt, such as gadopentatic acid (Gd-DTPA), the culture medium becomes paramagnetic. Within the appropriate exposure limits, Gd-DTPA (a magnetic resonance imaging (MRI) contrast agent (CA)) is potentially non-toxic. The addition of Gd-DTPA establishes a magnetic susceptibility difference between the diamagnetic cells and their surrounding paramagnetic liquid media, and has been shown to effectively facilitate the displacement of cells in the presence of a magnetic field. [26-27, 29] In an inhomogeneous magnetic field, the suspended cells are displaced towards regions of lowest magnetic field strength to form a single 3D cellular cluster in a contactless, label-free manner within hours (**Figure 5.1** and **Video 5.1**). We have previously demonstrated the rapid and highly reproducible formation of 3D MCF-7 cellular structures using this technique.[26]

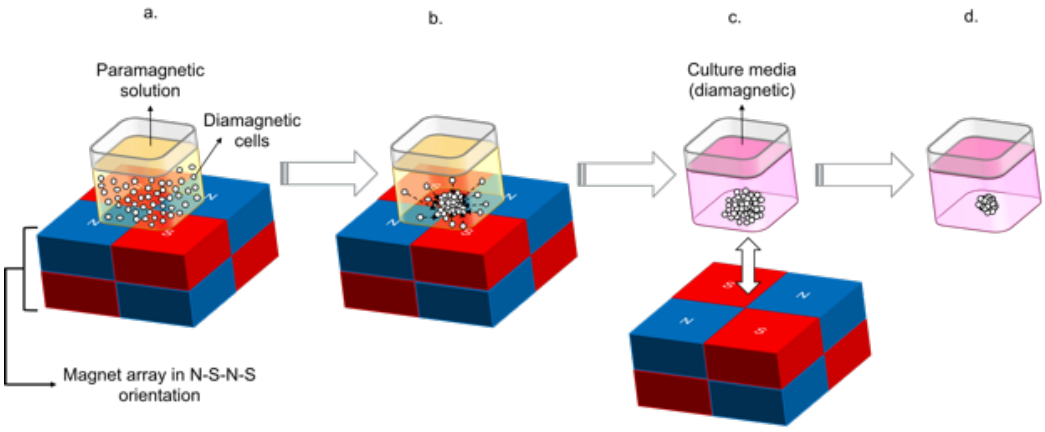

Figure 5.1: Schematic illustration of the magnetically-assisted printing of 3D cellular structures. (**a**) Printing 3D cellular structures with magnetic assistance requires (1) a homogeneous suspension of cells in a liquid medium, (2) a magnetic susceptibility difference between the cells (diamagnetic) and the medium (paramagnetic), and (3) an applied inhomogeneous magnetic field. This is produced by a quartet of magnets in North-South-North-South (N-S-N-S) orientation. At the intersection of this quartet there is a region of low magnetic field gradient. A physical well that is part of a standard 384- or 96- well plate is placed directly above this region. (**b**) The diamagnetic cells are displaced towards the center of the well. (**c**) After all cells have assembled in the center of the well and have had sufficient intercellular interactions to stabilize the cell agglomerate, the paramagnetic solution is replaced with regular culture media, and the magnetic field is removed. (**d**) The 3D cellular structure contracts as a result of continued intercellular interactions.

In vivo, tumors may be composed of up to 80% stromal cells which include fibroblasts, adipose, endothelial and inflammatory cells, as well as a cocktail of different growth factors

and enzymes.[8] Since the tumor microenvironment (TME) *in vivo* is highly regulated by the presence of stromal [31-33], soluble factors[34] and ECM[35], an alternative to the addition of Matrigel or collagen is the co-culture with fibroblasts[5, 8].

Fibroblasts are the most predominant cell type of connective tissue found in animals, and actively produce and remodel the ECM. .[8, 32, 36] In addition, it has been shown that activity of cancer-associated fibroblasts (CAFs)[37] or resident fibroblasts present in a TME[38] stiffen the TME containing tumor cells through the crosslinking of collagen, one of the most predominant proteins in ECM[39]. This results in the increase in fibroblast contraction and the number of focal adhesions[37], which are the interactions that anchors cells to ECM. Formation of a scaffold-free co-culture tumor model also eliminates the need to employ laborious extraction techniques from a matrix, which are necessary for further downstream analyses.[40] Fibroblasts have been used in previous studies to model the influence of stromal cells in a malignant tumor model[4, 8, 31, 41], and for conditioning culture medium to observe an increase of invasiveness[34] or motility[42] of breast cancer cell lines *in vitro*.

Since fibroblasts in a co-culture have been shown to restore the formation of 3D cellular structures in comparison to 3D cellular structures formed from monotypic cell populations31, the introduction of fibroblasts is expected to also accelerate the formation of a 3D cellular structure. We hypothesize that through secretion of their ECM components and contraction of the 3D cellular structure (1) fibroblasts act as 'glue' that support the formation of 3D cellular structures, and (2) these structures are produced more rapidly and with higher reproducibility with magnetically assisted printing than through gravitational settling alone.

The effect of fibroblasts on the formation of 3D cellular structures of MDA-MB-231 cells is investigated for structures printed with magnetic assistance and through gravitational settling alone. An embryonic mouse fibroblast cell line, NIH/3T3, is mixed in various proportions into a population of MDA-MB-231 cells. The 3D cellular structures are printed with magnetic assistance on flat-bottom and those through gravitational settling on round-bottom ULA surfaces.

Initial experiments are performed to establish the exposure limits of Gd-DTPA to monotypic and co-culture populations of MDA-MB-231 and fibroblast cells. Once the formation time is established, the maximum projected area, circularity of the 3D cellular structure, as well as cellular ATP are measured for 336 hours. These measurements provide insight into the use of Gd-DTPA as a reliable paramagnetic agent, independent of its effect on the formation of 3D cellular structures via magnetic assistance. Confocal imaging is used to visualize the self-assembling distribution of the individual cell lines at 3, 7 and 14 days post-formation.

5.3 Results

5.3.1 Presence of Gd^{3+} in monotypic 3D cellular structures to assess the susceptibility of 3D cellular structures to Gd-DTPA

As previously demonstrated, the printing of 3D cellular structures with magnetic assistance is facilitated by adding 25 mM Gd-DTPA to the cell culture medium.[26-28] During the formation of a 3D MCF-7 cellular structure, the limiting exposure time to Gd-DTPA was established by evaluating the relative changes in cell viability. Subsequently, the minimum

time required to form a 3D cellular structure was determined. Cell viability was not significantly affected by exposure to 25 mM Gd-DTPA for 24 hours. The 3D structure was printed within 6 hours for specific conditions that include seeding cell density, magnet dimension, and well size. [26]

Different cell lines, however, may have varying susceptibilities to different concentrations and chelates of Gd^{3+} ions that can have a toxic effect[43], which may also interfere with native intercellular interactions. Gd-DTPA has a short biological half-life of approximately 30 minutes.[44] When Gd^{3+} ions separate from its chelate, they pose a toxic threat through accumulation, e.g., in organ tissues.[44]

To understand the influence of Gd-DTPA during the magnetically-assisted printing of 3D cellular structures, the concentrations of Gd^{3+} ions within the 3D cellular assemblies during short-term incubation periods must first be measured. Retention of Gd-based MRI CAs are of particular interest to the radiology community since the realization of physiological complications following intravenous administration, such as nephrogenic systemic fibrosis (NSF).[45-46]

ICP-MS, a mass spectroscopy technique, is used to quantify the Gd^{3+} ions present in monotypic 3D cellular structures (MDA-MB-231 and fibroblast) printed with magnetic assistance (**Figure 5.2**). The 3D cellular structures printed with magnetic assistance are exposed to 25 mM Gd-DTPA in the presence of a magnetic field for 24 hours. Other 3D structures formed through gravitational settling, which do not require a paramagnetic

medium or a magnetic field, are used as a control. These latter structures are therefore expected to have no Gd^{3+} ions present.

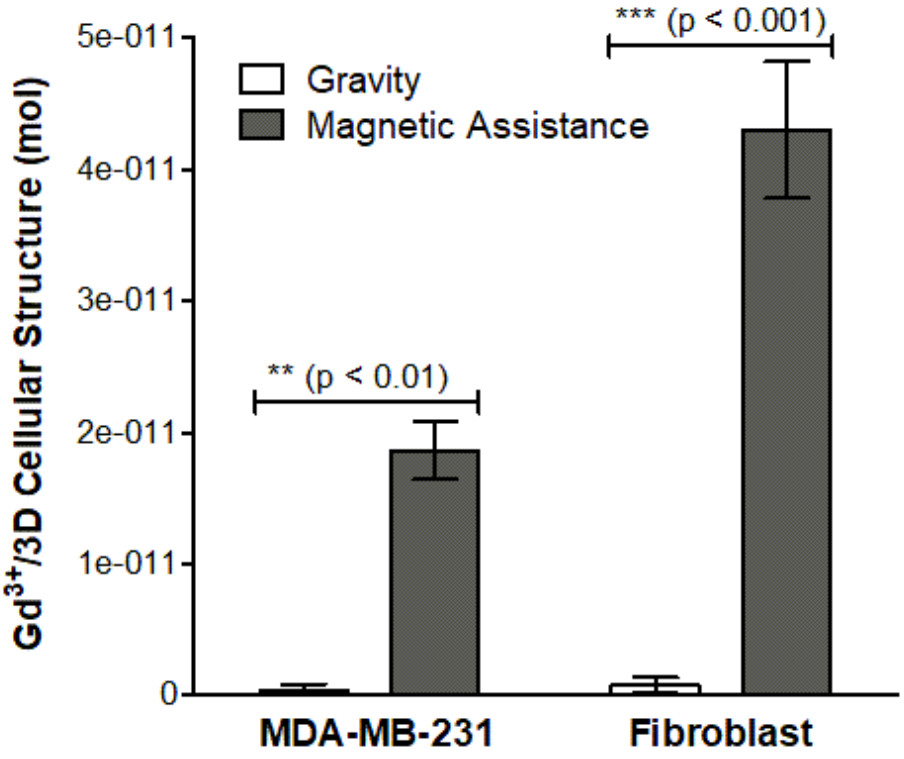

Figure 5.2: Presence of Gd3+ during formation of 3D cellular structures via magnetic assistance. The presence of Gd^{3+} ions within 3D cellular structures printed with magnetic assistance is observed in the two cell lines. A higher Gd^{3+} concentration is observed in 3D fibroblast structures (***) than in the MDA-MB-231 structures (**), as compared to their control samples formed through gravitational settling. Trace amounts of Gd^{3+} present in the control samples are attributed to instrument measurement sensitivity.

As shown in **Figure 5.2**, Gd^{3+} ions are present in 3D MDA-MB-231 or fibroblast cellular structures printed with magnetic assistance. Higher amounts of Gd^{3+} ions are present in fibroblast 3D structures ($4.3 \pm 0.9 \times 10^{-11}$ mol/3D structure) than those composed of MDA-MB-231 cells ($1.9 \pm 0.4 \times 10^{-11}$ mol/3D structure). Trace amounts of Gd^{3+} ions are also found in the 3D structures formed through gravitational settling for both MDA-MB-231 and fibroblast cells (4.4 ± 7.7 and $7.8 \pm 9.8 \times 10^{-13}$ mol/3D structure, respectively), but these amounts are close to the measurement limit of the instrument and thus considered insignificant.

Possible sources of Gd^{3+} retention in the 3D structures are entrapment within the ECM or cellular uptake. The internalization of Gd^{3+} ions in *in vivo* tissue and *in vitro* cellular structures can occur through diffusion[46] through the displacement of ions due to similarities of atomic radius size and competitive binding, such as in bone by replacing Ca^{2+} in hydroxyapatite[45].

Retention of Gd^{3+} has not been reported for breast cancer tissue composed of MDA-MB-231 cells, but its retention in kidney tissue has been measured to be 2.05 ± 0.17 ppm (~1.3×10^{-9} mol) two weeks following administration of clinically relevant dosages of Gd-DTPA.[42] The organ- or cell-specific toxicity of these levels of Gd^{3+} is unknown. In the future, to determine the subcellular presence of Gd^{3+} within the structures, scanning electron microscopy energy-dispersive X-ray spectroscopy (SEM-EDS) [44] The organ- or cell-specific toxicity of these levels of Gd^{3+} is unknown. In the future, to determine the subcellular presence of Gd^{3+} within the structures, scanning electron microscopy (SEM)

energy-dispersive X-ray spectroscopy (EDS)[47] or synchrotron radiation scanning transmission X-ray microscopy (SR-STXM)[48]. Resolution limits of these techniques are 2 μm and 10-30 nm, respectively. Alternatively, administration of a specifically membrane-permeable Gd-based CA detected by ICP-MS[49] may be used.

5.3.2 Effect of Gd-DTPA on cell viability in 2D monotypic and co-culture populations

The effect of Gd-DTPA on cell viability is evaluated on 2D monotypic and co-culture populations using an MTT assay (**Figure 5.3**), which measures metabolic activity, an indication of cell viability. The co-culture populations consist of 12.5, 25 and 50% fibroblasts. Exposure to higher Gd-DTPA concentrations over longer durations should be more toxic to cells than to lower concentrations, shorter exposure times, or a combination of the two.

Our previous investigations found exposure to 25 mM for 24 hours to be non-toxic to MCF-7 cells.[26-27] Therefore, we continue to investigate the short-term cell viability of MDA-MB-231, fibroblast and co-culture populations at 25 mM Gd-DTPA for two incubation times. Each population is exposed to that concentration for 3 and 24 hours and the cell viability is normalized to the corresponding Gd-DTPA-free (0 mM) control population. At 3 hours, none of the populations exhibit significant changes in cell viability. At 24 hours, while the monotypic MDA-MB-231 (**Figure 5.3**(**a**)) and co-culture populations (**Figure 5.3**(**b-d**)) exhibit nonsignificant changes in cell viability, the monotypic fibroblast populations (**Figure 5.3**(**e**)) display a significant decrease.

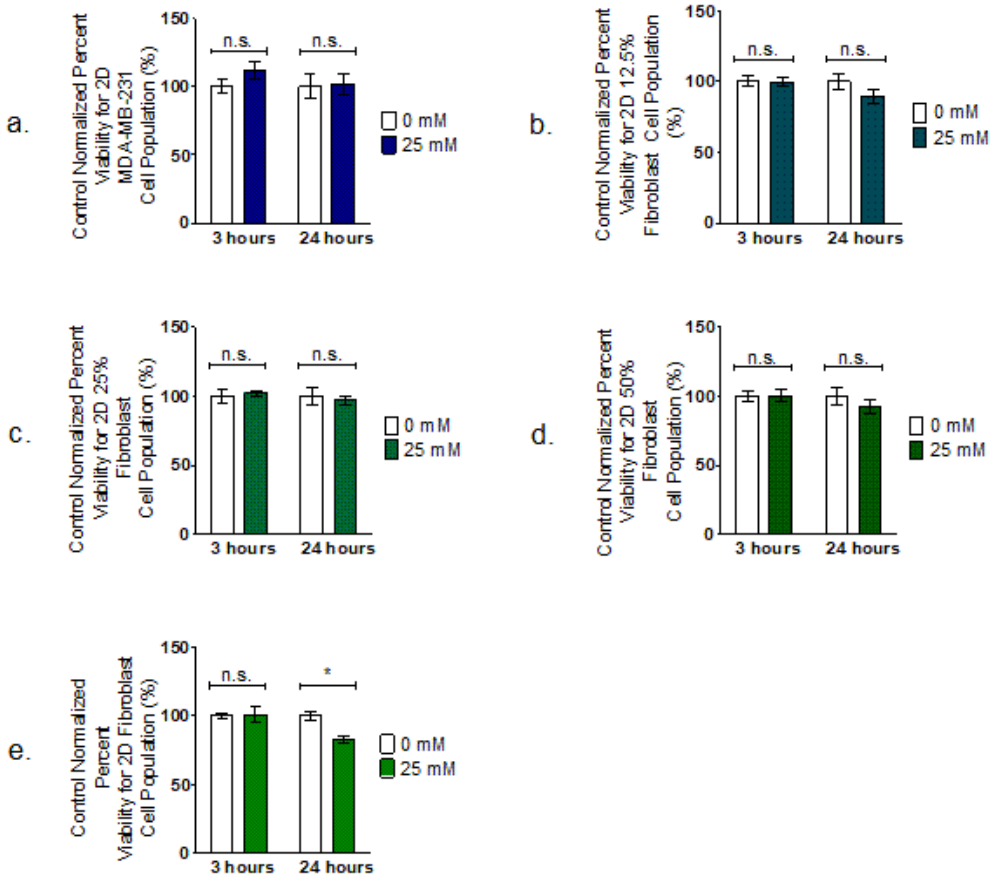

Figure 5.3: Control normalized percent viability. 2D cell populations of monotypic MDA-MB-231, fibroblast, and co-culture populations are exposed to 25 mM Gd-DTPA for 3 and 24 hours. A 25 mM Gd-DTPA concentration does not influence the cell viability of (**a**) monotypic MDA-MB-231 and co-culture cell populations composed of (**b**) 12.5%, (**c**) 25% and (**d**) 50% fibroblast cells at 3 and 24 hours, and (**e**) monotypic fibroblast cell populations at 3 hours. However, at 24 hours of exposure to 25 mM Gd-DTPA the control percent viability for monotypic fibroblast cell populations decreases (*).

This reduced viability of fibroblast cells agrees with the ICP-MS measurements that show increased susceptibility of fibroblast cells to Gd^{3+} ions, the presence of which is likely related to toxicity and thus affects cell viability. The reduced susceptibility of the monotypic MDA-MB-231 cell populations may be due to their inherent resistance to the salt. This may also be the case for co-cultures where the resistance of the MDA-MB-231 cell population or its proportion overcomes the susceptibility of fibroblasts or their reduced metabolic inactivity in the presence of Gd-DTPA. The interaction between the two cell lines may also increase their overall resistance[31] towards Gd-DTPA.

Based on these results, to limit potential toxic effects of Gd-DTPA, the monotypic MDA-MB-231 and co-culture cell populations are exposed to 25 mM Gd-DTPA for a maximum of 24 hours. However, fibroblasts are only exposed to 25 mM Gd-DTPA for a maximum of 3 hours.

5.3.3 Formation of monotypic and co-culture 3D cellular structures to assess the influence of cellular composition and method of formation

Printing 3D cellular structures with magnetic assistance require (1) a suspension of cells in a liquid medium, (2) a magnetic susceptibility difference between the cells (diamagnetic) and the medium (paramagnetic) and (3) an applied inhomogeneous magnetic field. After the 3D structures are printed, the magnetic field can be removed and the paramagnetic medium replaced with a usual cell medium. [26] However, if the paramagnetic cell medium is replaced with a Gd-free cell medium prior to sufficient intercellular interactions

occurring, the cell agglomerate is readily disturbed and the morphology of the resulting 3D structure distorted. This can lead to the formation of numerous 3D daughter structures.

A 3D cellular structure is considered established when it contains cellular interactions[7] or retains its morphology following transfer into another well[50]. Hence, we compare the morphologies of the 3D structures before and after physical disturbances to the culture well in the form of cell medium washes (**Figure 5.4**), which are performed to remove Gd-DTPA. Here, formation is considered successful when a single 3D cellular structure is present following these necessary washes.

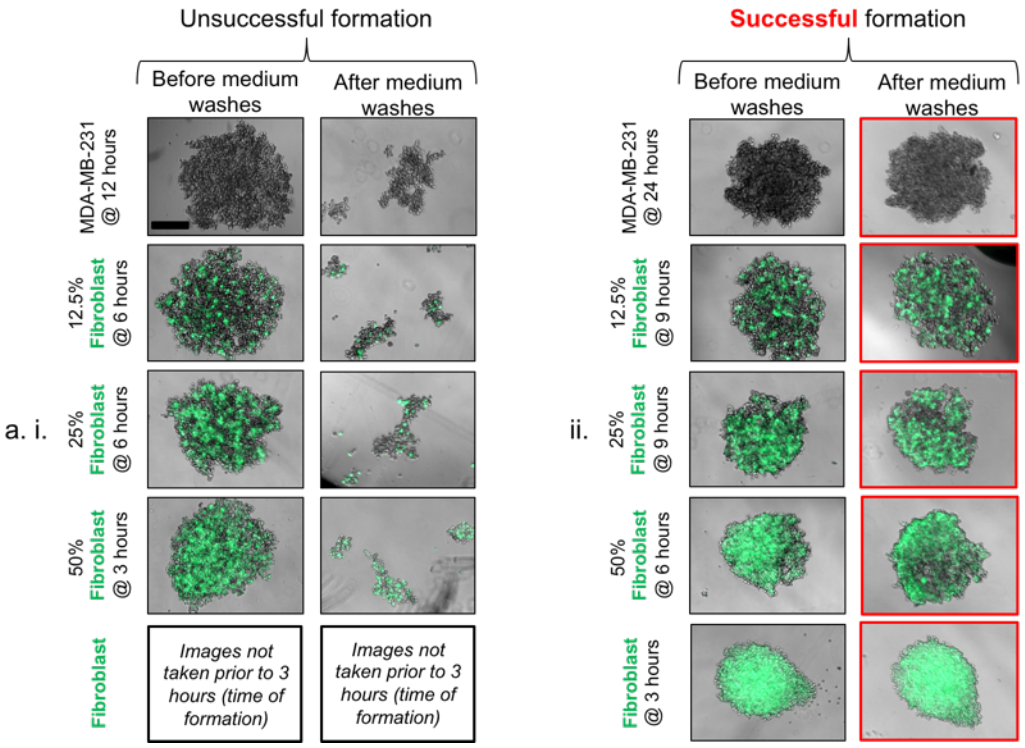

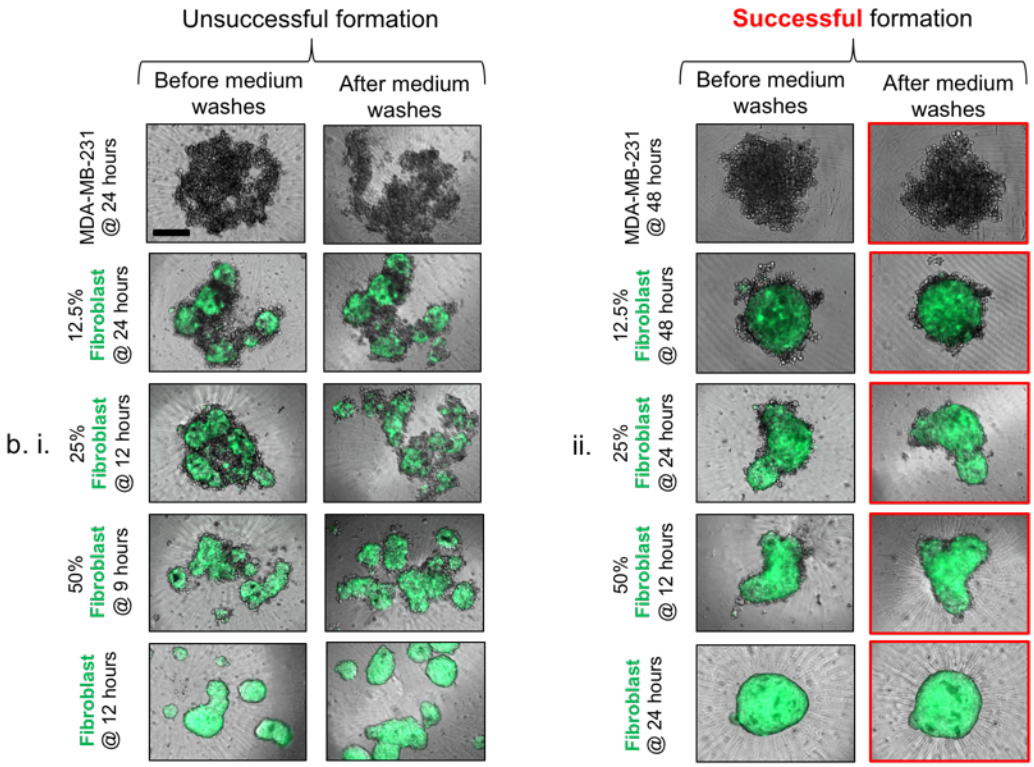

Figure 5.4: Morphology of 3D cellular structures. (**a**) Printed with magnetic assistance and (**b**) formed through gravitational settling before and after washes with the medium to remove Gd-DTPA and prevent overexposure to its ions. Cells require time to form a 3D cellular structure that will cohere. Prior to this coherence, (**i**) cells still form single 3D cellular structures but this disintegrates during washing, which disturbs their morphology. After the structure coheres, (**ii**) changes in the medium by washing are unable to overcome intercellular interactions and disturb the single 3D cellular structures. The scale bar is equal to 100 μm.

A summary of successful productions (%) of 3D cellular structures printed with magnetic assistance and formed through gravitational settling alone is provided in **Table 5.1** and **Table 5.2**, respectively. Due to the increased secretion of ECM factors *in vivo*, increasing the fibroblast proportion in the cell population *in vitro* is expected to decrease the time required to form a 3D structure.

Table 5.1. Fraction of successful formation of 3D cellular structures with different percent cell populations and exposure times (hours) for printing with magnetic assistance. Interruptions were introduced to the culture well to remove the paramagnetic medium. A cut-off of 75% is used to determine the appropriate time required for successful formation.

Exposure time / Cell population	**3**	**6**	**9**	**12**	**24**
MDA-MB-231	*0*	*0*	*29*	*38*	*100*
12.50%	*0*	*13*	*88*	*88*	*100*
25%	*0*	*63*	*100*	*100*	*100*
50%	*50*	*75*	*100*	*100*	*100*
Fibroblast	*100*	*100*	*100*	*100*	*100*

Table 5.2. Fraction of successful formation of 3D cellular structures with different percent cell populations and exposure times (hours) for structures formed through gravitational settling. Interruptions were introduced to the culture well to replace the cell medium. A cut-off of 75% is used to determine the appropriate time required for successful formation.

Exposure time / Cell	**3**	**6**	**9**	**12**	**24**	**48**

population						
MDA-MB-231	*0*	*0*	*0*	*0*	*41*	*86*
12.50%	*0*	*0*	*0*	*0*	*61*	*92*
25%	*0*	*0*	*21*	*72*	*80*	*92*
50%	*42*	*56*	*68*	*78*	*92*	*100*
Fibroblast	*48*	*56*	*58*	*69*	*81*	*88*

Each cell population requires a different incubation time to form a 3D cellular structure (**Figure 4(a)**). A single monotypic MDA-MB-231 3D cellular structure is confirmed at 24 hours when printed with magnetic assistance. Similar formation times have been reported for non-growing aggregates,[7] or ones created with rBM in a scaffold-free environment[1] that promotes intercellular interactions. Otherwise, longer formation times are required to form robust 3D MDA-MB-231 structures.[5, 51]

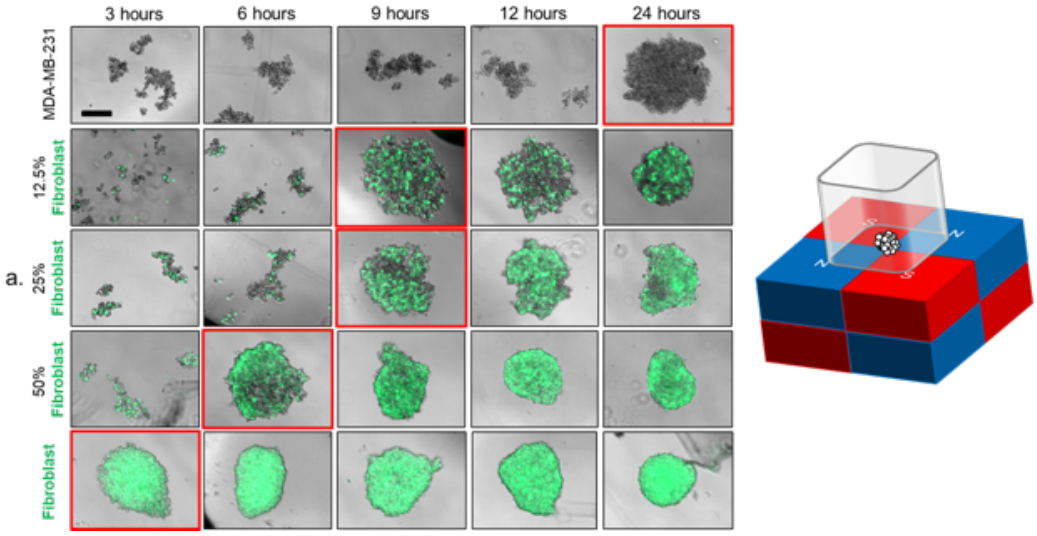

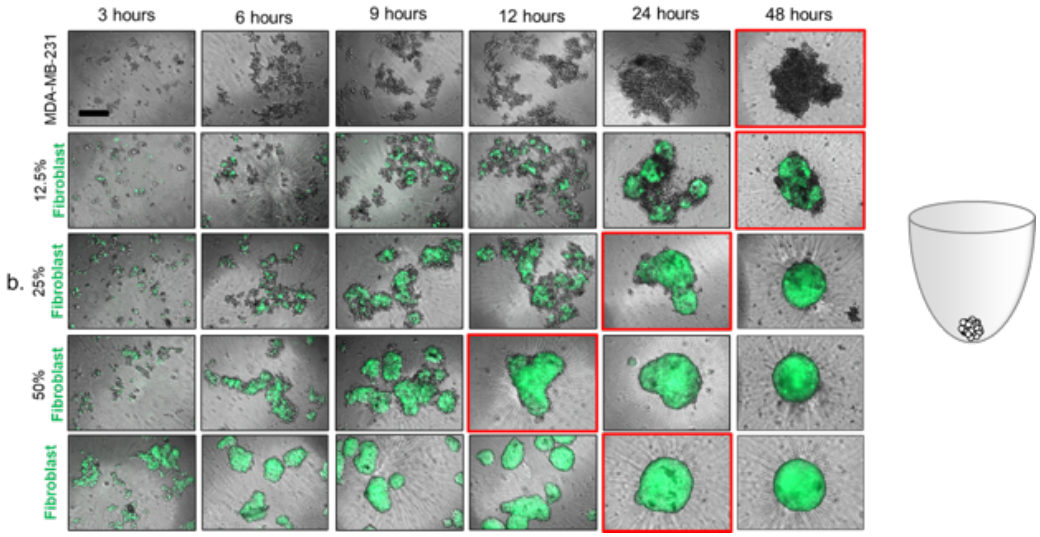

Figure 5.5: Formation of 3D cellular structures. 3D cellular structures composed of MDA-MB-231 (monotypic), 12.5, 25 and 50 % fibroblast (co-cultures) and fibroblast (monotypic) cells (**a**) printed with magnetic assistance and (**b**) formed through gravitational settling are imaged at 3, 6, 9, 12, 24 and 48 hours. A monotypic 3D structure containing MDA-MB-231 is formed at 24 hours with magnetic assistance in contrast a similar formation at 48 hours when gravity is used alone. As the proportion of fibroblast cells increases, the structure formation time decreases. Again, magnetically-assisted printing reduces structure formation time as compared to formation under the influence of gravity alone for all cell populations. The panels with red borders indicate the time it takes to form a 3D cellular structure. The images are taken after the cell media is replaced with fresh medium for both methods. The scale bar is equal to 100 μm.

To further reduce the time for printing a 3D MDA-MB-231 structure, we introduce fibroblasts in various proportions. *In vivo*, fibroblasts are found throughout the body and

act as scaffolds for other cells.[36] Therefore, fibroblasts can be used in an *in vitro* setting where they act as an adhesive that promotes intercellular interactions. As the proportion of fibroblasts increases in these binary cell mixtures, the time required to print a 3D cellular structure decreases.

The 12.5 and 25% fibroblast cell populations both produce 3D structures at 9 hours, while with 50% fibroblasts a 3D structure is formed at 6 hours with magnetic assistance (**Figure 5.5**(**a**)). A monotypic fibroblast cell population forms a 3D cellular structure within 3 hours with magnetic assistance. These rapid formation times are within the exposure limits of Gd-DTPA determined from the MTT results. The results support our hypothesis that fibroblasts act as 'glue' that supports the formation of 3D cellular structures.

A U-bottom ULA plate that employs gravitational setting to form 3D structures is used as a control. The cell media is replaced at identical incubation periods used for magnetically-assisted printing and images taken of their morphologies (**Figure 5.5**(**b**)). As expected, it takes longer to form a structure with gravity alone. Although it is expected that increasing the proportion of fibroblasts reduces the time requires to form a 3D structure, an exception to this is seen in the 3D structures composed of 50% fibroblasts which formed at 12 hours, whereas a monotypic fibroblasts culture required 24 hours to form. This is possibly due to increased cell-cell interactions between the two cell types, which promotes the production of ECM.

Monotypic MDA-MB-231 and fibroblast cell populations form 3D cellular structures at 48 and 24 hours, respectively. Similar to structures printed with magnetic

assistance, introducing fibroblasts accelerates the formation of a 3D structure compared to one produced with a monotypic MDA-MB-231 cell population. When the fibroblast proportion introduced into an MDA-MB-231 cell population is doubled, the structure formation time decreases by half. 3D structures with 12.5% fibroblast are formed at 48 hours, those with 25% fibroblast at 24 hours and with 50% fibroblast at 12 hours.

Observations made prior to 3D structure formation indicate that numerous 3D structures are present instead of a single principal cellular structure. Therefore, the delay in structure formation does not suggest an inability of the cells to establish intercellular interactions but is instead a consequence of their distances from each other as these interactions occur.

5.3.4 Growth of monotypic and co-culture 3D cellular structures to assess the influence of cellular composition and method of formation

The long-term growth characteristics of 3D cellular structures, maximum projected areas, and circularities [7, 23, 52, 26, 53] are measured. Since the maximum projected structures are not perfect circles, it is not appropriate to use diameter as a metric.[5] Instead, the maximum projected area is used.

The maximum projected area of the 3D cellular structures is expected to decrease as a result of increasing cell agglomeration density before the area increases due to cell growth. A decrease in projected area measurements that follows a formation period is considered contraction. This pattern of contraction followed by an increase in maximum projected size is typical for multicellular tumor spheroids (MCTS),[21] which are

agglomerations of cancer cells in a scaffold-free environment. A size increase indicates that cells are proliferating and that the 3D cellular structure is growing.

Circularity is defined as,

$$\text{Circularity} = 4\pi(\text{Area}/\text{Perimeter}^2), \quad (1)$$

where a value of 1 indicates a perfect circle. Values smaller than 1 indicate a deviation from a perfect circle, but do not provide information that describes the morphology of the structure.

Over a duration of 336 hours, 3D cellular structures printed with magnetic assistance (**Figure 5.6**(**a**)) and formed under the influence of gravity alone (**Figure 5.6**(**b**)) exhibit different growth behaviors. Maximum projected area measurements (**Figure 5.6**(**a**,**i**)) for magnetically-printed monotypic MDA-MB-231 3D structures and those containing 12.5 and 25% fibroblast co-cultures decrease by 39, 64 and 55 %, respectively from their times of formation to 72 hours. Meanwhile, the maximum projected areas of 50% fibroblast-containing and monotypic fibroblast 3D structures decrease by 51 and 57 % respectively from their times of formation until 24 hours and then maintained until 72 hours. An increase of 44, 61, 50, 50 and 30% in maximum projected areas is observed from 144 to 336 hours for monotypic MDA-MB-231, 12.5, 25 and 50% fibroblast-containing, and monotypic fibroblast 3D structures, respectively. This suggests that there is cell growth in the 3D structures.

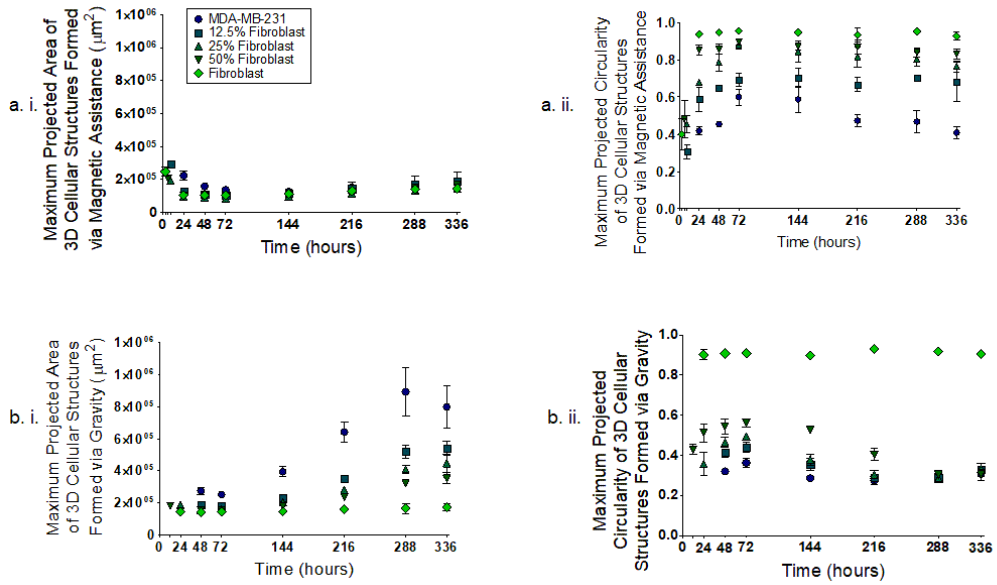

Figure 5.6: Growth of 3D cellular structures printed with via magnetic assistance and formed under the influence of gravity alone. (**i**) Maximum projected area and (**ii**) circularity measurements of 3D cellular structures (**a**) printed with magnetic assistance and (**b**) formed through gravitational settling. The maximum projected areas of the monotypic MDA-MB-231, and 12.5 and 25% fibroblast co-culture 3D structures printed with magnetic assistance decrease by 39, 64 and 55%, respectively after their initial formation. The maximum projected areas of 3D structures containing a 50% fibroblast co-culture and a monotypic fibroblast decrease by 51 and 57 % respectively until 24 hours. These maximum projected areas are maintained until 72 hours. From 144 hours until 336 hours, the maximum projected areas increase slightly within experimental error. In contrast, the maximum projected areas of 3D cellular structures formed under the influence of gravity alone (**b**,**i)** increase by 103, 130, 117 and 94 % from 144 to 336 hours for

monotypic MDA-MB-231, and 12.5, 25 and 50% fibroblast 3D structures, respectively. As the proportion of fibroblasts increases, structure circularity (**a**,**ii**) and (**b**,**ii**) also improves. The legend in (**a**,**i**) applies to graphs in panels (**a**,**ii**), (**b**,**i**) and (**b**,**ii**).

The maximum projected circularity (**Figure 5.6**(**a**,**ii**)) of monotypic fibroblast 3D cellular structures is maintained between 3 and 336 hours. However, between their times of formation and 72 hours, the co-cultured 3D structures become more circular, with maximum projected circularity increasing by 127, 94 and 86% for 12.5, 25 and 50% fibroblast-containing binary cell mixtures, respectively. From 144 to 336 hours, their maximum projected circularity is essentially maintained. As the proportion of fibroblasts in the binary mixture increases, the circularity also increases. Monotypic MDA-MB-231 3D structures become more circular between their time of formation (24 hours) and 72 hours with an increase of 43%. At 144 hours, their maximum projected circularity decreases by 30% at 336 hours.

Maximum projected areas for monotypic MDA-MB-231 and co-cultured 3D cellular structures formed due to gravitational settling (**Figure 5.6(b**,**i**)) remain unchanged from their times of formation (48, 48, 24 and 12 hours, for monotypic MDA-MB-231, and 12.5, 25 and 50% fibroblast co-cultured 3D structures, respectively) until 72 hours. Afterward, these areas increase but do so more rapidly from 144 to 336 hours (where they exhibit 103, 130, 117 and 94% increases, respectively). As the fibroblast concentration increases in the co-cultured structures, the increase in the maximum projected area becomes less rapid. Maximum projected area measurements for monotypic fibroblast 3D cellular

structures do not change significantly from their times of formation (24 hours) until 336 hours.

The maximum projected circularity (**Figure 5.6**(**b**,**ii)**) of a monotypic fibroblast 3D cellular structure formed through gravitational settling also does not change from its time of formation until 336 hours. The circularities of monotypic MDA-MB-231 and co-cultured 3D cellular structures increase by 10, 6, 38 and 31% for monotypic MDA-MB-231, and 12.5, 25 and 50% fibroblast-containing 3D structures, respectively, from their times of formation until 72 hours. For monotypic MDA-MB-231, 12.5 and 25% fibroblast co-cultured 3D structures, their maximum projected circularity decreases by 24, 34 and 38%, respectively from 72 hours until 216 hours. For the 50% fibroblast co-culture 3D structure, its maximum projected circularity decreases by 46% from 72 hours until 288 hours. As the proportion of fibroblasts increase, the circularity is higher and maintained until 336 hours, at which time the circularity between these various 3D structures is indistinguishable.

The growth characteristics observed from **Figure 5.6** suggest that Gd-DTPA has a detrimental effect on 3D structures, preventing them from growing. Although fibroblast-containing aggregates appear to have higher amounts of Gd^{3+} per structure, the changes in their maximum projected areas are not significant. The MDA-MB-231 3D structures are affected by Gd-DTPA, but this is not suggested by the ICP-MS or MTT results. In contrast to the maximum projected area results, magnetically assisted printing improves the longer-term circularity of the structures as compared with those formed through gravitational settling. For all cases, the 3D structures are more circular when printed with magnetic assistance as compared to those with the same initial composition formed through

gravitational settling. Circularity is expected to be a consequence of cell-cell interactions and the production of ECM. In this investigation, fibroblasts produce the most ECM, supporting their maintained circularity. On the other hand, toxicity of Gd-DTPA towards MDA-MB-231 (**Figure 5.6(a,ii)**) manifests its effects over time and can be seen by decreased circularity due to reduced number of interacting cells and production of ECM. In the case of 3D structures formed through gravitational settling (**Figure 5.6(b,ii)**), the Gd-DTPA over time for 3D structures composed of co-cultures and monotypic cultures of MDA-MB-231 is maintained, but is less in comparison to 3D structures formed via magnetic assistance. This is likely due to reduced critical cell-cell interactions during the early stages of formation, resulting in less circular 3D structures over time.

A lytic process at the time of measurement is employed to quantify cellular ATP, which accesses all available ATP within the 3D cellular structure that may have otherwise been unaccounted for if an MTT assay were used. The cellular organization of metabolically active cells in the 3D structures can contribute to different ATP levels. Since the sizes of the 3D structures cannot be controlled, the measurements refer to total cellular ATP that is compared to a 40 pmol ATP reference and quantified with a standard curve calibration. This assay does not measure apoptosis or necrosis. Growth is indicated by an increasing amount of ATP. As described in the manufacturer specifications (Promega), 40 pmol is the expected ATP recovery from a spheroid that has a diameter of 250 μm, consistent with the sizes of the 3D structures in this investigation.

Cellular ATP measurements for 3D cellular structures are taken from the time of formation until 336 hours to determine the cell viability (**Figure 5.7**). Cellular ATP

measurements for monotypic and co-culture 3D structures printed with magnetic assistance (**Figure 5.7**(**a**)) are indistinguishable from one another for all measurements. This minimal change in cellular ATP is similar to the maximum projected area measurements (**Figure 5.6(a**,**i**)).

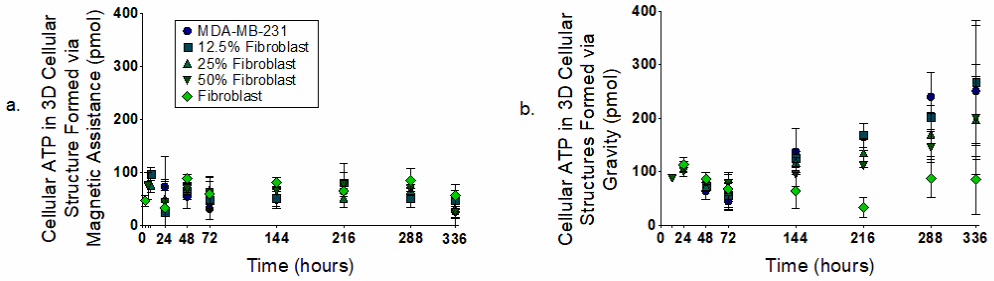

Figure 5.7: Cellular ATP of monotypic and co-culture 3D cellular structures. Measurements are made from the time of formation until 336 hours for monotypic and co-cultured 3D cellular structures (**a**) printed with magnetic assistance and (**b**) formed through gravitational settling. For monotypic and co-cultured 3D structures (**a**) printed with magnetic assistance, cellular ATP does not change significantly within experimental error. Monotypic MDA-MB-231 and co-cultures for structures (**b**) formed under the influence of gravity alone have a minimum cellular ATP level at 72 hours, and monotypic fibroblast cellular structures at 216 hours. The legend in (**a**) applies to panel (**b**).

Similar scaling of cellular ATP to the maximum projected area is observed for 3D structures formed with gravity alone (**Figure 5.7**(**b**)). The cellular ATP of monotypic MDA-MB-231 and co-cultured 3D structures decreases from their times of formation by 30, 23, 20 and

10% until 72 hours, followed by an increase of 461, 375, 212 and 154% until 336 hours for monotypic MDA-MB-231, 12, 25 and 50% fibroblast co-cultured structures, respectively. As the proportion of fibroblasts increases, the increase in cellular ATP for each measurement is less rapid. However, monotypic fibroblast 3D cellular structures exhibit very different behavior since the minimum cellular ATP occurs at 216 hours.

This also suggests that Gd-DTPA has a countering effect on the growth of the 3D structures. We previously observed a different phenomenon when a 2D monolayer of MDA-MB-231 cells was exposed to 0.1, 1 and 10 mM Gd-DTPA.[28] There, the cells did not appear to respond to Gd-DTPA, displaying similar characteristics to their control (0 mM) at 3 days (percent cell viable cell count) and at 6 hours (cell migration). This was conjectured to occur due to the absence of an estrogen receptor on these cells, which responds to Gd-DTPA as a xenoestrogen.[28] The complexity of a 3D structure, however, may introduce interactions with Gd-DTPA that interfere with regular cellular behaviour.

Although printing with magnetic assistance improves the reproducibility of 3D cellular structures, which is demonstrated by the better maximum projected area and circularity, this method could be improved further by replacing Gd-DTPA with a less cytotoxic paramagnetic agent. Alternatively, the present system can be optimized to limit cell exposure to Gd-DTPA by reducing the exposure time or salt concentration. To obtain a better understanding of the specific effect that Gd-DTPA has on the 3D structures, additional assays that target different metabolic processes should be performed, such as the resazuran reduction assay,[54] response to drug toxicity,[21] immunostaining,[55] and profiling gene expression.[9]

5.3.5 Self-distribution of individual cell lines within co-cultured 3D cellular structures to assess the significance of cell populations and method of formation

The segregation of cells within a 3D cellular structure is influenced by the cell lines used in the co-culture.[56] We find that differences in the self-distributions of MDA-MB-231 and fibroblasts also depends on the method of formation (**Figure 5.8**). The long-term distributions are observed using confocal microscopy. For 3D structures printed with magnetic assistance (**Figure 5.8**(**a**)), numerous small regions containing fibroblasts (green) are observed at 3 days for an initial 12.5% fibroblast-containing mixture. This number of regions decreases at 7 days and continues to reduce when observed at 14 days. Similar behavior is observed for a 25% fibroblast-containing 3D structure, but there are smaller numbers of regions composed of MDA-MB-231 cells (blue) between 3 and 7 days. At 14 days, however, it becomes difficult to distinguish regions within the structures that contain primarily MDA-MB-231 cells or fibroblasts. The number of regions with primarily MDA-MB-231 cells appears to be unchanged in 50% fibroblast-containing 3D cellular structures. For all structures, single optical sections at z = 12 μm and z = 24 μm (**Figure 5.9**(**a**)) show that fibroblasts dominate within the mass, rather than form a capsule around the 3D cellular structure printed with magnetic assistance.

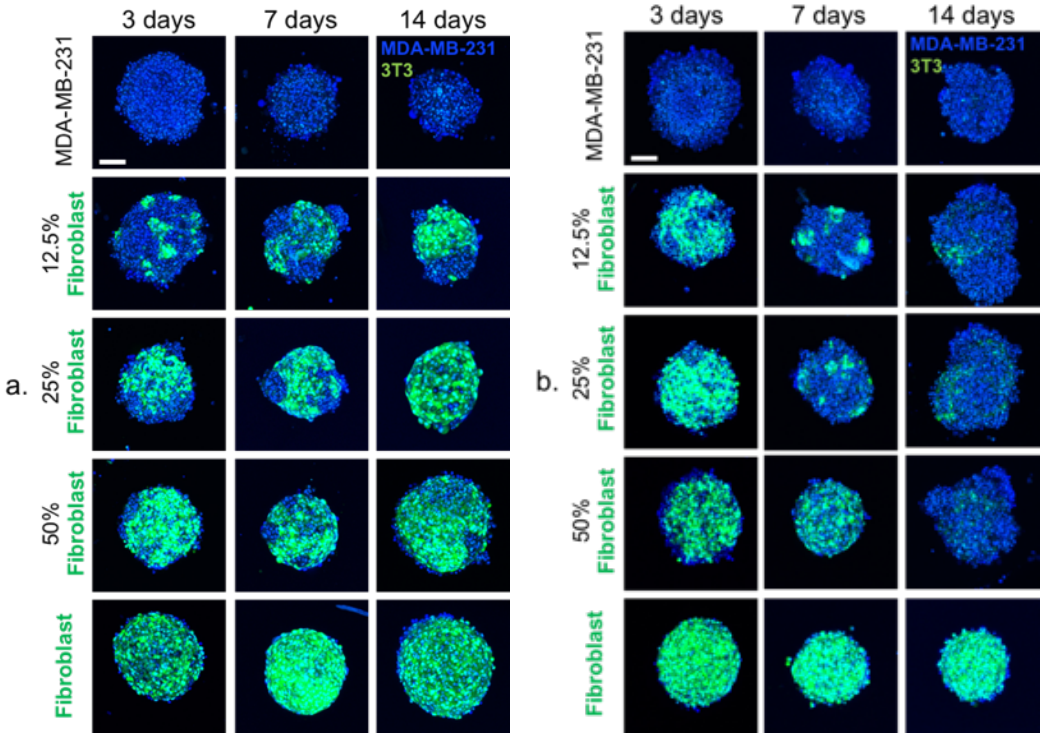

Figure 5.8: Visualization of self-distributing cell lines within co-culture 3D cellular structures following formation. Confocal z-stack images showing regional distributions of MDA-MB-231 (blue) and fibroblast (green) cells in 3D cellular structures (**a**) printed with magnetic assistance and (**b**) formed through gravitational settling at 3, 7 and 14 days. The scale bar is equal to 100 μm.

For 3D structures formed under the influence of gravity alone (**Figure 5.8**(**b**)), the proportion of fibroblasts appears to decrease over time and these cells concentrate toward the center of the structure, where they are surrounded by loosely-aggregated MDA-MB-231 cells. Similar to 3D cellular structures printed with magnetic assistance, single optical sections at z = 12 μm and z = 24 μm (**Figure 5.9**(**b**)) indicate that fibroblasts concentrate more within of 3D cellular structures formed through gravitational settling.

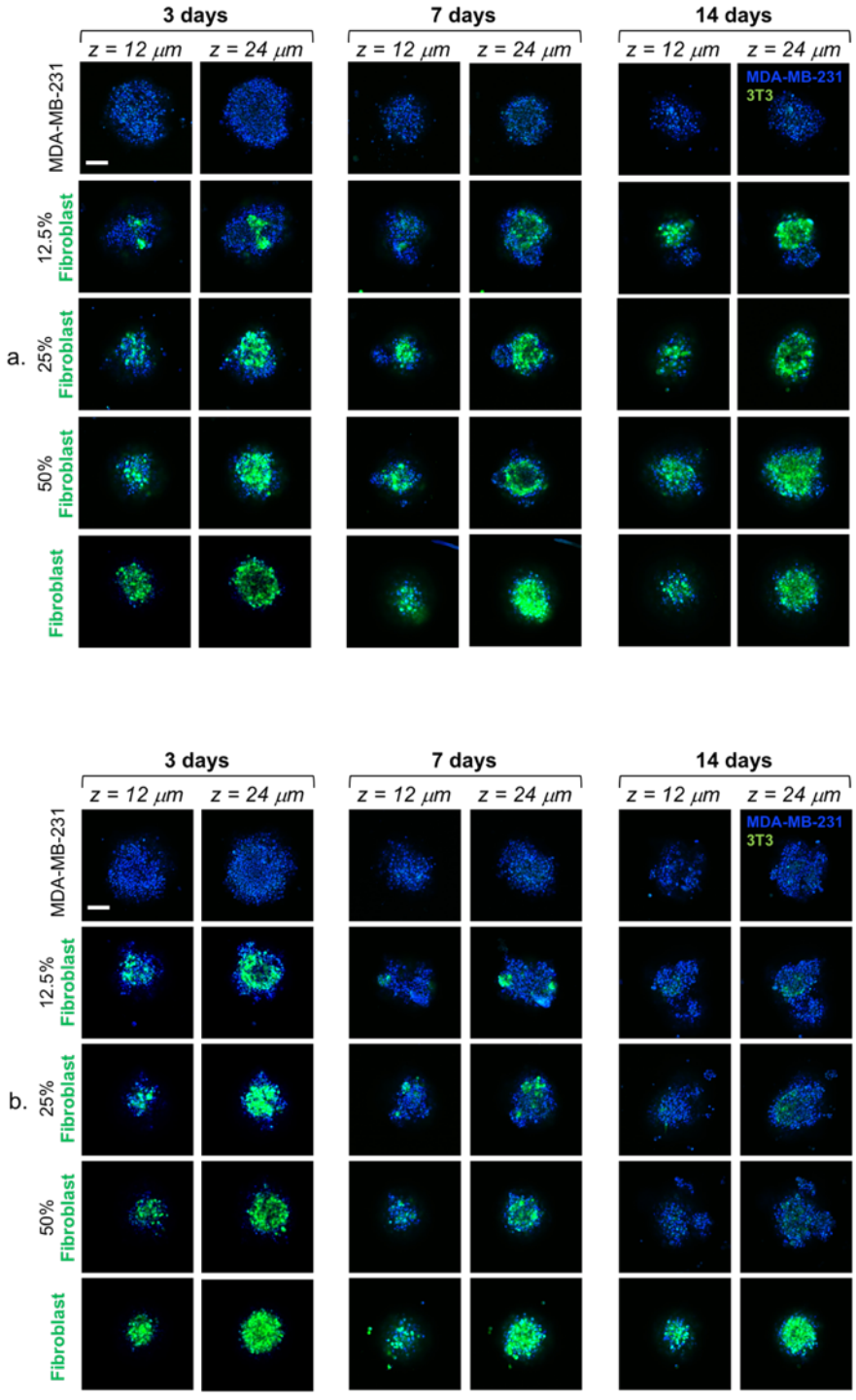

Figure 5.9: Single optical sections at z = 12 μm and z = 24 μm for 3D cellular structures. (**a**) Printed with magnetic assistance and (**b**) formed through

gravitational settling. Although the presence of fibroblasts diminishes over time for 3D cellular structures formed through gravitational settling, both methods of formation indicate that fibroblasts concentrate within the structures, rather than form a capsule.

The confocal microscopy analysis does not provide quantifiable data that can measure the physical space occupied by each cell line over time. The random orientations of cell constructs at the time of imaging can also affect the analysis. Although it may not be the case for the particular 3D cellular structures that we have produced, the difference in the doubling time between the two cell lines (36 hours for MDA-MB-231 and 20 hours for NIH/3T3, in 2D) should be considered when analyzing the relative proportions of each cell type over time.

In previous investigations, MDA-MB-231 have displayed endothelial-like morphologies when 3D cellular structures were cultured on Matrigel and injected into mice[6]. The ECM provided by fibroblasts may interact with tumor cells to prevent epithelium organization, instead of sustaining the formation of clusters.[31] The distribution of each cell line following formation might also be explained by the differences in their surface tensions[57], which is a consequence of adhesive and cohesive interactions of the cells[58] and is supported by the differential adhesion hypothesis (DAH)[59]. However, this does not explain the observed differences between the two methods of forming 3D cellular structures with identical cell population identities. Although the doubling time of each cell type suggests that fibroblasts should take over, formation of 3D structures via gravitational settling shows almost complete dominance of MDA-MB-231 cells at 14 days, while 3D

structures formed via magnetic printing indicates a greater proportion of fibroblasts. This may be due to toxicity of MDA-MB-231 cells to Gd-DTPA during magnetic printing, and lack of cell-cell interactions during formation during gravitational settling. The exact mechanisms need to be investigated further.

Previous investigations of 3D *in vitro* cultures of human breast cancer and fibroblast cells report that the fibroblasts encapsulate breast tumor cells, maintaining their presence on the periphery of the spheroid, which is comparable to the organization of *in vivo* tumors.[8] We observe this only for the 3D cellular structures printed with magnetic assistance. For clinically relevant cells, the specific intercellular interactions may be observed using immunohistochemistry.

The differences between the two methods of formation, magnetically assisted printing and gravitational settling, suggest explanations for the corresponding maximum projected area and circularity, and cellular ATP measurements. Although their distribution changes over time when the 3D structures are printed with magnetic assistance, the constant presence of fibroblasts maintains a conserved maximum projected area and circularity. This correlates with the ATP measurements, which are also conserved and do not change significantly, and are independent of the composition of the monotypic or co-culture 3D cellular structures. These observations suggest that printing through magnetic assistance is necessary to observe the long-term presence of both cell lines initially used. For 3D cellular structures formed through gravitational settling, the decrease in the presence of fibroblasts over time may explain the decrease in the maximum projected circularity of the structures.

Printing with magnetic assistance promotes intercellular interactions between monotypic cells that do not otherwise form 3D cellular structures readily. This is the case for the monotypic MDA-MB-231 cell population that is able to form reproducible 3D structures with magnetic assistance in 24 hours and through gravitational settling in 48 hours. However, the advantage of printing with magnetic assistance comes at the expense of limiting cell growth in the 3D structures that are produced.

5.4 Discussion

The unmet need for producing 3D cellular structures of MDA-MB-231 in a rapid high-throughput manner inspires unique approaches to overcome this challenge. This investigation explores how 3D cellular structures can be more rapidly printed with magnetic assistance than leveraging the influence of gravity alone. The results validate our hypothesis that (1) fibroblasts act as 'glue' that support the formation of 3D cellular structures, and (2) the structures are produced more rapidly and with higher reproducibility with magnetically assisted printing than through gravitational settling alone.

We elucidate the differences between 3D MDA-MB-231 cellular structures printed with magnetic assistance and those formed under the influence of gravity alone. Fibroblasts are introduced to promote cell agglomeration. This is seen for both methods of forming 3D structures that contain human breast adenocarcinoma cells. We demonstrate that 3D structures composed of MDA-MB-231 cells can be printed with magnetic assistance within 24 hours without using a scaffold or matrix to promote cell agglomeration. This incubation time is not observed in literature without additional reagents.

To avoid affecting the magnetic susceptibility of the cells by labeling with[8] or internalization of[60] a magnetic particle, the magnetic susceptibility of the medium is changed by adding a magnetic salt, creating a paramagnetic solution.[61] A lower magnetic susceptibility causes the cells to be displaced towards regions of the lowest magnetic field strength.[62]

Printing with magnetic assistance (also termed the magneto-Archimedes effect[63]) allows label-free manipulation of non-magnetic cells. A magnetic buoyancy force is introduced by applying a magnetic field to a system where there is a difference in the magnetic susceptibility of a suspended analyte and its surrounding suspension medium.[64] The magnetic force acting on a cell,

$$F_m = [(\chi_c - \chi_m)/2\mu_0] V_c \nabla |\mathbf{B}|^2, \quad (2)$$

where χ_c and χ_m denote the magnetic susceptibilities of the suspended cells and the suspension medium, respectively, μ_0 the permeability of free space, V_c the volume of a cell and $\nabla|\mathbf{B}|^2$ the gradient of the square of the magnetic field. This is a high throughput method, e.g., realized by forming an array of magnets in an alternating North-South-North-South orientation and aligning a standard 96- or 384-well plate so that the intersection of four magnets is centered to each well (**Figure 5.1** and **Video 5.1**). Each well containing a suspension of diamagnetic cells in the paramagnetic medium will form a 3D cellular structure as described in ***Materials and methods***.

Although NIH/3T3 cells are of animal origin, their intended use in this study is to evaluate the influence of fibroblasts on the formation of 3D cellular structures for cell types

which are difficult to cohere without using additional reagents. Such a use of cell lines from different species has been used in previous co-culture models. [34, 65] Since human and mouse fibroblasts behave similarly in terms of their ability to produce ECM proteins (such as collagen),[66-68] the conclusions of our study demonstrate the capability of magnetically-assisted printing in this co-culture model.

For disease-specific modeling in a clinical setting, where it will be necessary to use human-derived cell lines or primary cells, this technique has the potential to form different shapes which may be more physiologically relevant than a spherical model. Improving the formation of 3D cellular structures by printing them with magnetic assistance has applications for tissue engineering, drug discovery, and lab-on-chip devices.

5.5 Materials and methods

5.5.1 Cell Culture

Human MDA-MB-231 (American Type Culture Collection (ATCC), USA) and mouse green fluorescent protein (GFP)-transfected (GFP^+) NIH/3T3 (ATCC, USA, code CRL-1658) cells were both gifts obtained from colleagues. GFP^+ NIH/3T3 cells were used for all investigations that mentioned fibroblast or NIH/3T3 cells. Both cell lines were maintained in Dulbecco Modified Eagle's medium (DMEM, Life Technologies, catalog number 12800-082) containing 10% fetal bovine serum (FBS, cat.no. 12484028). Phosphate buffered saline (PBS, cat.no. 10010023) and Trypsin-EDTA (0.25%), phenol red (cat.no. 25200056) used for cell culture maintenance purchased from Life

Technologies, Canada. The cells were maintained at standard culture conditions (37°C, 5% CO_2 in a humidified environment).

5.5.2 Synthesis of Paramagnetic Gd-DTPA Medium

Gadopentetic acid (Gd-DTPA) salt hydrate purchased from Sigma Aldrich, Canada (cat.no. 381667) was used to make a 200 mM Gd-DTPA solution in the culture medium. Immediately after dissolution, 1 M sodium hydroxide (NaOH, Alfa Aesar, cat.no. A16037) was then added dropwise to adjust the pH to physiologic levels, to approximately 7.4±0.2. Contents were constantly mixed on a stir plate as Gd-DTPA and NaOH were added. Subsequent dilutions were prepared with the culture medium.

5.5.3 Preparation of 3D Cellular Structures

3D cellular structures printed with magnetic assistance were prepared by seeding a cell concentration of 5000 cells/80 μL of 25 mM Gd-DTPA culture medium per well into a 384-well flat-bottom ULA plate (Corning, product no. 4588). A quartet of 4.5×4.5×4.5 mm N52 magnets (Zigmyster Magnets) was arranged into an N-S-N-S orientation and placed directly underneath each well. 3D cellular structures formed through gravitational settling were prepared by seeding a cell concentration of 5000 cells/80 μL of regular, Gd-DTPA-free (0 mM Gd-DTPA) culture medium per well into a 384-well U-bottom ULA plate (SBio, cat.no. MS-9384UZ). At the end of the specified exposure time during magnetically assisted printing, the paramagnetic medium was removed through a series of washes with regular, Gd-DTPA-free culture medium (0 mM Gd-DTPA). This was also performed for 3D cellular structures formed through gravitational settling, to determine the appropriate

formation time. Half of the culture medium present in the 3D cellular structure samples was removed and replaced with fresh culture medium every 3 days.

5.5.4 Inductively Coupled Plasma Mass Spectrometry (ICP-MS)

MDA-MB-231 and fibroblast 3D cellular structures printed with magnetic assistance and formed through gravitational settling were prepared and pooled together after 24 hours. The pooled samples were then centrifuged and the supernatant was removed. Each sample was washed with PBS five times to remove residual cell culture medium, which also contained Gd-DTPA for the 3D cellular structures formed via magnetic assistance. A final wash with ultrapure water was performed to dilute the salts present in PBS, which could interfere with ICP-MS measurements. The samples were stored at -20°C until the ICP-MS apparatus (Agilent 7700 series) was ready. When ready, the samples were digested with concentrated nitric acid and measured to detect Gd^{3+} (157 atomic mass units) with helium for plasma generation.

5.5.5 MTT Assay Analysis for Viability of 2D Cell Monolayers

For each cell population, 1000 cells were plated into a 96-well tissue culture-treated plate at 0 hours. Duplicate samples were prepared and exposed to 100 μL of either 0 or 25 mM Gd-DTPA in the culture medium for each time of measurement. MTT reagent (3-(4,5-dimethylthiazol-2-yl)-2,5-diphenyltetrazolium bromide, Invitrogen, Canada, cat.no. M6494) was made into a 5 mg/mL solution in PBS. At 3 and 24 hours, the culture medium was removed from the samples and replaced with fresh culture medium. 10 μL of MTT solution was added to each sample and incubated for 3 hours at standard culture conditions.

Following incubation, 85 µl of the solution was removed and 50 µL dimethyl sulfoxide (DMSO, Sigma Aldrich, Canada, cat.no. D4540) was added. The samples were again incubated at standard condition, for 10 minutes. The plate was then shaken and the absorbance was read at 570 nm using the Tecan Infinite M200 plate reader. For each incubation period, the absorbance was normalized to the 0 mM (Gd-DTPA-free) control sample to measure the relative percent viability of cells exposed to 25 mM Gd-DTPA.

5.5.6 Size Measurements

For each monotypic and co-culture 3D cellular structure printed with magnetic assistance or formed through gravitational settling, images were taken using a Carl Zeiss Axio Observer Z1 microscope: at the time of formation, 24 hours (if applicable), 48 hours (if applicable), 72, 144, 216, 288 and 336 hours. Images were analyzed with Fiji (ImageJ) imaging software, and maximum projected area and circularity measurements were obtained. The number of measurements taken (described in section **5.5.9**) for maximum projected area and circularity minimize variation between the height and the cross section. The amount of variation introduced is expected to be little since a spherical construct is stable.

5.5.7 Measurements of Cellular ATP

For each monotypic and co-cultured 3D cellular structure printed with magnetic assistance or formed under the influence of gravity alone, samples in 25 µL of their medium were transferred into a white U-bottom 384-well plate (SBio, cat.no. MS-9384WZ). 25 µL of CellTiter®-Glo 3D Viability Assay (Promega, part no. G9681) was added to lyse the 3D

cellular structures and access cellular adenosine triphosphate (ATP). The samples were then shaken at 3 mm amplitude for 5 minutes and left to incubate at room temperature for an additional 25 minutes. Finally, the samples were read by luminescence with 1 second attenuation time. For all readings, a 40 pmol sample was used as a reference and normalized to a standard curve to quantify the relative luminescence units (RLU).

5.5.8 Confocal Microscopy

For each monotypic and co-culture 3D cellular structure printed with magnetic assistance or formed through gravitational settling, three replicate samples were prepared at time equal to 0. On days 2, 6 and 13, 4',6-diamidino-2-phenylindole (DAPI) blue fluorescent nucleic acid stain was added to each sample, staining all nuclei, both MDA-MB-231 and fibroblast, blue. After 24 hours of incubation at standard conditions, the 3D cellular structures were imaged on days 3, 7 and 14, respectively, using a Nikon A1R confocal microscope. A z-stack with a step size of 2.4 μm was acquired from the bottom-most focused plane to approximately half the thickness of the 3D cellular structures. 2D reconstructed images were formed by taking the maximum intensity pixels at each stack for blue and green fluorescent channels. MDA-MB-231 cells were identified by their nucleus (blue) while fibroblasts were identified by an overlay of their nucleus and inherent GFP^+ fluorescence (blue and green, respectively). Excitation and emission wavelengths of 395/509 and 358/461 were used for GFP and DAPI, respectively.

5.5.9 Statistical Analysis

Three biological samples of 3D cellular structures printed with magnetic assistance and formed through gravitational settling were prepared for ICP-MS measurements, each with ≥ 64 technical replicates. Pooled biological samples that were below the method reporting limit (MLR) were below the sensitivity limit of the instrument and therefore assigned a value of 0. ICP-MS results were analyzed by the standard error of the mean (SEM) of the pooled biological samples. A two-way analysis of variance (ANOVA) with Bonferroni post-test was performed. A p-value of < 0.01 had two-star significance (**), while a p-value of < 0.001 had three-star significance (***).

Three biological samples of 2D monolayers for each cell population were prepared for MTT analysis, with six technical replicates for control and 25 mM Gd-DTPA samples, at each time of measurement i.e. 3 and 24 hours. MTT results for 25 mM Gd-DTPA were control-normalized to their respective 0 mM Gd-DTPA sample and analyzed by SEM. A two-way ANOVA with Bonferroni post-test was performed. A p-value of > 0.05 had no statistical significance, while a p-value of < 0.05 had one-star significance (*).

Two biological samples of 3D cellular structures printed with magnetic assistance and six biological samples of 3D cellular structures formed through gravitational settling were prepared for the determination of the formation of 3D cellular structures. For each sample, four technical replicates were used at each specified time.

Two biological samples of 3D cellular structures printed with magnetic assistance and three biological samples of 3D cellular structures formed through gravitational settling

were measured for their maximum projected area and circularity. For each sample, four technical replicates were used and SEM was calculated.

Three biological samples of 3D cellular structures printed with magnetic assistance and three biological samples of 3D cellular structures formed through gravitational settling were prepared for the measurement of cellular ATP. For each sample, four technical replicates were used and SEM was calculated.

Three biological samples were prepared for 3D cellular structures printed with magnetic assistance and three biological samples of 3D cellular structures formed through gravitational settling were prepared and imaged for confocal analysis. Representative images were selected for qualitative analysis of the cell distribution within the 3D cellular structures following formation.

All statistical analysis was performed using GraphPad Prism software with a 95% confidence interval.

5.6 Acknowledgements

General: The authors thank Professor Juliet Daniel (Biology, McMaster University) for donating MDA-MB-231 cells, and Alireza Shahin-Shamsabadi, Rana Attalla and Professor Ravi Selvaganapathy (School of Biomedical Engineering, McMaster University) for donating GFP-transfected NIH/3T3 cells, Tahereh Majdi for supplying reagents used for measuring cellular ATP, SBio for supplying U-bottom ULA plates, and Jeffrey Warner of the Biotron Experimental Climate Change Research Center at The University of Western Ontario for performing the ICP-MS measurements.

Funding: This work was supported by the Natural Sciences and Engineering Research Council of Canada (NSERC) Discovery Grant [RGPIN-2014-04066], Canada Foundation for Innovation John R. Evans Leaders Fund (CFI-JELF), the Ontario Research Fund Research Infrastructure [ORF-RI: Grant No. 33016].

Author contributions: S. Mishriki completed all experiments and was the lead writer of the manuscript. S. Aithal co-lead the confocal microscopy investigation. All authors contributed to editing the final version of the manuscript.

Competing interests: The authors declare that there are no competing financial interests regarding the publication of this article. The authors declare that there is no conflict of interest regarding the publication of this article.

5.7 References

1. Ivascu, A.; Kubbies, M., Rapid generation of single-tumor spheroids for high-throughput cell function and toxicity analysis. *Journal of biomolecular screening* **2006,** *11* (8), 922-932.

2. Nath, S.; Devi, G. R., Three-dimensional culture systems in cancer research: Focus on tumor spheroid model. *Pharmacology & therapeutics* **2016,** *163*, 94-108.

3. Razian, G.; Yu, Y.; Ungrin, M., Production of large numbers of size-controlled tumor spheroids using microwell plates. *JoVE (Journal of Visualized Experiments)* **2013,** (81), e50665.

4. Kunz-Schughart, L. A.; Heyder, P.; Schroeder, J.; Knuechel, R., A heterologous 3-D coculture model of breast tumor cells and fibroblasts to study tumor-associated fibroblast differentiation. *Experimental cell research* **2001,** *266* (1), 74-86.

5. Rustamov, V.; Hafner, M.; Rudolf, R., Bone sialoprotein shows enhanced expression in early, high-proliferation stages of three-dimensional spheroid cell cultures of breast cancer cell line MDA-MB-231. *Frontiers in oncology* **2019,** *9*, 36.

6. Harrell, J. C.; Pfefferle, A. D.; Zalles, N.; Prat, A.; Fan, C.; Khramtsov, A.; Olopade, O. I.; Troester, M. A.; Dudley, A. C.; Perou, C. M., Endothelial-like properties of claudin-low breast cancer cells promote tumor vascular permeability and metastasis. *Clinical & experimental metastasis* **2014,** *31* (1), 33-45.

7. Badea, M. A.; Balas, M.; Hermenean, A.; Ciceu, A.; Herman, H.; Ionita, D.; Dinischiotu, A., Influence of Matrigel on Single-and Multiple-Spheroid Cultures in Breast Cancer Research. *SLAS DISCOVERY: Advancing Life Sciences R&D* **2019,** *24* (5), 563-578.

8. Jaganathan, H.; Gage, J.; Leonard, F.; Srinivasan, S.; Souza, G. R.; Dave, B.; Godin, B., Three-dimensional in vitro co-culture model of breast tumor using magnetic levitation. *Scientific reports* **2014,** *4*, 6468.

9. Kenny, P. A.; Lee, G. Y.; Myers, C. A.; Neve, R. M.; Semeiks, J. R.; Spellman, P. T.; Lorenz, K.; Lee, E. H.; Barcellos-Hoff, M. H.; Petersen, O. W., The morphologies of breast cancer cell lines in three-dimensional assays correlate with their profiles of gene expression. *Molecular oncology* **2007,** *1* (1), 84-96.

10. Manni, A.; Washington, S.; Griffith, J. W.; Verderame, M. F.; Mauger, D.; Demers, L. M.; Samant, R. S.; Welch, D. R., Influence of polyamines on in vitro and in vivo features of aggressive and metastatic behavior by human breast cancer cells. *Clinical & experimental metastasis* **2002,** *19* (2), 95-105.

11. Hughes, C. S.; Postovit, L. M.; Lajoie, G. A., Matrigel: a complex protein mixture required for optimal growth of cell culture. *Proteomics* **2010,** *10* (9), 1886-1890.

12. Hongisto, V.; Jernström, S.; Fey, V.; Mpindi, J.-P.; Sahlberg, K. K.; Kallioniemi, O.; Perälä, M., High-throughput 3D screening reveals differences in drug sensitivities between culture models of JIMT1 breast cancer cells. *PloS one* **2013,** *8* (10), e77232.

13. Cavo, M.; Caria, M.; Pulsoni, I.; Beltrame, F.; Fato, M.; Scaglione, S., A new cell-laden 3D Alginate-Matrigel hydrogel resembles human breast cancer cell malignant morphology, spread and invasion capability observed "in vivo". *Scientific reports* **2018,** *8* (1), 5333.

14. Froehlich, K.; Haeger, J.-D.; Heger, J.; Pastuschek, J.; Photini, S. M.; Yan, Y.; Lupp, A.; Pfarrer, C.; Mrowka, R.; Schleußner, E., Generation of multicellular breast cancer tumor spheroids: Comparison of different protocols. *Journal of mammary gland biology and neoplasia* **2016,** *21* (3-4), 89-98.

15. Edmondson, R.; Broglie, J. J.; Adcock, A. F.; Yang, L., Three-dimensional cell culture systems and their applications in drug discovery and cell-based biosensors. *Assay and drug development technologies* **2014,** *12* (4), 207-218.

16. Verjans, E. T.; Doijen, J.; Luyten, W.; Landuyt, B.; Schoofs, L., Three-dimensional cell culture models for anticancer drug screening: Worth the effort? *Journal of cellular physiology* **2018,** *233* (4), 2993-3003.

17. Asghar, W.; El Assal, R.; Shafiee, H.; Pitteri, S.; Paulmurugan, R.; Demirci, U., Engineering cancer microenvironments for in vitro 3-D tumor models. *Materials today* **2015,** *18* (10), 539-553.

18. Stevenson, C. S.; Marshall, L. A.; Morgan, D. W., *In vivo models of inflammation*. Springer Science & Business Media: 2006; Vol. 2.

19. Park, H.-J.; Helfman, D. M., Up-regulated fibronectin in 3D culture facilitates spreading of triple negative breast cancer cells on 2D through integrin β-5 and Src. *Scientific reports* **2019,** *9* (1), 1-14.

20. Maity, G.; Choudhury, P. R.; Sen, T.; Ganguly, K. K.; Sil, H.; Chatterjee, A., Culture of human breast cancer cell line (MDA-MB-231) on fibronectin-coated surface induces pro-matrix metalloproteinase-9 expression and activity. *Tumor Biology* **2011,** *32*, 129-138.

21. Gong, X.; Lin, C.; Cheng, J.; Su, J.; Zhao, H.; Liu, T.; Wen, X.; Zhao, P., Generation of multicellular tumor spheroids with microwell-based agarose scaffolds for drug testing. *PloS one* **2015,** *10* (6), e0130348.

22. Zanoni, M.; Piccinini, F.; Arienti, C.; Zamagni, A.; Santi, S.; Polico, R.; Bevilacqua, A.; Tesei, A., 3D tumor spheroid models for in vitro therapeutic screening: a systematic approach to enhance the biological relevance of data obtained. *Scientific reports* **2016,** *6*, 19103.

23. Amaral, R. L.; Miranda, M.; Marcato, P. D.; Swiech, K., Comparative Analysis of 3D Bladder Tumor Spheroids Obtained by Forced Floating and Hanging Drop Methods for Drug Screening. *Frontiers in physiology* **2017,** *8*, 605.

24. Hong, X.; Chedid, K.; Kalkanis, S. N., Glioblastoma cell line-derived spheres in serum-containing medium versus serum-free medium: A comparison of cancer stem cell properties. *International journal of oncology* **2012,** *41* (5), 1693-1700.

25. Terashima, J.; Sampei, S.; Iidzuka, M.; Ohsakama, A.; Tachikawa, C.; Satoh, J.; Kudo, K.; Habano, W.; Ozawa, S., VEGF expression is regulated by HIF-1α and ARNT in

3D KYSE-70, esophageal cancer cell spheroids. *Cell biology international* **2016,** *40* (11), 1187-1194.

26. Mishriki, S.; Fattah, A. A.; Kammann, T.; Sahu, R.; Geng, F.; Puri, I., Rapid Magnetic 3D Printing of Cellular Structures with MCF-7 Cell Inks. *Research* **2019,** *2019*, 9854593.

27. Fattah, A. R. A.; Mishriki, S.; Kammann, T.; Sahu, R. P.; Geng, F.; Puri, I. K., 3D cellular structures and co-cultures formed through the contactless magnetic manipulation of cells on adherent surfaces. *Biomaterials science* **2018,** *6* (3), 683-694.

28. Fattah, A. R. A.; Mishriki, S.; Kammann, T.; Sahu, R. P.; Geng, F.; Puri, I. K., Gadopentatic acid affects in vitro proliferation and doxorubicin response in human breast adenocarcinoma cells. *BioMetals* **2018**, 1-12.

29. Abdel Fattah, A. R.; Meleca, E.; Mishriki, S.; Lelic, A.; Geng, F.; Sahu, R. P.; Ghosh, S.; Puri, I. K., In Situ 3D Label-Free Contactless Bioprinting of Cells Through Diamagnetophoresis. *ACS Biomaterials Science & Engineering* **2016**.

30. Anil-Inevi, M.; Yaman, S.; Yildiz, A. A.; Mese, G.; Yalcin-Ozuysal, O.; Tekin, H. C.; Ozcivici, E., Biofabrication of in situ Self Assembled 3D Cell Cultures in a Weightlessness Environment Generated using Magnetic Levitation. *Scientific reports* **2018,** *8* (1), 7239.

31. Rama-Esendagli, D.; Esendagli, G.; Yilmaz, G.; Guc, D., Spheroid formation and invasion capacity are differentially influenced by co-cultures of fibroblast and macrophage cells in breast cancer. *Molecular biology reports* **2014,** *41* (5), 2885-2892.

32. Place, A. E.; Huh, S. J.; Polyak, K., The microenvironment in breast cancer progression: biology and implications for treatment. *Breast Cancer Research* **2011,** *13* (6), 227.

33. Jeong, S.-Y.; Lee, J.-H.; Shin, Y.; Chung, S.; Kuh, H.-J., Co-culture of tumor spheroids and fibroblasts in a collagen matrix-incorporated microfluidic chip mimics reciprocal activation in solid tumor microenvironment. *PloS one* **2016,** *11* (7), e0159013.

34. Rajah, T. T.; Rambo, D. J.; Dmytryk, J. J.; Pento, J. T., Influence of antiestrogens on NIH-3T3-fibroblast-induced motility of breast cancer cells. *Chemotherapy* **2001,** *47* (1), 56-69.

35. Mah, E. J.; Lefebvre, A. E.; McGahey, G. E.; Yee, A. F.; Digman, M. A., Collagen density modulates triple-negative breast cancer cell metabolism through adhesion-mediated contractility. *Scientific reports* **2018,** *8* (1), 17094.

36. Fernandes, I. R.; Russo, F. B.; Pignatari, G. C.; Evangelinellis, M.; Tavolari, S.; Muotri, A. R.; Beltrão-Braga, P. C. B., Fibroblast sources: Where can we get them? *Cytotechnology* **2016,** *68* (2), 223-228.

37. Wei, S. C.; Yang, J., Forcing through tumor metastasis: the interplay between tissue rigidity and epithelial–mesenchymal transition. *Trends in cell biology* **2016,** *26* (2), 111-120.

38. Butcher, D. T.; Alliston, T.; Weaver, V. M., A tense situation: forcing tumour progression. *Nature Reviews Cancer* **2009,** *9* (2), 108-122.

39. Frantz, C.; Stewart, K. M.; Weaver, V. M., The extracellular matrix at a glance. *Journal of cell science* **2010,** *123* (24), 4195-4200.

40. Breslin, S.; O'Driscoll, L., Three-dimensional cell culture: the missing link in drug discovery. *Drug discovery today* **2013,** *18* (5-6), 240-249.

41. Studebaker, A. W.; Storci, G.; Werbeck, J. L.; Sansone, P.; Sasser, A. K.; Tavolari, S.; Huang, T.; Chan, M. W.; Marini, F. C.; Rosol, T. J., Fibroblasts isolated from common sites of breast cancer metastasis enhance cancer cell growth rates and invasiveness in an interleukin-6–dependent manner. *Cancer research* **2008,** *68* (21), 9087-9095.

42. Dvorak, K. M.; Pettee, K. M.; Rubinic-Minotti, K.; Su, R.; Nestor-Kalinoski, A.; Eisenmann, K. M., Carcinoma associated fibroblasts (CAFs) promote breast cancer motility by suppressing mammalian Diaphanous-related formin-2 (mDia2). *PloS one* **2018,** *13* (3).

43. Türker, E.; Demirçak, N.; Arslan-Yildiz, A., Scaffold-free three-dimensional cell culturing using magnetic levitation. *Biomaterials Science* **2018**.

44. Bartolini, M.; Pekar, J.; Chettle, D.; McNeill, F.; Scott, A.; Sykes, J.; Prato, F.; Moran, G., An investigation of the toxicity of gadolinium based MRI contrast agents using neutron activation analysis. *Magnetic resonance imaging* **2003,** *21* (5), 541-544.

45. Gräfe, J. L.; McNeill, F. E., Measurement of gadolinium retention: current status and review from an applied radiation physics perspective. *Physiological measurement* **2018,** *39* (6), 06TR01.

46. Aime, S.; Caravan, P., Biodistribution of gadolinium-based contrast agents, including gadolinium deposition. *Journal of Magnetic Resonance Imaging: An Official Journal of the International Society for Magnetic Resonance in Medicine* **2009,** *30* (6), 1259-1267.

47. Noseworthy, M. D.; Ackerley, C.; Qi, X.; Wright, G. A., Correlating subcellular contrast agent location from dynamic contrast-enhanced magnetic resonance imaging (dMRI) and analytical electron microscopy. *Academic radiology* **2002,** *9* (2), S514-S518.

48. Wang, J.; Liu, J.; Liu, Y.; Wang, L.; Cao, M.; Ji, Y.; Wu, X.; Xu, Y.; Bai, B.; Miao, Q., Gd-Hybridized Plasmonic Au-Nanocomposites Enhanced Tumor-Interior Drug Permeability in Multimodal Imaging-Guided Therapy. *Advanced Materials* **2016,** *28* (40), 8950-8958.

49. Allen, M. J.; MacRenaris, K. W.; Venkatasubramanian, P.; Meade, T. J., Cellular delivery of MRI contrast agents. *Chemistry & biology* **2004,** *11* (3), 301-307.

50. Zhang, W.; Li, C.; Baguley, B. C.; Zhou, F.; Zhou, W.; Shaw, J. P.; Wang, Z.; Wu, Z.; Liu, J., Optimization of the formation of embedded multicellular spheroids of MCF-7 cells: How to reliably produce a biomimetic 3D model. *Analytical biochemistry* **2016,** *515*, 47-54.

51. Charoen, K. M.; Fallica, B.; Colson, Y. L.; Zaman, M. H.; Grinstaff, M. W., Embedded multicellular spheroids as a biomimetic 3D cancer model for evaluating drug and drug-device combinations. *Biomaterials* **2014,** *35* (7), 2264-2271.

52. Gencoglu, M. F.; Barney, L. E.; Hall, C. L.; Brooks, E. A.; Schwartz, A. D.; Corbett, D. C.; Stevens, K. R.; Peyton, S. R., Comparative study of multicellular tumor spheroid formation methods and implications for drug screening. *ACS biomaterials science & engineering* **2017,** *4* (2), 410-420.

53. Shoval, H.; Karsch-Bluman, A.; Brill-Karniely, Y.; Stern, T.; Zamir, G.; Hubert, A.; Benny, O., Tumor cells and their crosstalk with endothelial cells in 3D spheroids. *Scientific reports* **2017,** *7* (1), 10428.

54. Walzl, A.; Unger, C.; Kramer, N.; Unterleuthner, D.; Scherzer, M.; Hengstschläger, M.; Schwanzer-Pfeiffer, D.; Dolznig, H., The resazurin reduction assay can distinguish cytotoxic from cytostatic compounds in spheroid screening assays. *Journal of biomolecular screening* **2014,** *19* (7), 1047-1059.

55. Vinci, M.; Gowan, S.; Boxall, F.; Patterson, L.; Zimmermann, M.; Lomas, C.; Mendiola, M.; Hardisson, D.; Eccles, S. A., Advances in establishment and analysis of three-dimensional tumor spheroid-based functional assays for target validation and drug evaluation. *BMC biology* **2012,** *10* (1), 29.

56. Saleh, F.; Whyte, M.; Genever, P., Effects of endothelial cells on human mesenchymal stem cell activity in a three-dimensional in vitro model. *Eur Cell Mater* **2011,** *22* (242), e57.

57. Tocchio, A.; Durmus, N. G.; Sridhar, K.; Mani, V.; Coskun, B.; El Assal, R.; Demirci, U., Magnetically guided self-assembly and coding of 3D living architectures. *Advanced Materials* **2018,** *30* (4), 1705034.

58. Foty, R. A.; Pfleger, C. M.; Forgacs, G.; Steinberg, M. S., Surface tensions of embryonic tissues predict their mutual envelopment behavior. *Development* **1996,** *122* (5), 1611-1620.

59. Foty, R. A.; Steinberg, M. S., The differential adhesion hypothesis: a direct evaluation. *Developmental biology* **2005,** *278* (1), 255-263.

60. Lewis, N. S.; Lewis, E. E.; Mullin, M.; Wheadon, H.; Dalby, M. J.; Berry, C. C., Magnetically levitated mesenchymal stem cell spheroids cultured with a collagen gel maintain phenotype and quiescence. *Journal of tissue engineering* **2017,** *8*, 2041731417704428.

61. Turker, E.; Arslan-Yildiz, A., Recent Advances in Magnetic Levitation: A Biological Approach from Diagnostics to Tissue Engineering. *ACS Biomaterials Science & Engineering* **2018,** *4* (3), 787-799.

62. Akiyama, Y.; Morishima, K. In *Label-free ultrarapid spheroid formation in microfluidic chip using magneto-Archimedes effect*, Micro Electro Mechanical Systems (MEMS), 2012 IEEE 25th International Conference on, IEEE: 2012; pp 116-119.

63. Akiyama, Y.; Morishima, K., Label-free cell aggregate formation based on the magneto-Archimedes effect. *Applied Physics Letters* **2011,** *98* (16), 163702.

64. Gao, Q.-H.; Zhang, W.-M.; Zou, H.-X.; Li, W.-B.; Yan, H.; Peng, Z.-K.; Meng, G., Label-free manipulation via the magneto-Archimedes effect: fundamentals, methodology and applications. *Materials Horizons* **2019**.

65. Shahin-Shamsabadi, A.; Selvaganapathy, P. R., A rapid biofabrication technique for self-assembled collagen-based multicellular and heterogeneous 3D tissue constructs. *Acta biomaterialia* **2019,** *92*, 172-183.

66. Healy, L.; Ruban, L., Mouse and Human Fibroblasts. In *Atlas of Human Pluripotent Stem Cells in Culture*, Springer US: Boston, MA, 2015; pp 3-18.

67. Taubman, M. B.; Goldberg, B., The processing of procollagen in cultures of human and mouse fibroblasts. *Archives of biochemistry and biophysics* **1976,** *173* (2), 490-494.

68. Wang, L.; Liu, H.; Jiao, Y.; Wang, E.; Clark, S. H.; Postlethwaite, A. E.; Gu, W.; Chen, H., Differences between mice and humans in regulation and the molecular network of collagen, type III, alpha-1 at the gene expression level: obstacles that translational

research must overcome. *International journal of molecular sciences* **2015,** *16* (7), 15031-15056.

6 3D Cellular Structures and Co-Cultures Formed through Contactless Magnetic Manipulation of Cells on Adherent Surfaces

This chapter is reproduced from *3D cellular structures and co-cultures formed through contactless magnetic manipulation of cells on adherent surfaces, 2(12), 2133-2138, 2016, RSC Biomaterials Science, Abdel Fattah Abdel Rahman,* ***Sarah Mishriki****, Tobias Kammann, Rakesh P. Sahu, Fei Geng, and Ishwar K. Puri, https://doi.org/10.1039/C7BM01050H.* The author of this thesis co-authored this publication with AA, who each contributed equally to the work. SM conceptualized the use of co-culture, observed unique 2.5D geometries of cells printed with magnetic assistance on adherent surfaces, conducted cellular experiments, and contributed to writing of the manuscript.

6.1 Abstract

A magnet array is employed to manipulate diamagnetic cells that are contained in paramagnetic medium to demonstrate for the first time the contactless bioprinting of three-dimensional (3D) cellular structures and co-cultures of breast cancer MCF-7 and endothelial HUVEC at prescribed locations on tissue culture treated well plates. Sequential seeding of different cell lines and spatial displacement of the magnet array creates co-cultured cellular structures within a well without using physically intrusive well inserts. Both monotypic and co-culture experiments produce morphologically rich 3D cell structures that are otherwise absent in regular monolayer cell cultures. The magnetic contactless bioprinting of cells provides further insight into cell behaviour, invasion

strategies and transformations that are useful for potential applications in drug screening, 3D cell culture formation and tissue engineering.

6.2 Introduction

Under normal physiological conditions, tumor cells coexist with benign and other cell types, which can influence *in vivo* tumor microenvironments and tumor drug response. Attempts to simulate and represent these responses by conducting tests on monotypic monolayers *in vitro* skews expected results.[1] Cell manipulation techniques have been extended to *in vitro* co-culture experiments to better mimic *in vivo* conditions[2, 3], e.g. to demonstrate increased angiogenic potential and phenotypic modification[4], and increased invasiveness of MCF-7 cells.[5] These techniques can also change cell states, which in turn significantly alter cell response, e.g. to drugs such as doxorubicin[6, 7], by exhibiting phenotypic heterogeneity of quiescent and malignant cells.[6] Thus, cell manipulation during synthetic experiments enables the predesigned formation of cellular structures in which cell-cell interactions can be observed in different environments.

Cell manipulation techniques depend on procedures[2, 8] that position different cell types at specific locations to observe their interactions. For example, transwell models are able to mimic *in vivo* conditions of the blood-brain barrier[9], while scaffolds[10] and hydrogels[11] are used as structural supports to promote co-cultures. Microfluidics methods depend on channel geometry to guide cells to specific positions in a controlled manner[8], e.g., for investigating microbial interactions[12], single cell co-cultures[13], cell migration[14], and to create organ on chip devices.[15]

Cell manipulation generally involves multistep processes, that increase complexity, which hinders their adoption.[16] Setups usually require that physically intrusive inserts be placed directly into the cell culture environment. While magnetic cell manipulation does not require such inserts, it often uses magnetic nanoparticles as cell inclusions[17, 18], raising the risk of damage to the cellular membrane. As an alternative, the difference between the magnetic susceptibilities of diamagnetic cells and their surrounding paramagnetic medium can be leveraged to move cells to regions where they experience lower magnetic field strengths[19, 20], thus separating cells from the surrounding medium[21] and clustering them together.[22, 23] The spatial influence of magnetic arrays designed to intensify magnetic fields and thus influence cell separation[23], e.g., to form spheroids on non-adherent surfaces[24], can be enhanced by increasing the paramagnetic susceptibility of the culture medium.[25, 26]

We have previously shown that macroscale 3D cellular structures are produced in various shapes with differently oriented magnet arrays that are able to influence a label free suspension of non-adherent diamagnetic whole blood cells in a paramagnetic buffer.[27] Here, using paramagnetic medium, we extend that approach to manipulate adherent cell lines using breast cancer cells (Michigan Cancer Foundation-7, MCF-7) and human umbilical vein endothelial cells (HUVECs) that are placed on common adherent tissue cultured treated (TCT) surfaces. A schematic is provided in **Figure 6.1**. Although epithelial breast tumor and endothelial cell exist *in vivo*[28], the main purpose of using these specific cell lines is to demonstrate and the capabilities of magnetic printing. Cross-talk between these cell types is important in tumor studies. The label-free cells are magnetically manipulated into 3D monotypic and co-culture cellular structures on well plates. The

method requires no supplementary equipment other than the magnet array, does not use inserts, making it suitable for a variety of experimental procedures.

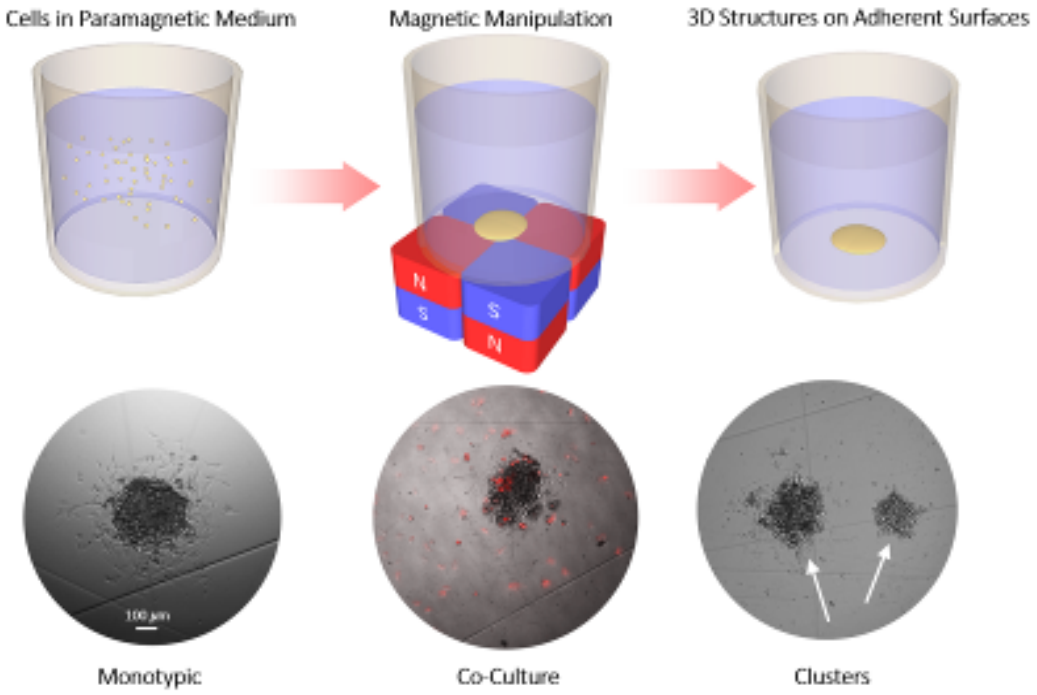

Figure 6.1: Schematic for magnetic cell manipulation on adherent surfaces. Label-free cell magnetic manipulations facilitate fast and new experimental setups and reveal novel observations in synthetic biology.

6.3 Results and discussion

Adding paramagnetic gadopentatic acid (Gd-DTPA, 25mM), a common magnetic resonance imaging contrast agent, to regular DMEM medium with 10% FBS, increased its overall magnetic susceptibility, rendering the medium paramagnetic. The magnetic susceptibility of the medium was thus $\chi_m > 0$ while that of a cell $\chi_c < 0$, since it was diamagnetic. The magnet array was assembled into 96 blocks, each consisting of 4

individual neodymium N52 grade 3.175 mm cube magnets. The block configuration localized a spatial region of lowest magnetic field strength that was deliberately aligned within the wells of a 96 or a 384 well plate. Since $(\chi_c - \chi_m) < 0$, the cells in a settling suspension were guided to this region of lowest magnetic field strength where they clustered, aggregated, and adhered to each other and the plate surface. Following an incubation period under the magnetic field the paramagnetic medium was replaced with fresh regular culture medium, eliminating further exposure of the cells to the paramagnetic salt, since prolonged exposure to the salt can be toxic.[24] An MTT assay was performed to assess cell viability, see **Figure 6.2**. Compared to **Figure 4.1**, **Figure 6.2** indicates less toxicity to paramagnetic medium (25 mM Gd-DTPA) after 24 hours of exposure. This discrepancy can be attributed to the different cell numbers at t_0: 1000 cells/well versus 500 cells/well, respectively. Although the 96-well plates where the MTT assay was performed in has a capacity of approximately 40,000 cells, increased confluency of cells in **Figure 4.1** can contribute to decreased proliferation.[29] Based on absorbance values and a standard curve, a control normalized percent viable cell evaluation showed no significant difference between cells cultured in medium containing 25 mM Gd-DTPA and a Gd-DTPA free medium control. This suggested that a medium replacement at 6 h does not negatively impact the cells. The 3D structures can be created in a monotypic environment, on top of another monolayer of a different cell line, or by spatially moving the magnetic field, be co-cultured with other 3D cellular structures, as shown in **Figure 6.3**.

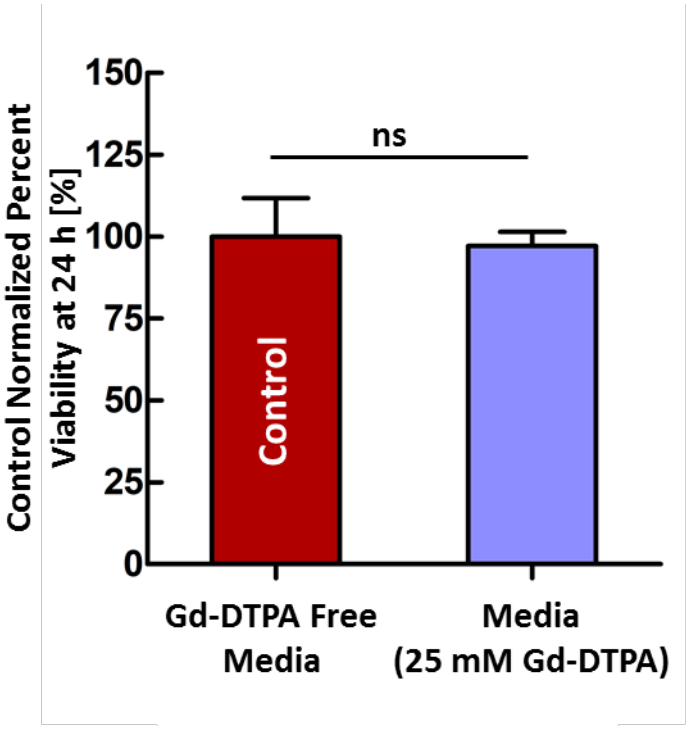

Figure 6.2: MTT assay displayed percent viable cells for MCF-7 cells cultured in medium containing 0 mM and 25 mM Gd-DTPA for 24 h. The control normalized percent viable cells of MCF-7 cells cultured in medium containing 25 mM Gd-DTPA yielded no significant difference when compared to the control case over the course of 24 h. This mitochondrial metabolic analysis suggests that a change from a paramagnetic medium to a Gd-DTPA-free medium at t = 6 h has a negligible impact on cells.

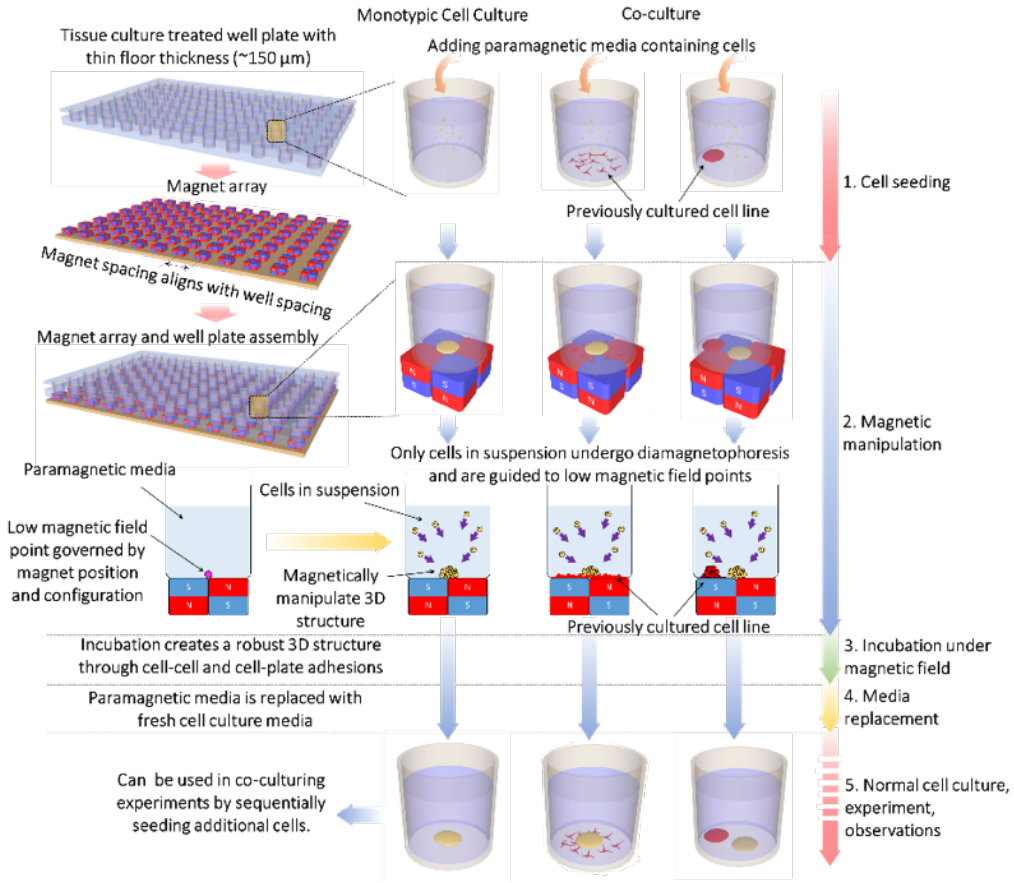

Figure 6.3: Macroscale magnetic manipulation of cells. Cells are seeded into wells containing paramagnetic medium with a 25 mM Gd-DTPA concentration. The wells can contain either previously cultured monolayers or magnetically manipulated cells. Under the influence of a magnetic, where S (blue) and N (red) respectively denote the south and north poles of the magnet, cells in suspension behave diamagnetically and aggregate in regions of low magnetic field strength. These locations are determined by the relative positions of the magnet array and the well plate. As they aggregate, cells are incubated while still under the influence of the magnetic field, creating a robust 3D cellular structure through cell-

cell and cell-plate adhesion. The paramagnetic medium is then replaced with fresh culture medium with minimum disruption to the 3D cell structure. This readily adoptable method facilitates cell monotypic and co-culture experiments and promotes phenotypic changes in cells, while forgoing physical well inserts.

To investigate the effect of full medium change after magnetic manipulation, 2,000 MCF-7 cells are first manipulated for 1, 3, and 6 h prior to the medium change. **Figure 6.4** presents micrographs before and after the medium change for these three manipulation durations. After cells have been incubated for 1 and 3 h with a magnetic field, the medium change disturbs the 3D structures significantly, leaving only monolayer cells behind. Cells incubated for 3 h are allowed to adhere to the surface over a longer duration, which prevents them from being washed away. Hence, the 3 h samples contain more monolayer cells than those incubated for 1 h. In contrast, cells incubated for 6 h have their 3D morphologies relatively undisturbed after a medium change. Since longer incubation leads to more robust structures, these are able to better withstand wash away forces due to the medium change. Therefore, the 6h incubation time is selected for cases where the medium must be fully changed.

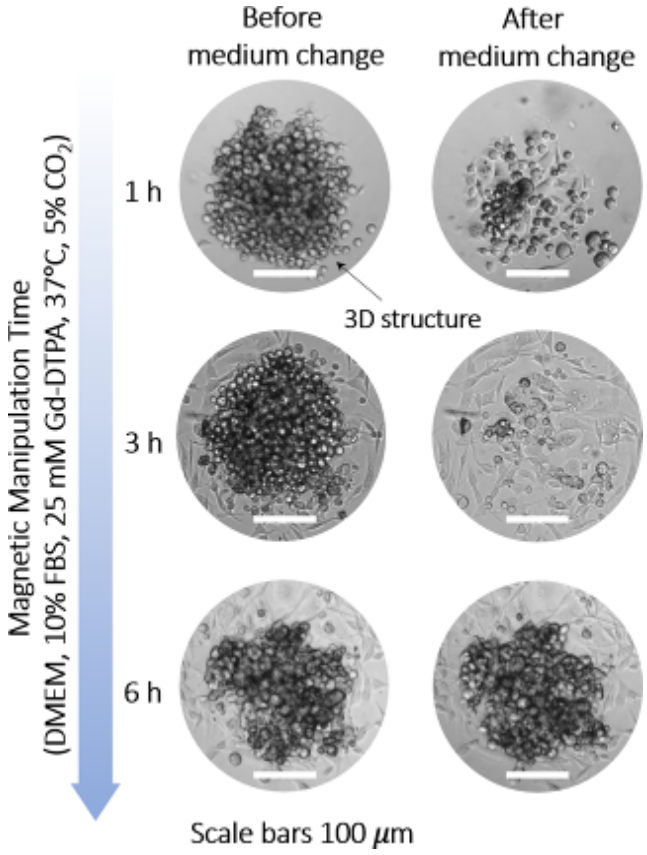

Figure 6.4: Optimization of the magnetic manipulation time. 2,000 MCF-7 cells are magnetically manipulated and incubated for 1, 3, and 6 h, before the medium is changed, i.e., the paramagnetic culture is replaced with a Gd-DTPA free medium. The medium change imposes wash away forces on the magnetically facilitated 3D structures for each case. When the manipulation occurs over 1 and 3 h, the 3D structures are washed away, presumably due to a lack of firm cell-cell adhesion for those incubation durations. When cells are magnetically manipulated over a longer 6 h period, the 3D structures are less disturbed after medium change. Therefore, when a full medium change is required, an incubation time lower than 6 h is not recommended for MCF-7 cells.

We demonstrated how MCF-7 cells were magnetically manipulated into 3D cellular structures while undergoing cell growth along the well floor in **Figure 6.5**. Each experiment was repeated 4 times. MCF-7 cells were first suspended in paramagnetic medium (DMEM, 10% FBS, 25 mM of Gd-DTPA). 2,000 MCF-7 cells were seeded in the microwells of a 384 well plate and placed on the magnet array. As a negative control, cells were also plated in a monolayer under the same conditions using a Gd-DTPA free medium. When cells were magnetically manipulated, they were cultured for 6 hours under the influence of the magnetic field, which facilitated the formation of 3D cellular structures. After 6 hours of incubation, cell-cell and cell-plate adhesions were formed. Then, the paramagnetic medium was replaced with fresh Gd-DTPA free medium without impacting the integrity of the cellular structures. At time t = 6 h, the central 3D cellular structure was surrounded by monolayer cells, highlighted by black dashed circles, which formed the rim of an expanding cellular front, as shown in **Figure 6.5**(**a**). At t = 24 h, 3D protrusions, highlighted by the solid black line, emerged from the central structure. These protrusions have been shown to be rich in F-actin in previous studies,[30] and are not unique to magnetic printing. Patches of dense monolayer cells, highlighted by the dotted black line, surrounded the 3D structure. At t = 48 h, monolayer cells migrated further away from the central structure. At t = 72 h, the protrusions continued to grow and the 3D central structure was surrounded by expanding dense monolayer cells, but the monolayer cells had by then migrated outside the field of view. Cells cultured in the absence of magnets and paramagnetic medium did not reveal 3D protrusions and exhibited regular and dense monolayer features. The dense

features, characteristic of MCF-7 cells, did not surround specific cellular structures and were randomly scattered, unlike cells that were magnetically manipulated.

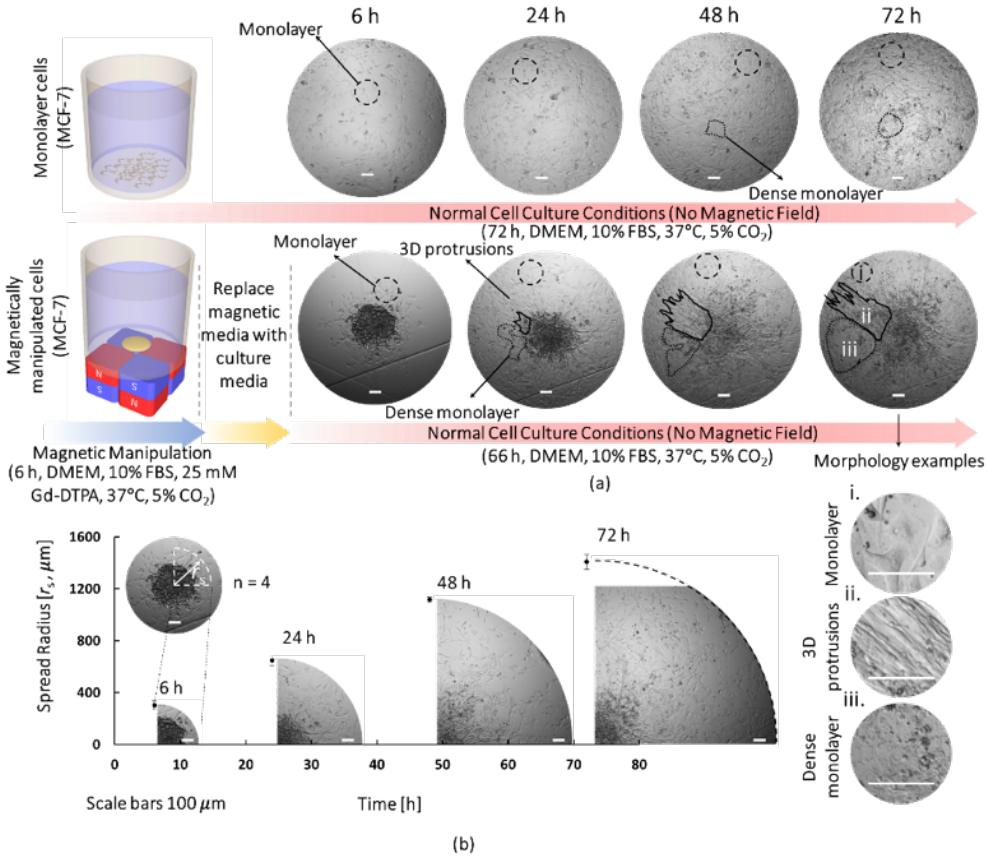

Figure 6.5: Magnetic manipulation of MCF-7 cells for monotypic cell culture. (**a**) 2,000 MCF-7 cells were cultured in a monolayer and an equal number of cells were magnetically manipulated to form 3D structures following a 6 hour incubation in paramagnetic medium and the presence of a magnet (the magnets were removed at t = 6 h). In both cases, the cells were observed over 72 hours in a 384 well plate. For the monolayer case, dense monolayer clusters appeared at t = 48 h highlighted in black dashed line. When cells were magnetically manipulated, 3D central

structures were produced from which 3D cell projections, which were malignant transformations, became evident. Dense monolayer cells were evident at t = 24 h and continually expanded radially from the central structure along with other monolayer cells. (**b**) The radial spread of cells was due to cell migration and mobility through the environment. The spread was measured from the center of the cell covered area to the perimeter rim outlined by the monolayer cells. MCF-7 spread was quasi linear and at t = 72 h, almost reached the well wall. Thus, magnetic manipulation of cells in this experiment triggered morphological changes and exposed interesting cell behavior related to cell malignancy and motility.

By spatially concentrating cells with a magnetic field, the measurement of cell spread, thus their mobility, was possible. We measured the diameter of the rim created by monolayer cells at the perimeter of cell spread, see **Figure 6.5**(**b**). The cell spread rate decreased slightly over time. At t = 72 h, the cells covered almost the entirety of the well. As shown in **Figure 6.5**(**a**), the control experiment conducted without the magnetic field could not provide mobility information.

Cell migration from the initial 3D central cellular structure is likely related to MCF-7 motility, and competition for space due to the local increase in cell density produced by magnetic focusing. This cell clustering induces a different local environmental change of increased confluency and cell signaling, which likely contributes to the observed morphological change shown in **Figure 6.5** that suggests phenotypic transformations. The different morphologies encountered when cells were magnetically manipulated in **Figure 6.5**(**a**) are (1) dense monolayer regions, which resembled epithelial-like behaviour[31],

characteristic of MCF-7 cells, and 2) migrating monolayer cells and 3) 3D protrusions, both suggesting migratory transformations. The dense monolayer cells and migrating monolayer cells were likely related to the MCF-7 epithelial and migratory like behaviours, respectively.[31-32] Such behaviors revealed that magnetic cell manipulation is a facile method to trigger diverse morphologically heterogeneous MCF-7 cell cultures as a result of invasiveness, growth patterns, and collective behaviour, unlike randomly scattered cell seeding encountered in non-magnetically manipulated cultures.

The methodology also provided co-culture capability. In this context, we cultured MCF-7 cells along with a HUVEC monolayer for 3 days, with the experiment being repeated 4 times. 5,000 red fluorescent protein positive (RFP+) HUVECs were seeded and cultured for 24 h in a 384 TCT well plate in HUVEC culture medium. Subsequently, the medium was removed and replaced with paramagnetic medium and the well plate was placed on a magnetic array. Then, 2,000 MCF-7 cells were seeded in the culture and incubated for 6 hours, after which the medium was replaced with fresh Gd-DTPA free culture medium (DMEM, 10% FBS) and left to incubate until t = 72 h. Although HUVECs were subjected to the same magnetic force used to focus MCF-7 cells, they adhered to the well floor and were thus stationary. Only the MCF-7 cells, which were still in suspension, underwent diamagnetophoresis to form a 3D structure.

Figure 6.6(a) shows that at t = 6 h, magnetically focused MCF-7 cells localized HUVECs around them, which may have occurred due to cell-cell interactions between the two cell lines. Monolayer MCF-7 cells were also observed surrounding the central structure, while other monolayer HUVECs were scattered throughout the field of view. A

HUVEC only control is observed for comparison. At t = 24 h, similar to its monotypic counterpart in **Figure 6.5**(**a**)**,** evidence of 3D cell protrusions and dense monolayer cells, are highlighted in black solid and dotted lines, respectively. However, these protrusions are smaller than those in **Figure 6.5**(**a**), which suggests slower migration. At t = 48 h, cells continued to spread radially, denser monolayer patches were seen, but the 3D protrusions grew more slowly than those shown in **Figure 6.5**(**a**). At t = 72 h, the dense monolayer regions continued to merge and grow but the 3D protrusions appeared to have ceased their growth. The densely packed cells appeared to be devoid of HUVECs, the cell count for which continually reduced in the face of an advancing MCF-7 front. This loss of HUVECs was observed through a reduction in RFP+ cells over time and possibly occurred due to a competition with invasive MCF-7 cells.

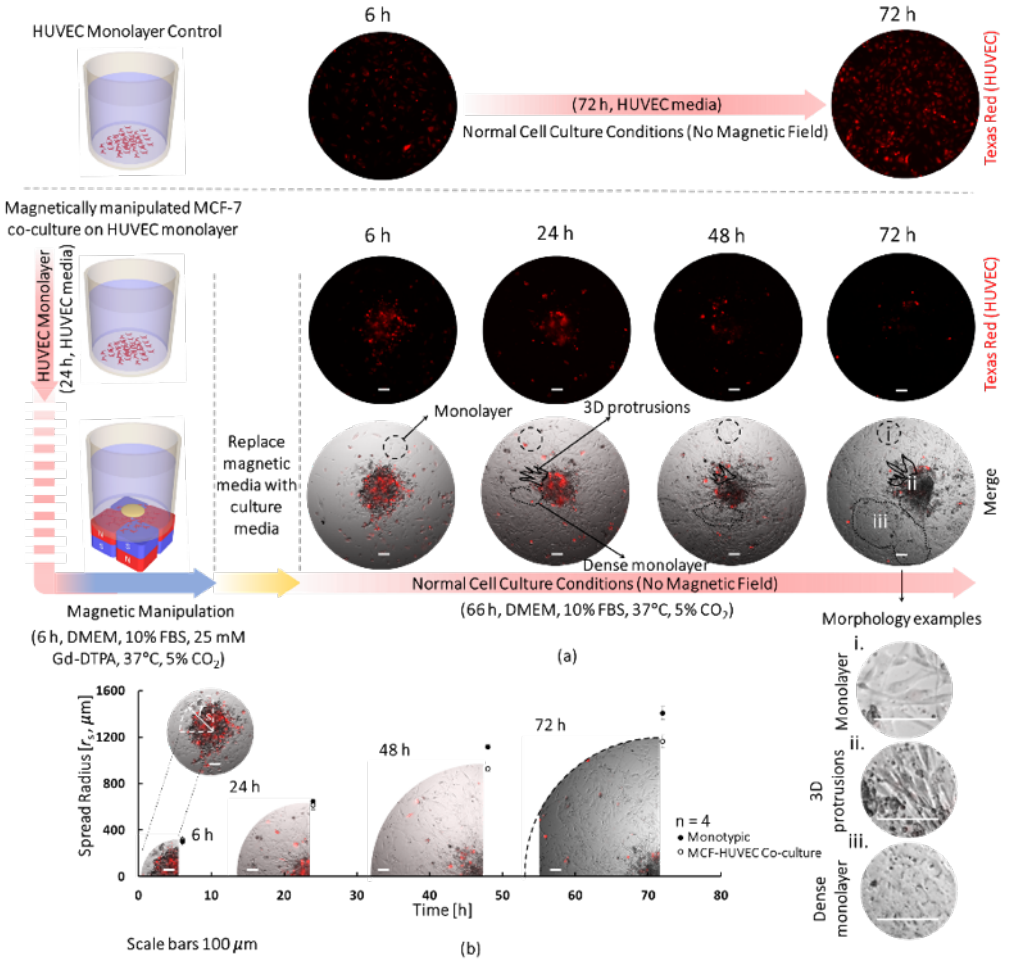

Figure 6.6: Co-culture of magnetically manipulated MCF-7 cells on a monolayer of HUVECs. (**a**) A monolayer of 5,000 HUVECs was first cultured for 24 hours in HUVEC medium in a 384 well plate. A 5,000 HUVEC only monolayer control was observed for comparison. The HUVEC growth media was then replaced by paramagnetic media containing MCF-7 cells in suspension and the plate placed on the magnet array, when the MCF-7 migrated to the region of lowest magnetic field strength. Following 6 hours of incubation, the paramagnetic media was

replaced by fresh culture media. Through incubation over 72 h, MCF-7 cells migrated away from the 3D central cellular structure, forming multiple dense monolayer cell regions, as well as 3D cell projections, which were smaller than their monotypic counterpart. The dense monotypic regions seemed to be devoid of HUVECs, which reduced in numbers as a result of the advancing MCF-7 front. (**b**) The spread of MCF-7 cells across the well floor was slower than of its monotypic counterpart and may be related to the smaller 3D cell projections and presence of HUVECs in the environment.

Figure 6.6(**b**) depicts the spread of magnetically manipulated MCF-7 cells in the presence of a HUVEC monolayer over 72 h. Data representing cell spread for the monotypic experiment is also presented for comparison. While co-cultured MCF-7 cells expanded radially, their spread rate was slower than for the monotypic culture. The slowdown was attributed to the presence of scattered HUVECs on the well floor, which influenced the physiological gradient within the well and consequent cell-cell interactions, thus hindered MCF-7 cell mobility.

As they were magnetically manipulated, a phenotypically rich spectrum of MCF-7 cells resulted in both the monotypic and co-cultured cases, prompting a more detailed investigation over a longer 6 day time period. Similar to the co-culture experiment, 5,000 HUVEC cells were seeded and cultured for 24 h in a 384 well plate, followed by magnetically manipulating 1,000 MCF-7 cells for 6 h, after which the paramagnetic medium was replaced with fresh culture medium. The medium was again refreshed at 72 h. **Figure 6.7**(**a**) shows a central MCF-7 cellular structure residing in an area containing

scattered RFP+ HUVECs after medium replacement at t = 6 h. After 48 h, **Figure 6.7**(**b**) shows that cells migrated away from the central structure, forming both monolayer and dense monolayer cells, respectively, at the rim of cell spread and within the region surrounding the initial central structure. There were fewer 3D cell projections emerging from the central structure.

At t = 96 h, **Figure 6.7**(**c**) shows that the dense monolayer features continued to grow and expand. However, a new feature formed at this time in the form of a 3D ring, which is highlighted by the dashed yellow lines surrounding the dense monolayer region, separating it from regular migrating monolayer cells. The 3D ring had a similar morphology to the 3D protrusions of **Figure 6.5**(**a**) and **6.6**(**a**), but instead of radial growth it oriented tangentially to the contour highlighted by the yellow dashed lines. The ring structure became more organized and prominent at t = 96 h and thereafter. At t = 144 h, **Figure 6.7**(**d**) presents a live/dead stain that identifies the cell states. Several morphologies were observed, i.e., 1) the initial central cellular structure transformed into an enlarging elongated 3D cluster, 2) monolayer cells, consisting of mostly MCF-7 cells and few HUVECs, 3) a dense monolayer of MCF-7 cells that surrounded the initial central structure that was largely devoid of HUVECs, 4) a 3D ring of MCF-7 cells surrounding the dense monolayer cells, and 5) spheroids formed on top of the dense monolayer cells. A HUVEC only control is presented in **Figure 6.7**(**e**) and shows the continual growth of HUVECs.

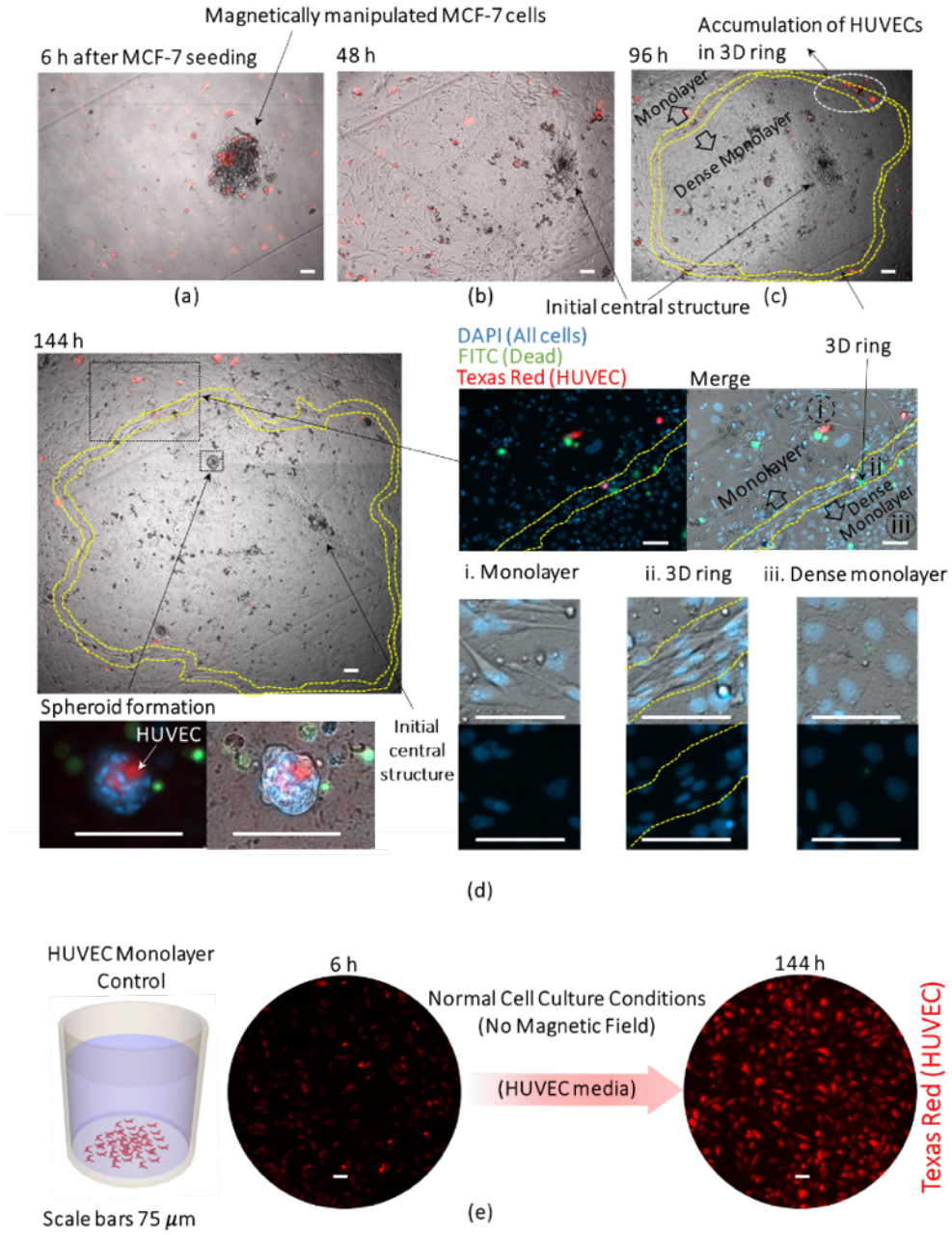

Figure 6.7: 6 day co-culture of magnetically manipulated MCF-7 cells on a HUVEC monolayer. MCF-7 cells were co-cultured with HUVECs in a similar manner to **Figure 6.4**. (**a**) At 6 h and after paramagnetic media change, MCF-7 cells

formed a 3D structure, which was surrounded by a monolayer of MCF-7 cells. (**b**) At t = 48 h, MCF-7 cells continued to expand radially, creating regions of monolayer and dense monolayer cells. (**c**) At t = 96 h, the central 3D structure was surrounded by dense monolayer cells, and a 3D ring of cells surrounded the dense monolayer cells. The ring cells were aligned tangentially to the perimeter of the dense monolayer cells and appeared to separate the latter from the monolayer cells found outside the ring. The expanding ring seemed to be devoid of dense HUVEC monolayers, and in some cases HUVECs were seen inside the ring structure. (**d**) At t = 144 h, the 3D ring became more organized. (**e**) A 5,000 HUVEC only monolayer control was observed for comparison. The monolayer and dense monolayer cells continued to expand radially. Spheroids were observed forming within the dense monolayer region and host HUVECs in their structure. The ring separated two morphologically distinct regions, 1) migrating monolayer cells and 2) dense monolayer cells.

Within the dense monolayer regions, there was little free space left, which was required for cell proliferation. Thus, expansion of these regions occurred at their peripheries and was attributed to the radially advancing 3D ring of cells. As the 3D MCF-7 ring moved radially, it collected HUVECs into its structure, which was evidenced by the concentration of HUVECs into the ring in **Figure 6.7**(**c**). Therefore, the dense monolayer MCF-7 cells located within the ring perimeter were largely devoid of HUVECs that once occupied that region. Similar to **Figures 6.4** and **Figure 6.6**, the dense monolayer region surrounded by the ring more closely resembled epithelial-like morphologies while migratory monolayer

cells were found outside the ring.[31-32] Hence, through loss of E-cadherin adhesion molecules and gain of migratory characteristics, epithelial cells can transition to mesenchymal migratory cells.[31-32] As it separated into the two morphologically distinct regions, i.e. dense and migratory monolayers, we speculate that the ring is a region where specific cell genomic transformations occurred, in this case epithelial-mesenchymal transitions (EMT)[32], which are often accompanied by morphological and behavioral transformations and cellular structure rearrangements.[33]

We also investigate the expression of N-Cadherin as a marker for cell mobility and as a preliminary indication of the transition to a more migratory phenotype.[34] After magnetically manipulating 2,000 MCF-7 cells on an adherent surface for 6h, incubation in a Gd-DTPA free medium over 72 h is followed by a cell fixation protocol. Subsequent immunohistochemistry reveals the expression of N-Cadherin in the monotypic cell culture.

N-Cadherin is expressed in the central structure, marked (**i**) in **Figure 6.8**. While the higher N-Cadherin expression arises due to the 3D structure, it also occurs as the constituent cells adopt a migratory behavior, as seen in **Figures 6.5**, **Figure 6.6**, and **Figure 6.7**. In the dense monolayer region, marked (**ii**) in **Figure 6.8**, N-Cadherin has minimum expression compared to other regions of the culture, suggesting the presence of a less migratory phenotype of MCF-7 cells. Within the same dense monolayer, there is a general and gradual increase in the expression of N-Cadherin for cells that lie closer to the circumference of the ring, marked (**iii**) in **Figure 6.8**. Along the ring and beyond it, marked (**iv**) in **Figure 6.8**, N-Cadherin is again generally expressed as the cells begin to separate

and migrate away in radial directions. The formation of a dense monolayer and the bias of cell movement is observed as a consequence of cell-substrate adhesions.[35]

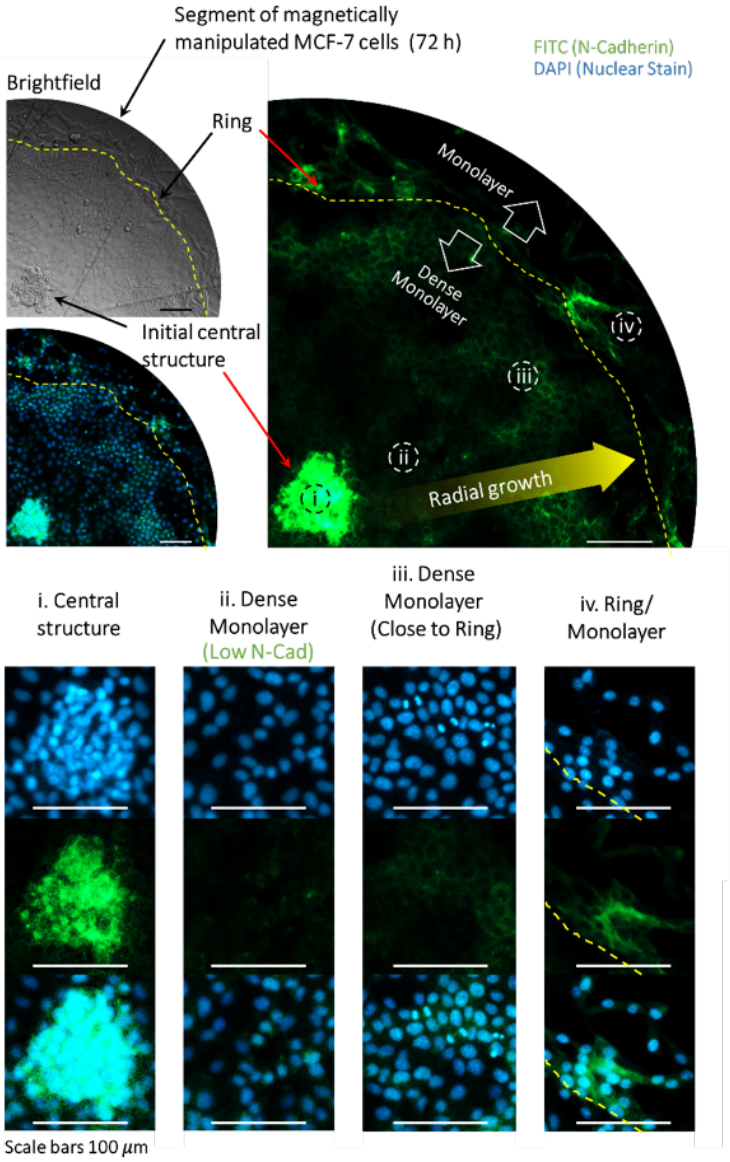

Figure 6.8: N-Cadherin expression in magnetically manipulated MCF-7 cells. 2,000 MCF-7 cells are magnetically manipulated in a paramagnetic medium for 6h, followed by a medium change and a 72 h incubation period, and then cell fixation.

Subsequent immunohistochemistry highlights the expression of N-Cadherin, which is expressed in the initial 3D central structure. The expression reaches a minimum for cells situated in the dense monolayer region between the central structure and the ring. Cells that lie further away from the central structure but close to the ring circumference exhibit a gradual increase in N-Cadherin expression, implying that these cells gain migratory characteristics. This migration allows cells along the ring, which also express N-Cadherin, to separate and migrate radially outward along the surrounding empty well floor.

These preliminary results support the possibility of the ring being a location for phenotypic transformation. Our investigation is limited to N-Cadherin. Hence, future work on possible phenotypic changes should also consider the expression of E-Cadherin. Besides, in addition to MCF-7 cells, co-cultures should also be compared in future, since other cells may influence cell behavior or impact phenotypic change.

Next, we co-cultured two different types of cells after magnetically manipulating them in the same well to form two separate 3D structures, see **Figure 6.9**(**a**). First, 2,000 MCF-7 cells were incubated for 3 h in paramagnetic medium under the influence of a magnetic field forming an initial structure. Subsequently, paramagnetic medium containing 1,000 HUVECs was added to the well. The sequential addition of HUVECs does not require a full medium change, but only the addition of the medium containing the cells. Hence, a 3 h incubation under the influence of a magnetic field is sufficient for the MCF-7 cells to form a robust 3D structure that is able to withstand the forces imposed by a magnet array shift. By displacing the magnetic array by a distance $d \approx 500\ \mu$m, the region of low magnetic

field strength was repositioned so that it is now off center from the MCF-7 cell structure. Although MCF-7 cells were also subjected to a body force in the direction of the displacement, they remained stationary due to their cell-cell and cell-plate adhesions. Therefore, only the diamagnetic HUVECs in suspension settled into a new 3D structure under the influence of the magnetic field, see **Figure 6.9(b)**. This differential cell positioning can thus be used to examine collocated populations of different cell types and their interactions. This capability of forming 3D cell structures of two different cell types in a single well can allow the observations of interactions which may not be apparent in 2D co-cultures.

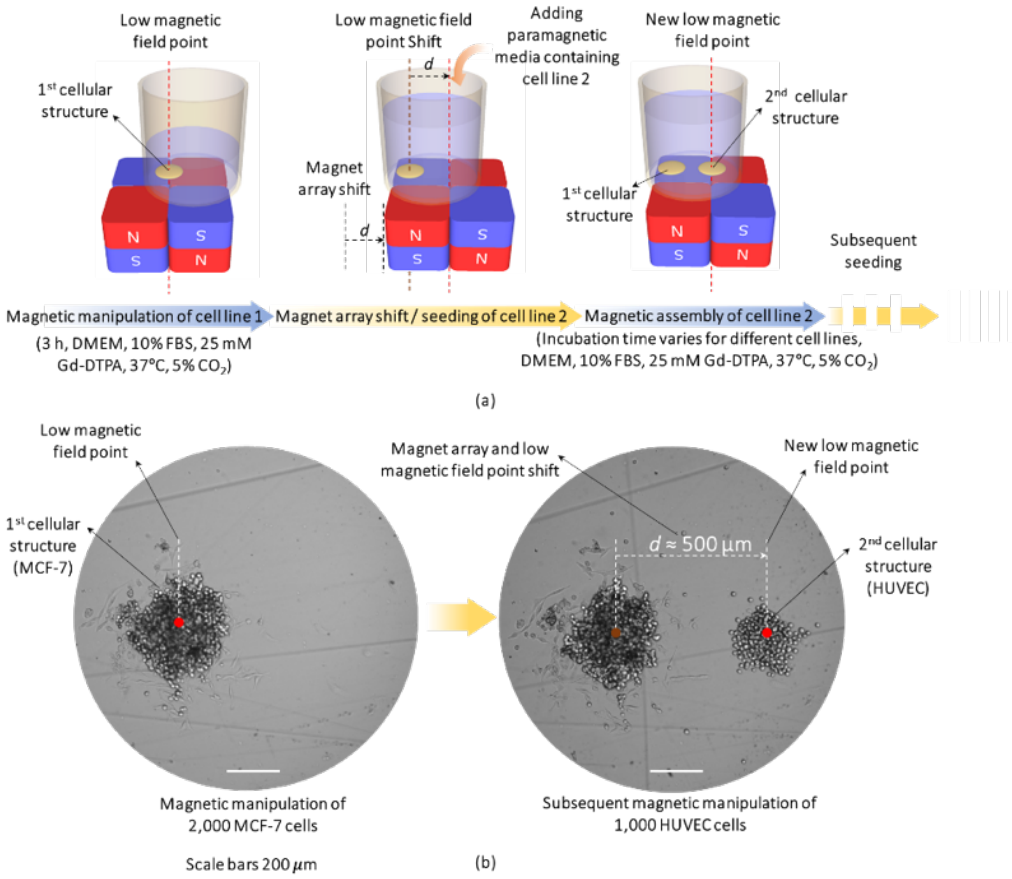

Figure 6.9: Two sequential magnetic manipulations of different cell lines. (**a**) The first cell line is cultured and forms an initial 3D structure. Since no medium change is required over such a short duration, after a 3 h incubation, the magnet array is displaced without influencing the first 3D structure, which relocates the region of low magnetic field strength within the well. Hence, when a second cell line is added to the well, another 3D central structure is formed at the new location of low field strength. Subsequent cell seeding can also follow sequentially. (**b**) 2,000 MCF-7 cells were first magnetically assembled and incubated for 3 h. The magnet array was displaced by $d \sim 500$ μm and 1,000 HUVECs in paramagnetic medium were seeded into the well. Although subject to a magnetic force, the adhered MCF-7 structure remained stationary. As a result, a second cellular structure of HUVECs was produced at the new location of the region of low magnetic field strength. This proof of concept demonstrated the ability to form autonomous 3D cellular structures within the same well, allowing for more elaborate co-culture conditions.

While this technique provided a facile route to readily manipulate and pattern cells directly into culture wells, further study can enhance the methodology. For example, the use of more intricate magnet configurations can provide additional options for achievable structures that are tailored to specific experimental needs, while incubation times between sequential cell seeding can be optimized for their impact on cell-cell and cell-plate adhesions.

6.4 Conclusions

We demonstrated for the first time the macroscale magnetic manipulation of adherent cells on tissue cultured treated surfaces. The method enabled morphological changes in monotypic and co-cultured cells. We examined the ability of MCF-7 cells to exhibit different morphological transformations and monitor their migration. Co-cultures were facilitated through the sequential seeding of cells, allowing the collocation and patterning of multiple cell types within the same environment. The loss of HUVEC over time can be controlled by changing the media to favor HUVEC maintenance. The technique forgoes well modifications, internal inserts and centrifugation steps, relying instead only on magnetic manipulation. The N-Cadherin expression in magnetically manipulated MCF-7 cells suggests that cells gain migratory characteristics near the ring structure, where they separate and migrate away from the remainder of the culture. While this study, limited only to N-Cadherin, suggests phenotypic changes related to observed morphologies, future investigation should combine both N- and E-Cadherin expressions in monotypic and co-culture settings, along with other markers. The diverse morphological spectrum facilitated by this manipulation revealed novel cell behaviors in both monotypic and co-cultured experiments, which could provide insight into cancer invasion, be used in drug response studies, and provided a platform for tissue engineering and organ-on-chip devices.

6.5 Materials and methods

Gadopentatic acid (Gd-DTPA) was obtained from Millipore Sigma (Diethylenetriaminepentaadetic acid gadolinium(III) dihydrogen salt hydrate, 97%,

381667). Dulbecco's modified eagle medium (DMEM), Rosewell Park Memorial Institute medium (RPMI) 1640, and fetal bovine serum (FBS) were purchased from ThermoFisher (DMEM – 12800082, RPMI 1640 – 31800089, FBS - 12484028). HEPES, L-Glutamine and Penicillin/Streptomycin were purchased from ThermoFisher (HEPES 1M – 15630080, L-Glutamine 200 mM 100X – 25030081, Penicillin/Streptomycin – 10,000 Units/mL Penicillin and 10,0000 μg/mL Streptomycin – 15140122). Trypsin-EDTA used for cell detachment from culture dishes was purchased from ThermoFisher (Trypsin-EDTA 1x, 0.25%, 25200056). Corning 384 culture well plates used for all experiments were purchased from Corning (384 tissue culture treated well plate, 4081). 100 mm culture dishes, used to culture cells were purchased from Corning (100 mm × 20 mm style dish, cell culture treated, nonpyrogenic, polystyrene, 430167). MTT (3-(4,5-dimethylthiazol-2-yl)-2,5-diphenyltetrazolium bromide) reagent was purchased from Invitrogen, Canada (cat# M6494). N-Cadherin antibody was generously supplied by Santa Cruz Biotechnology (N/R-Cadherin (H-4): sc-271386). Secondary fluorescent antibody was purchased from Thermofisher (Goat anti-Mouse IgG (H+L) Highly Cross-Adsorbed Secondary Antibody, Alexa Fluor 488, A-11029). N52 grade 3.175 mm cube magnets (Zigmyster Magnets, B18-N52) were used in the magnet array that was magnetically attached to a custom machined iron plate. This magnet dimension only allows for a maximum of 96 wells to be exposed to the magnetic field for spheroid printing. If desired, magnets with 4.5 mm cubed dimensions may be used in an array of 17×24 of alternating N-S orientation in order to occupy all wells of a 384-well plate and increasing scalability, as described in ***Chapter 5.5.3***. Trypan blue stain was used for cell counting purposes and was purchased from ThermoFisher (Trypan

blue stain 0.4%, 15250061). Neubauer Levy hemocytometer was used to count cells. A live/dead stain was used to differentiate between live and dead cells and purchased from Thermofisher (ReadyProbes Cell Viability Imaging Kit Blue/Green, R37609). Optical and fluorescence microscopy were performed using a Zeiss Axio Observer Z1 microscope.

The paramagnetic medium was prepared using DMEM supplemented with 10% FBS. Gd-DTPA powder was added to the medium and continuously stirred using a magnetic stirrer until it was completely dissolved to create a stock medium of 150 mM final concentration. Due to the presence of Gd-DTPA, NaOH must be added to quickly restore the resultant acidic medium to an isotonic pH of 7.4. The paramagnetic medium was finally created by diluting the stock medium to a lower concentration of 25 mM using DMEM supplemented with 10% FBS.

A 24 h MTT assay was performed to determine the effect of Gd-DTPA on cell viability. First 500 MCF-7 cells were plated and incubated in 100 μL medium containing 0 and 25 mM Gd-DTPA in 96-well tissue culture treated plates. At 24 hours, cell proliferation was analyzed by the MTT assay. A known number of cells were plated to produce a standard curve (0-1250 cells) to calibrate the MTT absorbance for quantification. The Tecan Infinite 200 Pro plate reader was used to obtain absorbance values. Following standard protocol given by the manufacturer, results were analyzed to obtain the control normalized percent viability (n = 3). Significance between the samples was determined using a two-tailed unpaired t test with a 95% confidence interval using GraphPad Prism version 5.01 for Windows, GraphPad Software, La Jolla California USA, www.graphpad.com.

MCF-7 cells were cultured in DMEM supplemented with 10% FBS in 100 mm tissue culture treated dishes. HUVECs were cultured in RPMI supplemented with 20% FBS, HEPES [10 mM], Pen/Strep [2 mM], and L-Glutamin [2 mM]. Cells were trypsinized at ~90% confluency into single cell suspensions before being seeded into wells. For a non-magnetically manipulated reference case and HUVEC monolayer, 1,000 - 5,000 cells per microwell were seeded. For the magnetically manipulated cases, the suspensions were adjusted with Gd-DTPA containing medium [150 mM] to provide a final Gd-DTPA concentration of 25 mM, and 1,000 - 2,000 cells per microwell were seeded. An incubation period of 3 to 6 hours was followed by a medium change to replace the paramagnetic medium with regular culture medium.

Immunohistochemistry was used to evaluate the expression of N-Cadherin in magnetically manipulated MCF-7 cells. First 2,000 MCF-7 cells were magnetically manipulated in a 386 well plate using paramagnetic medium with 25 mM Gd-DTPA. After a 6 h incubation period under the influence of a magnetic field, the medium was replaced with a Gd-DTPA free culture medium. After a 72 h incubation the cells were washed with PBS. A subsequent fixation step employed cold (-20°C) 100% methanol for 30 min at room temperature. The samples were washed with PBS, followed by addition of 1% BSA-PBS (w/v) and incubation for 30 min at room temperature. The solution was removed and the N-Cadherin primary antibody, diluted 1:100 in 1% BSA-PBS, was added to the fixated samples and incubated for 1 h at room temperature. The samples are subsequently triple washed using PBS and the secondary antibody, diluted 1:100 in 1% BSA-PBS, was added to the samples and incubated for 1 h at room temperature. After a triple wash with PBS, a

10 μL of DAPI nuclear stain was added to the samples and incubated for 15 min at room temperature. The samples were imaged using the bright field, DAPI and FITC channels on the Zeiss Axio Observer Z1 microscope. Exposure times were kept constant for comparative and qualitative evaluation fluorescence intensities.

6.6 Acknowledgements

Funding: This work was supported by Natural Sciences and Engineering Research Council of Canada (NSERC) Discovery Grant (RGPIN-2014-04066), Engage Grant (EGP 513882-17), Canada Foundation for Innovation John R. Evans Leaders Fund (CFI-JELF), Ontario Research Fund Research Infrastructure (ORF-RI: Grant no. 33016), the Mitacs Globalink Program and the German Academic Exchange Service (DAAD).

Author contributions: AA and SM contributed equally to this work. The manuscript was written through contributions of all authors. All authors have given approval to the final version of the manuscript.

6.7 References

1. Bielecka, Z. F.; Maliszewska-Olejniczak, K.; Safir, I. J.; Szczylik, C.; Czarnecka, A. M., Three-dimensional cell culture model utilization in cancer stem cell research. *Biol Rev Camb Philos Soc* **2017,** *92* (3), 1505-1520.

2. Goers, L.; Freemont, P.; Polizzi, K. M., Co-culture systems and technologies: taking synthetic biology to the next level. *J R Soc Interface* **2014,** *11* (96).

3. Miki, Y.; Ono, K.; Hata, S.; Suzuki, T.; Kumamoto, H.; Sasano, H., The advantages of co-culture over mono cell culture in simulating in vivo environment. *J Steroid Biochem Mol Biol* **2012,** *131* (3-5), 68-75.

4. Estrada, M. F.; Rebelo, S. P.; Davies, E. J.; Pinto, M. T.; Pereira, H.; Santo, V. E.; Smalley, M. J.; Barry, S. T.; Gualda, E. J.; Alves, P. M.; Anderson, E.; Brito, C., Modelling

the tumour microenvironment in long-term microencapsulated 3D co-cultures recapitulates phenotypic features of disease progression. *Biomaterials* **2016,** *78*, 50-61.

5. Benton, G.; DeGray, G.; Kleinman, H. K.; George, J.; Arnaoutova, I., In vitro microtumors provide a physiologically predictive tool for breast cancer therapeutic screening. *PLoS One* **2015,** *10* (4), e0123312.

6. John F. Gierthy; II, D. W. L., Inhibition of postconfluent focus production in cultures of MCF-7 human breast cancer cells by 2,3,7,8-tetrachlorodibenzo-p-dioxin. *Breast Cancer Research and Treatment* **1988,** *12*, 227-233.

7. Paraic A. Kenny; Genee Y. Lee; Connie A. Myers; Richard M. Neve; Semeiks, J. R.; Paul T. Spellman; Katrin Lorenz; Eva H. Lee; Mary Helen Barcellos-Hoff; Ole W. Petersen; Joe W. Gray; Bissell, M. J., The morphologies of breast cancer cell lines in three-dimensional assays correlate with their profiles of gene expression. *Mol. Oncol.* **2007,** *1*, 84-96.

8. van Duinen, V.; Trietsch, S. J.; Joore, J.; Vulto, P.; Hankemeier, T., Microfluidic 3D cell culture: from tools to tissue models. *Curr Opin Biotechnol* **2015,** *35*, 118-26.

9. Hatherell, K.; Couraud, P. O.; Romero, I. A.; Weksler, B.; Pilkington, G. J., Development of a three-dimensional, all-human in vitro model of the blood-brain barrier using mono-, co-, and tri-cultivation Transwell models. *J Neurosci Methods* **2011,** *199* (2), 223-9.

10. Campbell, J. J.; Davidenko, N.; Caffarel, M. M.; Cameron, R. E.; Watson, C. J., A multifunctional 3D co-culture system for studies of mammary tissue morphogenesis and stem cell biology. *PLoS One* **2011,** *6* (9), e25661.

11. Albrecht, D. R.; Underhill, G. H.; Wassermann, T. B.; Sah, R. L.; Bhatia, S. N., Probing the role of multicellular organization in three-dimensional microenvironments. *Nat Methods* **2006,** *3* (5), 369-75.

12. Hesselman, M. C.; Odoni, D. I.; Ryback, B. M.; de Groot, S.; van Heck, R. G.; Keijsers, J.; Kolkman, P.; Nieuwenhuijse, D.; van Nuland, Y. M.; Sebus, E.; Spee, R.; de Vries, H.; Wapenaar, M. T.; Ingham, C. J.; Schroen, K.; Martins dos Santos, V. A.; Spaans, S. K.; Hugenholtz, F.; van Passel, M. W., A multi-platform flow device for microbial (co-) cultivation and microscopic analysis. *PLoS One* **2012,** *7* (5), e36982.

13. Frimat, J. P.; Becker, M.; Chiang, Y. Y.; Marggraf, U.; Janasek, D.; Hengstler, J. G.; Franzke, J.; West, J., A microfluidic array with cellular valving for single cell co-culture. *Lab Chip* **2011,** *11* (2), 231-7.

14. Chung, S.; Sudo, R.; Mack, P. J.; Wan, C. R.; Vickerman, V.; Kamm, R. D., Cell migration into scaffolds under co-culture conditions in a microfluidic platform. *Lab Chip* **2009,** *9* (2), 269-75.

15. Huh, D.; Hamilton, G. A.; Ingber, D. E., From 3D cell culture to organs-on-chips. *Trends Cell Biol* **2011,** *21* (12), 745-54.

16. Schmidt, J. K.; Riedele, C.; Regestein, L.; Rausenberger, J.; Reichl, U., A novel concept combining experimental and mathematical analysis for the identification of unknown interspecies effects in a mixed culture. *Biotechnol Bioeng* **2011,** *108* (8), 1900-11.

17. Souza, G. R.; Molina, J. R.; Raphael, R. M.; Ozawa, M. G.; Stark, D. J.; Levin, C. S.; Bronk, L. F.; Ananta, J. S.; Mandelin, J.; Georgescu, M. M.; Bankson, J. A.; Gelovani, J. G.; Killian, T. C.; Arap, W.; Pasqualini, R., Three-dimensional tissue culture based on magnetic cell levitation. *Nat Nanotechnol* **2010,** *5* (4), 291-6.

18. Felton, E. J.; Copeland, C. R.; Chen, C. S.; Reich, D. H., Heterotypic cell pair co-culturing on patterned microarrays. *Lab Chip* **2012,** *12* (17), 3117-26.

19. David Melville; Frank Paul; Roath, S., Direct Magnetic Separation of Red Blood Cells from Whole Blood. *Nature* **1975,** *255*, 706.

20. Mirica, K. A.; Ilievski, F.; Ellerbee, A. K.; Shevkoplyas, S. S.; Whitesides, G. M., Using Magnetic Levitation for Three Dimensional Self-Assembly. *Advanced Materials* **2011,** *23* (36), 4134-4140.

21. Durmus, N. G.; Tekin, H. C.; Guven, S.; Sridhar, K.; Yildiz, A. A.; Calibasi, G.; Ghiran, I.; Davis, R. W.; Steinmetz, L. M.; Demirci, U., Magnetic levitation of single cells. *Proceedings of the National Academy of Sciences* **2015,** *112* (28), E3661-E3668.

22. Ki-Ho Han; Frazier, A. B., Diamagnetic Capture Mode Magnetophoretic Microseparator for Blood Cells. *Journal of Microelectromechanical Systems* **2005,** *14* (6), 1422 - 1432.

23. Abdel Fattah, A. R.; Ghosh, S.; Puri, I. K., High gradient magnetic field microstructures for magnetophoretic cell separation. *J Chromatogr B Analyt Technol Biomed Life Sci* **2016,** *1027*, 194-9.

24. Akiyama, Y.; Morishima, K., Label-free cell aggregate formation based on the magneto-Archimedes effect. *Applied Physics Letters* **2011,** *98* (16), 163702.

25. David Melville; Frank Paul; Roath, S., Fractionation of Blood Components Using High Gradient Magnetic Separation. *IEEE Trans. Magn.* **1982,** *MAG-18* (6), 1680 - 1685.

26. Tasoglu, S.; Yu, C. H.; Liaudanskaya, V.; Guven, S.; Migliaresi, C.; Demirci, U., Magnetic levitational assembly for living material fabrication. *Advanced healthcare materials* **2015,** *4* (10), 1469-1476.

27. Abdel Fattah, A. R.; Meleca, E.; Mishriki, S.; Lelic, A.; Geng, F.; Sahu, R. P.; Ghosh, S.; Puri, I. K., In Situ 3D Label-Free Contactless Bioprinting of Cells through Diamagnetophoresis. *ACS Biomaterials Science & Engineering* **2016,** *2* (12), 2133-2138.

28. Cos, S.; Álvarez-García, V.; González, A.; Alonso-González, C., Melatonin modulation of crosstalk among malignant epithelial, endothelial and adipose cells in breast cancer. *Oncology letters* **2014,** *8* (2), 487-492.

29. Pavel, M.; Renna, M.; Park, S. J.; Menzies, F. M.; Ricketts, T.; Füllgrabe, J.; Ashkenazi, A.; Frake, R. A.; Lombarte, A. C.; Bento, C. F., Contact inhibition controls cell survival and proliferation via YAP/TAZ-autophagy axis. *Nature communications* **2018,** *9* (1), 2961.

30. do Amaral, J. B.; Rezende-Teixeira, P.; Freitas, V. M.; Machado-Santelli, G. M., MCF-7 cells as a three-dimensional model for the study of human breast cancer. *Tissue Engineering Part C: Methods* **2011,** *17* (11), 1097-1107.

31. Y, W.; M, S.; JV, V., Epithelial-Mesenchymal Transition and Breast Cancer. *Journal of Clinical Medicine* **2016,** *5(2): 13*.

32. Shankar, J.; Nabi, I. R., Actin cytoskeleton regulation of epithelial mesenchymal transition in metastatic cancer cells. *PLoS One* **2015,** *10* (3), e0119954.

33. Maeda, M.; Johnson, K. R.; Wheelock, M. J., Cadherin switching: essential for behavioral but not morphological changes during an epithelium-to mesenchyme transition. *Jounral of Cell Science* **2004,** *118*, 873-887.

34. Hazan, R. B.; Phillips, G. R.; Qiao, R. F.; Norton, L.; Aaronson, S. A., Exogenous expression of N-cadherin in breast cancer cells induces cell migration, invasion, and metastasis. *The Journal of cell biology* **2000,** *148* (4), 779-790.

35. Henkes, S.; Kostanjevec, K.; Collinson, J. M.; Sknepnek, R.; Bertin, E., Dense active matter model of motion patterns in confluent cell monolayers. *Nature communications* **2020,** *11* (1), 1405.

7 Conclusions and Future Directions

7.1 Conclusions

The rapid and reproducible magnetic 3D cell printing method described in this thesis offers an engineering solution to a current biomedical challenge. Traditional 3D printing requires specialized equipment for printing objects using additive manufacturing. Recent innovations incorporate the use of biocompatible materials to support the growth of living cells. Here, the concept of 3D printing is reimagined. 3D dimensions on the order of hundreds of μm is formed completely *in situ*, without the use of moving parts, equipment nozzles, or artificial materials. Instead, the intentional positioning of living cells is possible through manipulation of magnetic properties. The ability to rapidly manipulate cells in a safe, controllable and non-contact manner permits the formation of unique cell landscapes and microarchitectures found in human tissues. The use of rapid magnetic 3D printing of cells enables the observation of *in vivo* phenomenon, *in vitro*.

The goal of this thesis was to describe the versatility of magnetic 3D printing. This was achieved using various cell lines. Although cells may coalesce within similar times (within 3 hours), the biological activity of each cell line to produce ECM ultimately determines the total time required for fabrication of a robust cellular structure. Barring the use of magnetic printing, however, the 3D cellular structures require more time for formation and are less reproducible. Through magnetic 3D printing of cells, spherical structures of MCF-7 were shown to be formed within 6 hours, MDA-MB-231 cells within 24 hours, and NIH/3T3 cells within 3 hours. These times of formation are not observed in

literature, which report one to multiple days. Thus, magnetic printing offers a solution to rapidly and consistently produce 3D cellular structures for downstream applications.

The combination of multidimensional and co-culture cell populations can be easily integrated into existing standard multi-well plates using magnetic printing. The utilization of various surface treatments, such as TCT and ULA, expands the printing capabilities to observe unique cell morphologies and heterogeneous cell landscapes to form 2.5D and 3D cellular structures, respectively. Complex cellular structures are formed rapidly, with high reproducibility and completely *in situ*.

7.2 Future Directions

Magnetic 3D printing of cells has the potential to be a game-changer for the future of biomedical innovation. As the magnetic 3D printing methodology is refined, its use in clinical settings will directly benefit the treatment of disease and patient outcome. So far, the use of magnetic 3D printing via negative magnetophoresis has primarily been demonstrated using immortalized cell lines. This is useful for *in vitro* cellular studies and in the drug discovery process. However, the use of patient-derived cells in the future will be required for efforts towards personalized medicine to determine optimal treatment plans, or transplantation of functional tissues and organs. The former is a realistic immediate translation of the technology, while the latter requires tissue engineering challenges to be overcome, regardless of the employed approach. These challenges include the formation vasculature, dimensions of the printed tissue or organ, cost, biocompatibility and functionality *in vivo*.

Automation of 3D magnetic cell printing in standardized multi-well plates will enable the ability to form tens of hundreds cellular clusters at a time. Future work includes the formation of different 3D cellular geometries, such as rings, lines, or tubular structures. These can be used individually using the same cell source to observe a specific cellular response or as building blocks for larger heterogeneous 3D constructs.

The current constraints of the magnetic printing method must be addressed. Recent investigations have revealed long-term toxicity of Gd-DTPA, which had not been observed in 3-day studies. Therefore, careful selection of the Gd^{3+} chelate should be considered for continued use. A promising candidate is gadobutrol. Alternative methods for diamagnetic cell printing in a medium which do not require the medium to contain a dissolved paramagnetic salt can also be explored. Previous demonstrations have shown that the use of MNPs in a medium can sufficiently displace single cells. This approach can be expanded to demonstrate magnetic printing of 3D cellular structures.

It is my sincere belief that magnetic 3D cell printing will be a stepping stone towards new hope for those inflicted by disease. Soon, it will no longer be necessary to endure ineffective and painful treatment. Instead, a custom and personalized therapy will be available on a case-by-case basis, as opposed to *'one size fits all'*. This can be achieved in all levels of tissue engineering, including cellular studies in early research, diagnosis, and treatment of disease. Magnetic 3D printing of cells is a promising method rich with potential for the future of medical enhancement.